Experimental and Theoretical Studies of Organic High-Spin Ions and Extremely Non-Rigid Ions(Dissertation_全文)

AUTHOR(S):

Matsushita, Michio

(2)

EXPERIMENTAL AND THEORETICAL STUDIES OF ORGANIC HIGH-SPIN IONS AND EXTREMELY NON-RIGID IONS

Doctoral Thesis

Department of Chemistry
Faculty of Science
Kyoto University

Michio Matsushita

Kyoto 1991

Contents

Chapter 0. Generation of Organic Radical Ions in Rigid Solutions by Radiolysis

In spite of the importance of organic radical ions as an intermediate of various chemical processes, experimental studies are relatively scare because of their high reactivity. In rigid media, however, such species can be produced in situ by radiolysis or photolysis and various spectroscopic studies can be carried out. In our laboratory a radiolytic technique has been used for generation of radical ions since the pioneering work by Shida and Hamill [Shida and Hamill (1968a, b, c)]. We will explain briefly the essential feature of the radiolytic method [Hamill (1968), Shida and Iwata (1973), Shida *et al.* (1984), Shida (1988, 1991)].

Materials consisting of elements of the first three rows of the periodic table interact with photons of energies of the order of 1 MeV mainly to cause inner shell ionization and the Compton effect. Typical such photons are γ-rays from ^{60}Co. With these events highly energetic electrons are ejected which, in turn, excite and ionize molecules of the system. In condensed matter the ionized molecules and the counterpart electrons are quickly deactivated and the whole system is thermalized within picoseconds. If we consider a system consisting of solute and matrix molecules with a molar concentration ratio of, say, 1 to 10^3, the direct ionization effect on solute molecules is negligibly small because the excitation by the high energy electrons is non-selective and roughly proportional to the molar fraction. Thus, the radiolytic effect at this stage is mainly regarded as the ionization of the matrix molecule *M*.

$$M + \gamma \rightarrow M^+ + e^-, \qquad (0.1)$$

Subsequent processes depend on the chemical character of the matrix molecule, which can be utilized for the selective generation of the radical cation or anion of the solute molecule as will be described below:

For the generation of radical anion of solute molecules 2-methyltetrahydrofuran (MTHF, $C_5H_{10}O$) is used as the matrix. The major processes upon γ-irradiation are as follows.

$$C_5H_{10}O + \gamma \rightarrow C_5H_{10}O^+ + e^-, \qquad (0.2)$$

$$C_5H_{10}O^+ + C_5H_{10}O \rightarrow C_5H_{11}O^+ + \cdot C_5H_9O, \qquad (0.3)$$

$$e^- + S \rightarrow S^-, \qquad (0.4)$$

where S denotes the solute molecule. Electrons ejected by reaction (0.2) move through the rigid solution until they encounter a solute molecule having a sufficiently high electron affinity to yield the corresponding radical anion S^-. On the other hand, the positive charge of the matrix molecule in reaction (0.2) suffers an ion-molecular reaction (0.3). The MTHF matrix is suitable for optical studies because it forms a transparent glassy solid at 77 K. However, it is not necessarily suitable for the ESR study since the ESR signal of the solute radical anion is easily masked by the overlapping signal due to the neutral radical $\bullet C_5H_9O$ produced by reaction (0.3).

The matrix molecules used for the generation of radical cations comprises alkyl halides such as CCl_4 [Shida and Hamill (1966a, b)], *sec*-butyl chloride, Freons such as $CFCl_3$ [Shida and Kato (1979)], and the 1:1 mixture of $CFCl_3$ and CF_2BrCF_2Br (Freon mixture, FM) [Grimison and Simpson (1968)]. The major processes that occur under γ-irradiation can be summarized as follows.

$$RX + \gamma \rightarrow RX^+ + e^-, \qquad (0.5)$$

$$e^- + RX \rightarrow (RX)^- \rightarrow R\bullet + X^-, \qquad (0.6)$$

$$RX^+ + S \rightarrow RX + S^+, \qquad (0.7)$$

where the alkyl halide is denoted by RX (X = halogen). Reaction (0.6) represents that the electron ejected from a matrix molecule by γ-irradiation reacts with another matrix molecule to cause dissociation of the carbon-halogen bond in RX. The positive charge in RX^+ is transferred intermolecularly to the solute molecule S. If the ionization potential of S is lower than that of the matrix molecule (e.g., I.P.($CFCl_3$) = 11. 8 eV), the radical cation of solute generated in reaction (0.7) is stabilized in the matrix. For the optical measurements *BuCl* or FM is used for the matrix substance because they forms a glassy solid at 77 K, whereas a polycrystalline $CFCl_3$ matrix is not convenient for the optical study. Instead, it was found to give a fairly well resolved ESR spectra of solute cations [Shida and Kato (1979), Shida *et al.* (1980)]. Since then a number of ESR spectroscopists have utilized the Freon matrices for ESR studies of various radical cations. The advantageous feature of $CFCl_3$ matrix is little disturbance from byproduced neutral radical $CFCl_2\bullet$ because of the extreme anisotropy of hyperfine interaction fluorine atom [Shida *et al.* (1991)]. The methods described here have been used throughout our experiments discussed later.

Using the radiolytic method, we have investigated several novel radical ions such as monoions of organic high-spin molecules as described in Chapter 1.

Chapter 2 is devoted for the analysis of the Jahn-Teller effect in CH_4^+. For the analysis of the CH_4^+ system it is essential to use the permutation inversion (PI) group theory. The brief explanation of the PI group theory is given in Appendix A. The PI group theory is used also in the analysis of the internal rotation of the two methyl groups in $CH_3OCH_3^+$ [Matsushita *et al.* (1990a)] (see the last section of Appendix A).

Chapter 1. ESR Study on Organic Ions of High-Spin States: Monoanion and Monocation of *m*-Phenylenebis(phenylmethylene)

Introduction

Since the first discovery of an organic quintet molecule [Itoh (1967), Wasserman *et al.* (1967)], organic high-spin molecules have been studied almost for a quarter of a century. It has now been firmly established that the spin alignment in these neutral high-spin molecules is dictated by the topology of the π-electron network [Itoh (1978)]. Based on the topological symmetry, efforts to obtain organic ferromagnets are continued.

With the intention of discovering new aspects of such high-spin molecules, we have studied charged high-spin molecules [Matsushita *et al.* (1990b)]. The charged system is potentially interesting not only from the experimental but also from the theoretical viewpoint, since the spin alignment of the charged system cannot be easily predicted in contrast to the neutral systems [Yamaguchi *et al.* (1987)]. As a prototype of charged polycarbenes a monoanion [Matsushita *et al.* (1990b)] and a monocation of *m*-phenylenebis(phenylmethylene) ($\mathbf{1}^{\pm\bullet}$) have been generated for the first time, and the ground state has been characterized by ESR.

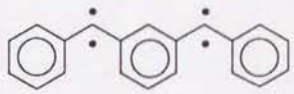

1

Historical background of the study of organic high-spin molecules

The ground electronic state of most organic molecules is singlet. Because usual organic molecules are not so symmetric, most of the molecular orbitals are non-degenerate. In the usual 32 point groups, the highest degeneracy of molecular orbitals is three so that the maximum spin quantum number is 3/2 according to Hund's rule. The only exception is C_{60} which belongs to I_h point group [Kroto *et al.* (1985), Krätschmer *et al.* (1990a, b), Ajie *et al.* (1990)]. An example of the orbital degeneracy is the triplet ground state of pentachlorocyclopentadienyl cation [Breslow *et al.* (1964)].

A theoretical work on organic high-spin molecules was made by Higuchi in 1963. He calculated the fine-structure parameters for several aromatic high-spin hydrocarbons which were hypothetical at that time [Higuchi (1963a, b)]. One of these hypothetical molecules was experimentally detected in 1967 by K. Itoh (1967) and by Wasserman *et al.* (1967). The molecule, *m*-phenylenebis(phenylmethylene) (**1**) (*m*-PBPM), is quintet in the ground state and its fine-structure parameters are in a reasonable agreement with the value predicted by Higuchi (1963a, 1970).

The high spin multiplicity of *m*-PBPM, which may appear curious considering its low symmetry, can be accounted for by the simple Hückel MO theory: In early 1950s Longuet-Higgins pointed out that in terms of LCAO-MO theory of π-electron systems (1950) an alternant hydrocarbon has at least N - 2T non-bonding molecular orbitals (NBMO's) where N denotes the number of carbon atoms in the conjugated system and T the maximum number of double bonds occurring in any resonance structure (1950). According to his argument there should be just one electron in each NBMO in the ground state, and if there are two or more such electrons, their spins will be parallel according to Hund's rule. This is an accidental degeneracy in view of the point group but has some mathematical meaning within the simple LCAO-MO approximation. What determines the orbital degeneracy of NBMO is the structure of secular equations for π-MO's, that is, the sequence of carbon atoms forming the conjugated system. Such an arrangement of atoms may be called topologically symmetric. In this sense the orbital degeneracy of NBMO is called "topological degeneracy" [Itoh (1978)]. In *m*-PBPM there are two non-bonding π-orbitals and two in-plane n-orbitals at the two carbene sites. Since the energy difference between the n-orbital and NBMO may be small, there can be four nearly degenerate orbitals so that the ground state is quartet.

Based on the guiding principle of topological symmetry, Prof. Itoh's group have studied a series of high-spin aromatic polycarbenes which includes; benzene-1,3,5-tris-phenylmethylene (**2**) ($S = 3$) [Takui and Itoh (1973)], 3,3'-diphenylmethylenebis(phenylmethylene) (**3**) ($S = 3$) [Teki *et al.* (1985)], *m*-phenylenebis[(diphenylmethylen-3-yl)methylene] (**4**) ($S = 4$) [Teki *et al.* (1983, 1986)], and the undecet aromatic polycarbene (**5**) ($S = 5$) [Fujita *et al.* (1990)]. Recently they reported the polycarbene with $S = 6$ (**6**) [Furukawa *et al.* (1991)].

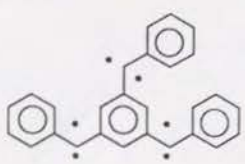

2

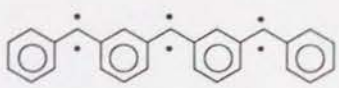

3

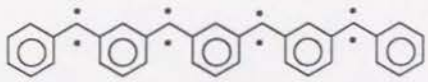

4

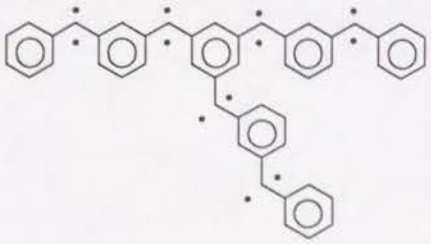

6

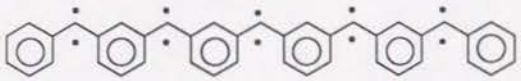

5

The static magnetic susceptibility of the nonet tetracarbene was measured by Prof. Iwamura's group [Sugawara *et al.* (1984, 1986)]. Prof. Itoh's group have also studied related compounds where high-spin excited states lie close to the ground state. For example, biphenyl-3,3'-bis(phenylmethylene) (**7**) was found to have the first excited triplet and the second excited quintet states, which are located above the singlet ground state by only 20 and 60 cm^{-1}, respectively, in the conformation favored at below 140 K [Itoh (1978)]. Recently, the spin density distribution in its first excited triplet state was experimentally determined by the single-crystal ^{1}H-ENDOR measurement of the excited state [Okamoto *et al.* (1990)].

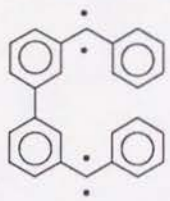

7

Spin alignment in organic high-spin molecules with both unpaired π and non-bonding electrons of carbene has been studied by several methods. The Hubbard Hamiltonian [Hubbard (1963)] gives correct prediction for the ground-state spin multiplicity and for the electronic structure of the highest spin state [Teki *et al.* (1987a)]. The Hubbard model was also used in the analysis of the ferromagnetic properties of an ideal one-dimensional polymer, *m*-polydiphenylcarbene (**8**) [Nasu (1986)].

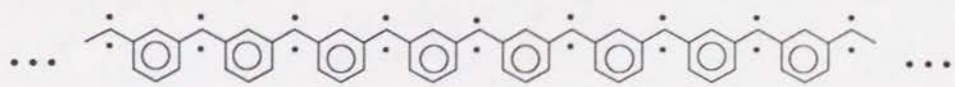

8

However, it fails to predict low-lying excited states with lower spin multiplicities because the Hubbard Hamiltonian commutes with S_z but not with S^2. Another popular approach is to assume the Heisenberg Hamiltonian. This Hamiltonian has been applied to some π-electron networks by Ovchinnikov (1978) for the prediction of their ground-state spin multiplicity on the basis of a theorem given by Lieb and Mattis (1962). When applied to organic high-spin molecules with both unpaired π and n electrons, this Heisenberg model predicts spin states correctly not only for ground states but also for low-lying excited states [Teki *et al.* (1987b)]. This is because the Heisenberg Hamiltonian commutes with S^2 as well as S_z. Thus, the Heisenberg model can explain consistently the features of the spin alignment, i.e., the sequence of the spin states, the relative magnitude of their energy gaps, and their spin density distributions. Klein *et al.* showed that the prediction of the ground state via the simple VB model (the isotropic Heisenberg spin Hamiltonian) is in remarkable agreement with the experimental evidence [Klein (1982), Klein *et al.* (1982), Alexander and Klein (1988)].

In the powder pattern first derivative ESR spectra, observed peaks are usually assigned to "canonical peaks" which arise from singularities of the absorption intensity that occur at turning points corresponding to the principal axes of *g*, hyperfine, and fine-structure tensors. Under certain conditions, however, an additional singularity occurs at an extra turning point at a certain direction which lies off the principal axes [Neiman and Kivelson (1961)]. This causes a extra peak called "extra line", or "off-axis line". In the series of organic high-spin molecules studied by Itoh's group, an extra line was reported first in the K-band powder pattern spectrum of the septet molecule [Teki *et al.* (1985)]. Teki has derived the general conditions for the occurrence of extra lines of fine structure by the third-order perturbation calculation [Teki *et al.* (1988)]. In general, extra lines tend to appear with an increase of *S* and of fine-structure energy, and with a decrease of microwave frequency. It was shown that for high-spin systems of $S > 1$ extra lines commonly appear at the X-band with comparable intensity with normal canonical peaks, which was found to be the case in the monoanion and monocation of *m*-PBPM [Matsushita *et al.* (1990b)].

At the end of this section, some other works on high-spin organic molecules will be mentioned. Wasserman *et al.* detected quintet and septet nitrenes isoelectric with the quintet and septet polycarbenes [quintet dinitrene (**9**) (1967), septet trinitrene (**10**) (1968)]. Kothe *et al.* studied the powder pattern spectrum of a quartet radical, 1,3,5-benzenetriyltris[bis(biphenyl-4-yl)methyl] (**11**) [Reibisch *et al.* (1972), Brickmann and Kothe (1973)]. The high-spin organic molecules reported so far are very reactive so that they are stable only when doped in a solid matrix at low temperatures. Recently, however, Rajca reported the 1,3-connected polyarylmethyl quintet tetraradical (**12**) which is stable at 195 K in THF solution [Rajca (1990a, b)]. Recently, Rajca has synthesized the 1,3-connected polyradical with up to 10 unpaired electrons ($S = 5$) [Rajca (1991)].

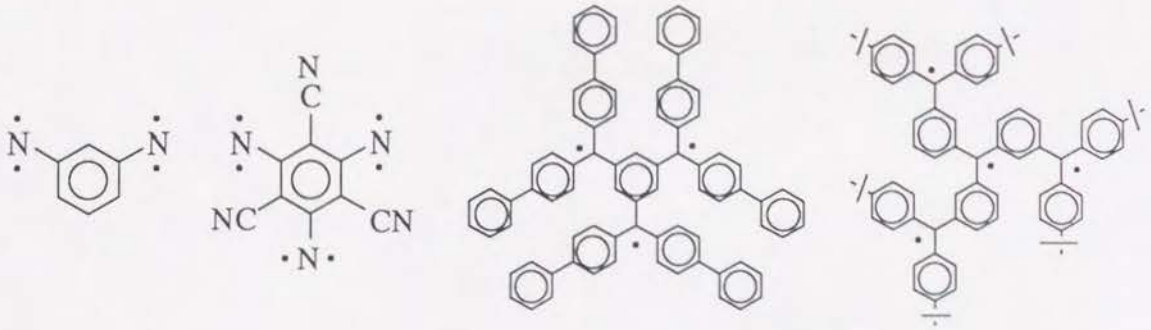

9 10 11 12

Experimental

1,3-Bis(α-diazobenzyl)benzene (1,3-BDB), which is the precursor of *m*-PBPM, was synthesized by a standard method in the literature [Murahashi *et al.* (1972)].

The radiolytic technique was used for the generation of the radical ions of 1,3-BDB (see Chapter 0). For the generation of the radical anion 2-methyltetrahydrofuran (MTHF) was used as the matrix and *sec*-butyl chloride (BuCl) was used for the generation of the radical cation. Commercial MTHF was purified by distillation followed by contacting with Na-K alloy in a vacuum line. 1,3-BDB was dissolved in MTHF or BuCl to a concentration of 5 – 10 mM and sealed off in Suprasil cells for ESR and optical measurements after degassing. The solution frozen at 77 K was γ-irradiated by ^{60}Co to a dose of ≈ 10^{19} eV/g.

The radical anion or cation of 1,3-BDB produced by γ-irradiation was photolyzed to generate the corresponding monoion of *m*-PBPM using a USHIO halogen lamp (1000 W) with TOSHIBA cut-off glass filters, R-62, O-55, and Y-51.

The ESR measurement was performed with a JEOL PE-2X spectrometer equipped with an Air Products LTR-3 refrigerator at Kyoto University and a Bruker ESP 300 spectrometer equipped with an Oxford ESR 910 temperature controller at Osaka City University. The ^{1}H-ENDOR measurements were carried out with a Bruker ESP 300/350 spectrometer with an Oxford ESR 910 temperature controller at Osaka City University. Cary 14RI and Cary 17I spectrophotometers were used for the optical measurements.

The simulations of ESR spectra were carried out with a HITAC M660K at Osaka City University Computer Center and a FACOM M-780/30 at the Data Processing Center of Kyoto University.

Results and discussion for a monoanion of *m*-PBPM (*m*-PBPM$^{-\bullet}$)

1. Formation of the radical anion of 1,3-BDB. The solution of 1,3-BDB in MTHF becomes a glassy solid at 77 K with purple color (see curve 1 in Figure 1.1). The color is ascribable to the $n\pi^*$-transition of the diazo group with $\varepsilon = 254$ at $\lambda_{max} = 530$ nm [Itoh *et al.* (1968)]. According to the recipe described in Chapter 0, the radical anion of 1,3-BDB was produced by γ-irradiation. The generation of the anion was confirmed by the optical absorption spectrum before and after γ-irradiation: the band at 530 nm diminished upon irradiation, and an intense absorption sets in at about 500 nm, increasing sharply toward shorter wavelengths (Figure 1.1). The absorption was accompanied with feeble absorptions appearing throughout the visible and near-IR regions. If the electron had not been scavenged by 1,3-BDB, one must observe the well-known absorption band due to the matrix-trapped electron in the same spectral region [Shida (1988)]. Thus, the absorption appearing after γ-irradiation is regarded as due to the radical anion of 1,3-BDB. To reinforce this inference, the following subsidiary experiment was also carried out: a sufficient amount of alkyl halides such as CF_2BrCF_2Br was dissolved (≈ 100 mM) along with 1,3-BDB, and exactly the same procedure as that without the halides was repeated. Since the halide denoted by RX scavenges electrons efficiently by the dissociative electron attachment, $RX + e^- \rightarrow R\bullet + X^-$ (see Chapter 0), it was expected that the optical change observed for the 1,3-BDB/MTHF solution would be suppressed drastically by the competition for the electron, which was indeed found to be the case.

The X-band ESR spectrum after γ-irradiation showed signals in a range of 0.32 – 0.34 T. This signals are attributed to the radical anion of 1,3-BDB superimposed on the signals due to the by-produced neutral radicals of the matrix (see the inset of Figure 1.2).

With the dose given and with the known G value of the total scavengeable electron [Shida (1988)], the concentration of the radical anion of 1,3-BDB was estimated as to be ≈ 1.5 mM; that is, conversion from the neutral 1,3-BDB to the radical anion was roughly 15 % under the present experimental condition.

2. Formation of *m*-PBPM$^{-\bullet}$. When the γ-irradiated 1,3-BDB/MTHF solution was photolyzed with $\lambda > 620$ nm, several new peaks appeared in the ESR spectrum over a wide range of 0 – 0.6 T (Figure 1.2). This change indicates the generation of a new high-spin molecule. By analogy of the photolytic denitrogenation of the parent 1,3-BDB molecule [Itoh (1967)], the observed spectral change is most plausibly associated with the following reaction.

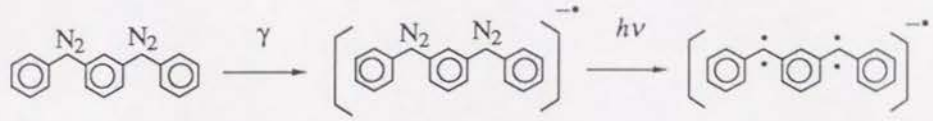

(1.1)

1,3-BDB 1,3-BDB$^{-\bullet}$ *m*-PBPM$^{-\bullet}$

Since the change was not observed for the sample containing the alkyl halide with 1,3-BDB, it was confirmed that the final product of reaction (1.1) is negatively charged. Furthermore, since only the doublet and the quartet is allowed for the spin multiplicity of *m*-PBPM$^{-\bullet}$, the fine structure observed at 0 – 0.6 T must be associated with *m*-PBPM$^{-\bullet}$ in the quartet state. Parallel measurements of optical spectra also showed a remarkable change upon photolysis; i.e., the intense absorption at $\lambda < 500$ nm was replaced with new absorption bands throughout the whole range of the near-UV to near-IR region, the major band being $\lambda_{max} = 500$ nm. This optical change can be associated with the formation of *m*-PBPM$^{-\bullet}$ upon photolysis.

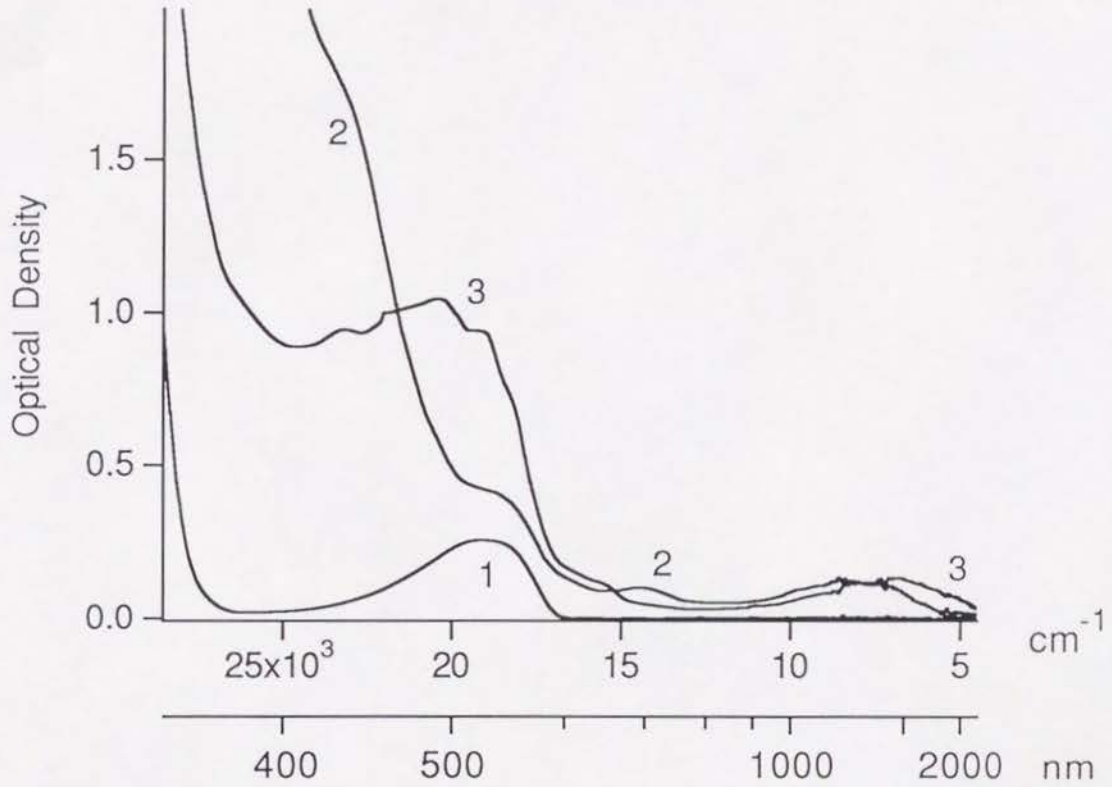

Figure 1.1 Electronic absorption spectra of 1,3-BDB/MTHF solutions at 77 K:
1, Before γ-irradiation.
2, After γ-irradiation.
3, Same as 2, but followed by photobleaching with $\lambda > 620$ nm.
Optical path length 1.5 mm.

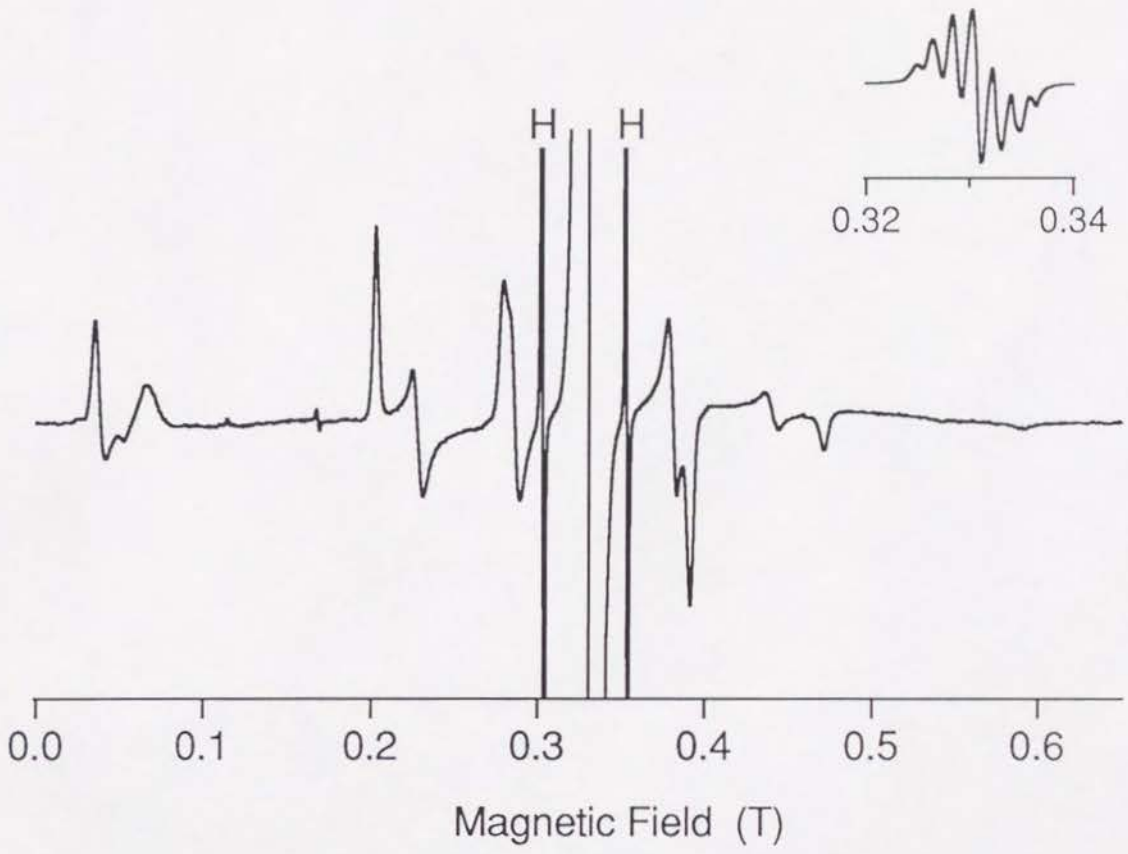

Figure 1.2 X-band ESR spectrum for a γ-irradiated and subsequently photobleached 1,3-BDB/MTHF solution at 77 K. Prior to photobleaching with $\lambda > 620$ nm, the spectrum showed only the signal at 0.3 −0.35 T and the doublet due to the hydrogen atom produced in the quartz cell by irradiation. A reduced-scale spectrum at this stage is shown in the inset. Upon photobleaching several new peaks appeared in the ESR spectrum over a wide range of 0 − 0.6 T in addition to the above-mentioned spectrum. The new peaks are assigned to the spin quartet *m*-PBPM$^{\cdot-}$.

3. Analysis of the X-band ESR spectrum of *m*-PBPM$^{-\bullet}$. To confirm that the ESR spectrum arises from a spin-quartet state of *m*-PBPM$^{-\bullet}$, we performed the spectral simulation based on the following spin Hamiltonian.

$$\mathcal{H} = g\beta\tilde{\mathbf{S}}\cdot\mathbf{H} + D\left[S_Z^2 - S(S+1)/3\right] + E\left(S_X^2 - S_Y^2\right) \qquad (1.2)$$

The Hamiltonian corresponding to a particular orientation of the magnetic field was diagonalized to obtain the resonant field and transition probability. Note that the transition probability depends on the third Euler angle χ so that it is necessary to average the transition probability over the whole 2π angle of χ. However, since the integration over 2π is equal to the average of transition probability at χ and that at $\chi + \pi/2$, calculations at only two points of χ are necessary (see Appendix B). Then, the spectrum was summed up over the whole spherical angle of 4π to get the powder-pattern spectrum. On account of symmetry of the fine-structure tensor, it is necessary to integrate only one eighth of the sphere. The number of orientations necessary for the simulated spectrum is 14,560. We assumed the Gaussian line-shape with common line-width of 3.6 mT for all the transitions.

The best fit parameters were found to be $g = 2.003$ (isotropic), $D = +0.1200$ cm^{-1}, and $|E| = 0.0045$ cm^{-1}. The sign of D was determined from the effect of Boltzmann factor on the relative intensity of ESR transitions (see below). The microwave frequency was equal to 9.188 GHz with which the experiment was performed. Figure 1.3 shows the angular dependence for random orientation (bottom) as well as the simulated spectrum (middle) obtained by the above best fit parameters. For the sake of convenience the principal axis transitions X and Y are labeled under the assumption of $E > 0$. Except for the masked area of 0.3 – 0.4 T, the agreement is excellent between the observed and simulated spectra. It should be noted that an off-axis extra line denoted by A in Figure 1.3 appears as expected for the case of half-integral spins and that the off-axis extra line is a key absorption peak in the spin multiplicity assignment [Teki *et al.* (1988)]. The appearance of the off-axis extra line assures that the observed fine-structure spectrum arises from a quartet spin state. The observation of the extra line in this work is the first example of extra lines from organic high-spin systems with half-integral spins.

The sign of D can be determined by the effect of the thermal population among the sublevels of the quartet state upon the relative intensity of ESR transitions. In the present work the intensity of the high-field X-axis canonical absorption at ≈0.44 T was compared with the low-field one at ≈0.22 T (see Figure 1.3). The intensity of the absorption was calculated by double integration of the first derivative peaks. The high-field X-absorption at 9.5 K is 1.9 times as strong as that at 1.4 K when normalized by the low-field X absorption. This result indicates unequivocally that the sigh of D is positive.

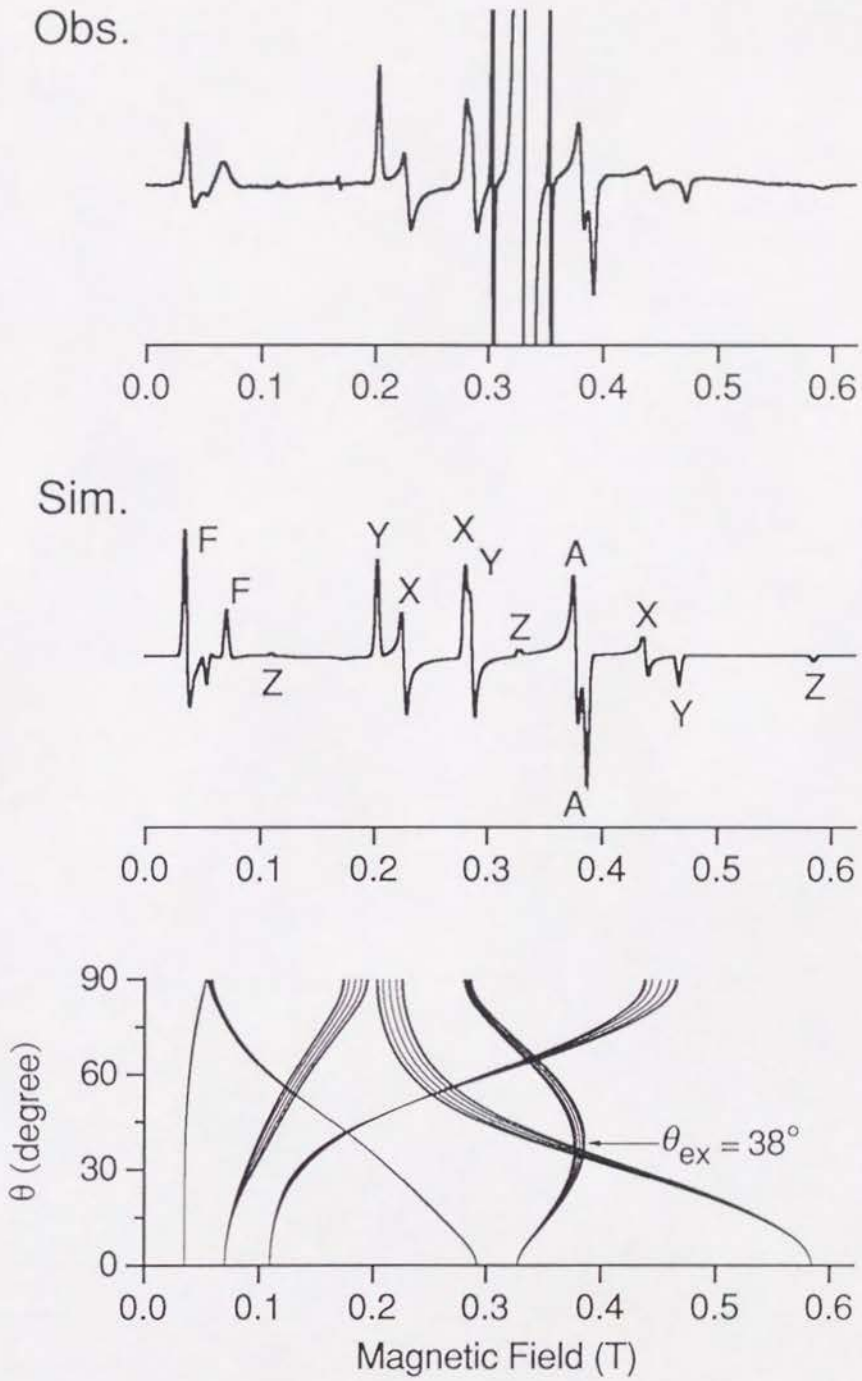

Figure 1.3 Observed and simulated X-band ESR spectra for the quartet state of *m*-PBPM$^{\bullet-}$. The angular dependence of resonant fields for random orientation is shown at the bottom. Symbols A and F denote the off-axis extra line and the "forbidden" bands corresponding to the transitions with $\Delta m_s = \pm 2$ and ± 3. The parameters used for the simulation are ν = 9.188 GHz, g = 2.003 (isotropic), D = +0.1200 cm^{-1}, and $|E|$ = 0.0045 cm^{-1}.

4. Spin multiplicity of the ground state of *m*-PBPM$^{-\cdot}$. In order to see whether or not the quartet state is the ground state, the temperature dependence of the intensity of the quartet signal was examined. Figure 1.4a shows a representative spectrum exhibiting the low-field *X* and *Y*-axis canonical absorptions of the anion along with several absorptions due to the quintet *m*-PBPM denoted by Q. For the measurement of the temperature of the sample the signal intensity of the neutral *m*-PBPM was used as an internal standard of the temperature. Because not all the 1,3-BDB is converted to its anion by γ-irradiation, the neutral *m*-PBPM can be produced by UV photolysis of the remaining 1,3-BDB [Itoh (1967)] together with the monoanion. To avoid the artifact due to the instrumental difference experiments were performed using both a JEOL PE-2X spectrometer with an Air Products LTR-3 refrigerator and a Bruker ESP 300 spectrometer with an Oxford ESR 910 temperature controller. The temperature dependence of the *Y*-axis peak of the anion obtained by the two instruments are shown in Figure 1.4b. The solid curves are calculated by the Boltzmann distribution in the sublevels of the quartet and the doublet states [Teki *et al.* (1986)]. The parameter $\Delta\varepsilon$ denotes the energy gap of ε(quartet) – ε (doublet). In the calculation for the curve denoted by $\Delta\varepsilon = -\infty$ the population in the doublet state was totally ignored. The scattered but essentially linear plots fits to the case of $\Delta\varepsilon = -\infty$ which signifies ε(quartet) « ε (doublet). The possibility of $|\Delta\varepsilon| < 1$ cm^{-1} can be ruled out because if so, the effective exchange interaction between the quartet and the doublet states should becomes significant and the eigenstate should not be described as a pure quartet nor a pure doublet state and the ESR spectrum should exhibit a characteristic feature different from those associated with a pure quartet or a pure doublet state. Since the present ESR spectrum can be analyzed unambiguously in terms of a pure quartet state, $|\Delta\varepsilon|$ must be much larger than ≈ 1 cm^{-1}. Thus, we can safely conclude that the ground state of the monoanion is quartet.

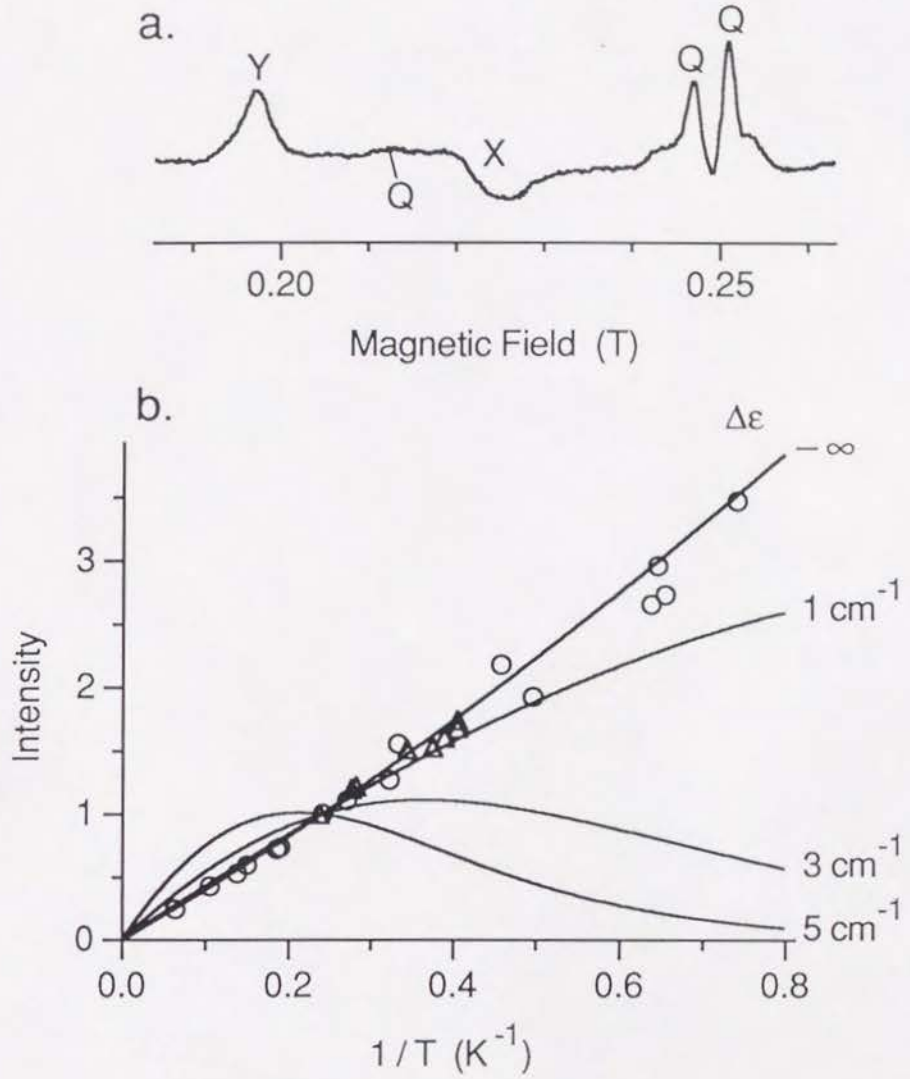

Figure 1.4 **a.** Typical ESR spectrum used for the calculation of the temperature dependence of the intensity of the *Y*-axis canonical peak due to the quartet anion. The signals due to neutral quintet are indicated by Q. The temperature was calibrated by the intensity of the neutral quintet signals at ≈0.25 T. The symbols X and Y denote the *X* and *Y*-axis canonical peaks of the quartet anion.

b. Temperature dependence of the intensity of the ESR signal of the *Y*-axis canonical peak shown in the upper spectrum. The triangles are experimental data measured with a JEOL spectrometer. Since the line-shape of the peak does not change with temperature, the intensity was calculated by the derivative peak height. The circles indicate data measured with a Bruker spectrometer and the intensity was calculated by double integration of the first derivative spectrum. The plot obtained by the double integrals is almost the same as that obtained by the derivative peak heights. Solid curves are the calculated temperature dependence for several values of $\Delta\varepsilon = \varepsilon(\text{quartet}) - \varepsilon(\text{doublet})$. All the experimental and theoretical intensities are nomalized at T = 4.2 K.

5. ^{1}H-ENDOR spectra of *m*-PBPM$^{-\bullet}$. In order to investigate the spin density distribution in the quartet ground state of the monoanion, ^{1}H-ENDOR measurement was carried out for the monoanion in the glassy solution of MTHF at 1.8 K.

Since the ENDOR study of single crystalline samples provides the angular dependence of the hfcc's, the principal values of the hfc tensor and the orientation of the principal axes relative to the crystalline axes can be determined precisely. However, for a randomly oriented sample of high-spin molecules the ENDOR measurement is usually feasible only for the direction of principal axes of the fine structure tensor because ESR peaks in the first derivative mode correspond to the turning points of the angular dependence of the resonant field which, in turn, correspond to the direction of the principal axes of the tensor. In some cases, the angular dependence of the resonant field yields an extra turning point at a magnetic field different from those corresponding to the principal axes. This gives rise to an off-axis extra line in the powder-pattern spectrum [Teki *et al.* (1988)] (see the angular dependence and the peak denoted by A in the simulation of Figure 1.3). In such a case it may be possible to observe the ENDOR signal corresponding to the extra turning point also, which was indeed observed in the present study (see below). In this context it is reminded that, in principle, ENDOR signals can be observed at any magnetic field if the ESR intensity and the condition of relaxation are favorable.

The ENDOR spectral pattern of high-spin molecules depends on the electron spin sublevels investigated: Under the high-field approximation the ^{1}H-ENDOR frequency ν is given by

$$\nu = \nu_n - a\, m_S \tag{1.3}$$

where ν_n is the Zeeman frequency of free proton and the symbols a and m_S denote the zz component of the hyperfine interaction tensor expressed in frequency units and the electron spin quantum number, respectively. Eq. (1.3) is valid for $|a\, m_S| \leq \nu_n$. For integral spin states, there are two characteristic ENDOR spectral patterns: One is that obtained by pumping the transition between $m_S = 0$ and ± 1. In this case all the signals due to $m_S = 0$ state collapse into a single peak at ν_n and only the signals due to $m_S = \pm 1$ state appear at frequencies apart from ν_n. Since the separation from ν_n is equal to a for $m_S = 1$ and $-a$ for $m_S = -1$, the hfcc of each proton can be easily determined from the spectrum (see Scheme 1.1a where a model system having two protons of hfcc's of $a_1 > 0$ and $a_2 < 0$ with $|a_1| > |a_2|$ is assumed.). The other is associated with ESR transitions involving states of $m_S \neq 0$ and is more complicated than the former since the ENDOR signals due to both the upper and the lower electron spin sublevels appear at frequencies different from ν_n. The resolution of hfcc's of the latter, however, is higher than the former because the separation of the ENDOR signals from ν_n is greater. Scheme 1.1b shows an example for the

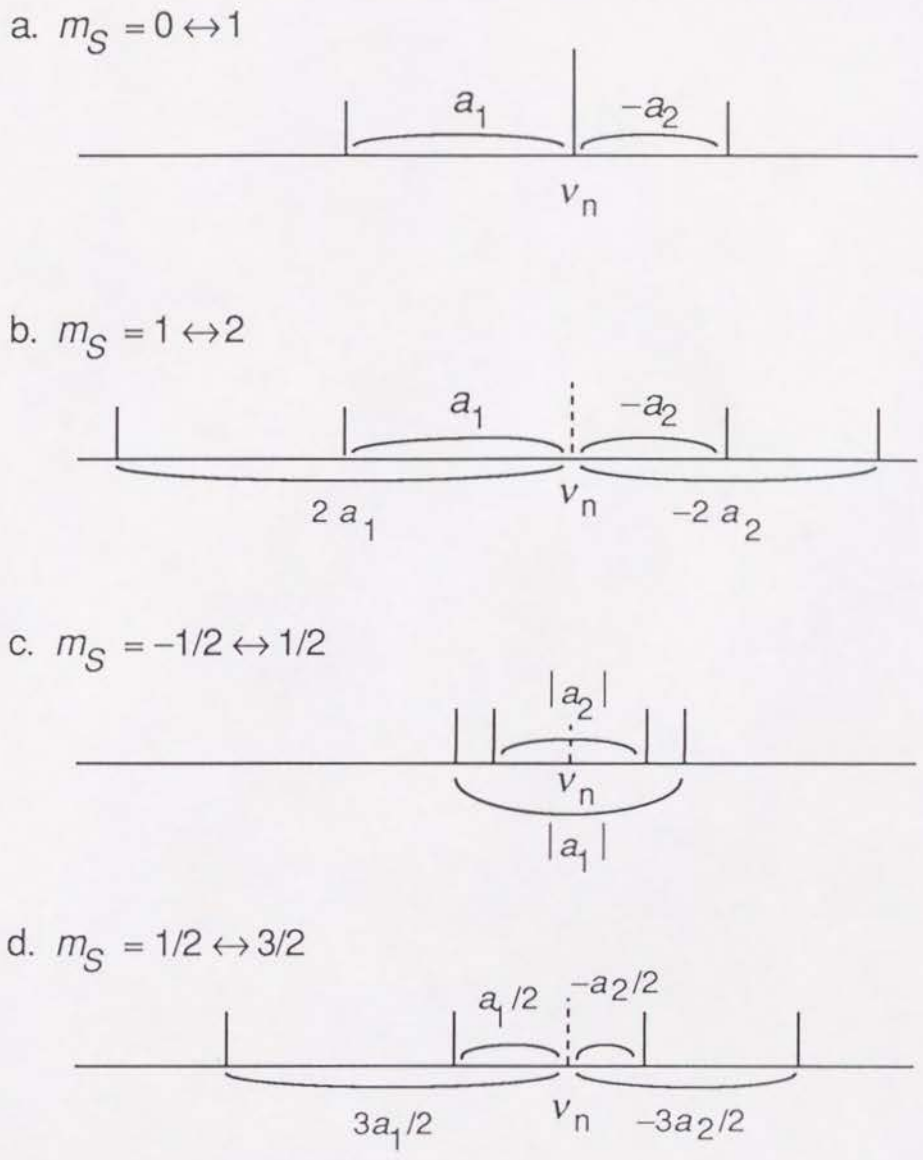

Scheme 1.1. The schematic pattern of the ^{1}H-ENDOR spectra of high-spin states. The model system having two protons of hfcc's of $a_1 > 0$ and $a_2 < 0$ with $|a_1| > |a_2|$ is assumed. The typical patterns for integral-spin states are shown in Schemes 1a and b and those for half-integral spin states are shown in c and d. Schemes 1a, b, c, and d represent the patterns for the transitions from $m_S = 0$ to 1, 1 to 2, −1/2 to 1/2. 1/2 to 3/2. respectively.

transition from $m_S = 1$ to 2. For half-integral spin states also. there are two characteristic ENDOR patterns: One is that obtained by monitoring the transition between $m_S = -1/2$ and 1/2. In this case the ENDOR spectrum is symmetric with respect to ν_n and the hfcc can be determined from the separation of the pair of the signals located symmetrically with respect to ν_n, although the sign of the hfcc cannot be determined from this spectrum (see Scheme 1.1c). The other patterns are asymmetric as is shown in Scheme 1.1d for the transition from $m_S = 1/2$ to 3/2. Since the proton having the hfcc of a gives two peaks at $\nu_n - 3/2\ a$ and $\nu_n - 1/2\ a$, the sign of a can be determined from the paired sets of the ENDOR signal in this case. In most actual cases the electronic spin functions cannot be regarded to be fully quantized along the external magnetic field because of the breakdown of the high-field approximation due to the non-negligible electron spin-spin interaction. As a result, analysis of the ENDOR spectra becomes more complicated than in the case of the high-field approximation discussed above.

The ^{1}H-ENDOR spectra of the monoanion were measured by monitoring the X, Y, Z-axis canonical peaks and the off-axis extra line denoted by A in Figure 1.3. The ENDOR signal corresponding to the Z-axis direction could not be detected because the ESR intensity was too weak. Figure 1.5 shows the ENDOR spectra observed by monitoring the four different ESR peaks. Since the ENDOR signals were very weak, each spectrum was obtained by accumulating the signals over hundreds of scans. It should be noted that the ENDOR spectra obtained by monitoring ESR transitions from $m_S = 1/2$ to 3/2 sublevels (Figures 1.5c and d) are approximately symmetric with respect to ν_n in accordance with the explanation above. The ENDOR signals due to the individual fourteen protons cannot be completely separated. The inhomogenity in a glassy solution will prevent the complete selection of the orientation by monitoring the canonical peaks or the extra-line. Therefore, we are forced to a semi-quantitative argument in the following.

The neutral *m*-PBPM has four singly occupied molecular orbitals (SOMO's), two of which are the non-bonding π-orbitals and the other are the in-plane n-orbitals at the two divalent carbon atoms [Itoh (1967, 1978)]. Therefore, the excess electron of the anion could occupy either the π or the n-orbital. If it occupies the π-orbital, the spin density in the π-system will be halved. On the other hand, if the excess electron resides on the n-orbital, the spin density of the π-electron system would be essentially unchanged but one of the n-orbitals be fully occupied by two electrons and the other remain singly occupied.

For the comparison of the hfcc's of the quartet anion with the neutral quintet *m*-PBPM, the difference of the electron spin multiplicity must be taken into account. According to the projection theorem [Rose (1957)], the isotropic hfcc of a state with the total electron spin angular momentum S is represented as

$$a_i = \frac{1}{2S}\frac{2}{3}\mu_0 g_e \beta g_n \beta_n \rho_i \qquad (1.4)$$

where a_i denotes the isotropic hfcc of the ith nucleus and ρ_i is the spin density at the position of the nucleus. The anisotropic part also contains the projection factor $1/2S$. Thus, the relation between the hfcc of quartet and quintet states is given as follows.

$$a_i(\text{quartet}) = \frac{4}{3}\frac{\rho_i(\text{quartet})}{\rho_i(\text{quintet})} a_i(\text{quintet}) \qquad (1.5)$$

From eq. (1.5) the hfcc's of the protons of the anion will be 2/3 of those of the quintet molecule if the excess electron occupies one of the two π-SOMO's, whereas they will be 4/3 if the electron occupies the n-orbital.

The hfcc's of all the fourteen protons of the neutral *m*-PBPM have been fully analyzed using single crystalline samples to reveal that the isotropic hfcc's are in the range of −8.0 to +3.6 MHz and that the magnitude of the anisotropic part is within ≈4 MHz [Takui *et al.* (1989)]. Therefore, the isotropic hfcc's of the π-anion will be in the range of −5.3 to +2.4 MHz and the maximum (negative) value of the hfcc including the anisotropy will be ≃−8 MHz. In the case of n-anion the isotropic part will span a range of −11 to 5 MHz.

In all the four observed ENDOR spectra of the quartet anion, the maximum absolute values of hfcc's are less than 10 MHz and most of the intensities are within a few MHz around ν_n as is seen from Figure 1.5. The orientations of the anion which were pumped in the ENDOR measurements correspond to the X and Y-canonical axes and to the direction of $\theta \simeq 38°$ for the extra line [Teki *et al.* (1988)] (see Figure 1.3). Although the hfcc of the Z-direction could not be observed due to the feebleness of the ESR intensity, the result of the observed spectra of the three different directions indicates that the isotropic component decreases upon charging, which leads to the conclusion that the excess electron occupies most probably the π-orbital.

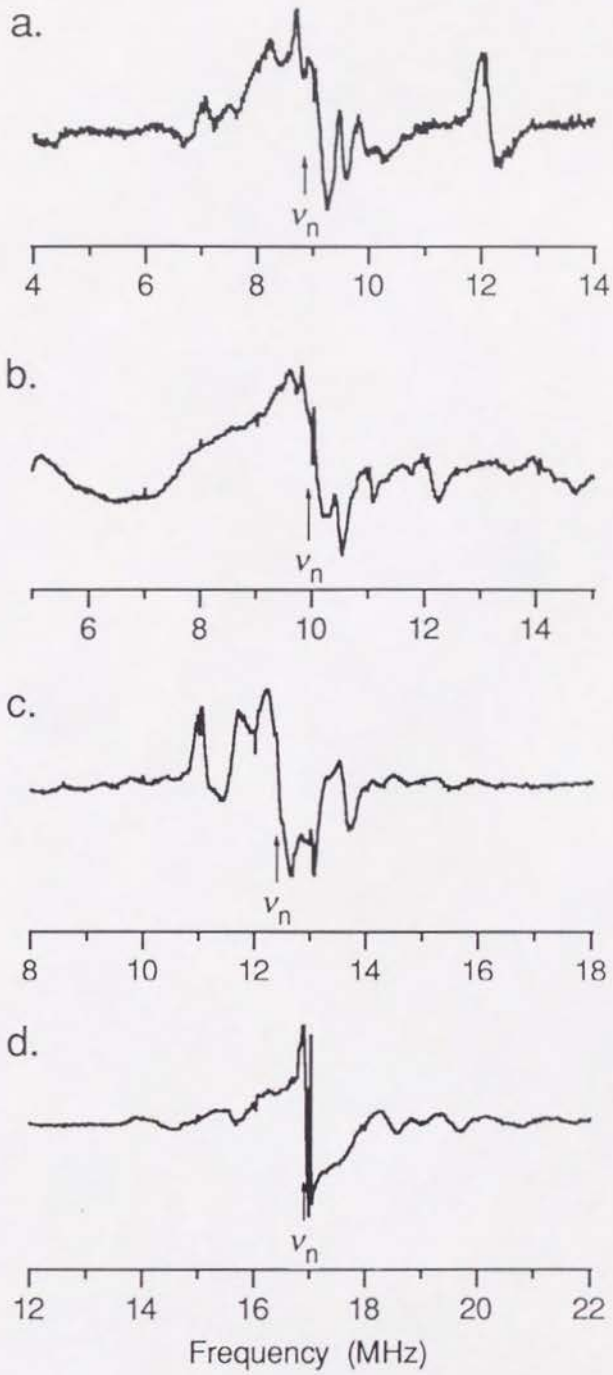

Figure 1.5 ^{1}H-ENDOR spectra of *m*-PBPM$^{-\bullet}$ in glassy solid of MTHF. The measurements were performed at 1.8 K. The magnetic field employed and the number of scans in each measurement were as follows:
a. 207.8 mT (*Y*-axis canonical peak of the transition from m_S = -3/2 to -1/2 sublevels) with 400 scans. **b.** 233.3 mT (*X*-axis canonical peak of the transition from m_S = -3/2 to -1/2 sublevels) with 321 scans. **c.** 291.3 mT (*X* and *Y*-axis canonical peaks of the transition from m_S = -1/2 to 1/2 sublevles) with 400 scans. **d.** 397.0 mT (extra-line of the transition from m_S = -1/2 to 1/2 sublevels) with 301 scans.

6. ESR spectrum of the ^{13}C isotopomer. When the excess electron in the anion occupies the π-orbital, the spin density of the n-orbital should remain essentially the same as that of the neutral quintet *m*-PBPM and the two divalent carbon atoms in the anion will have nearly the same isotropic hfcc. In order to see whether this is the case or not, we have prepared an isotopomer in which one of the two divalent carbon atoms is substituted by ^{13}C. All the canonical peaks and the off-axis extra line are broadened by the unresolved hyperfine splitting due to ^{13}C. The *Y*-axis canonical peak at 200 mT of the ^{13}C isotopomer appears less acute bell-shaped with a larger line-width than the unsubstituted (see Figure 1.6).

According to the above discussion on the π-anion the spin density at both divalent carbon atoms, ^{12}C and ^{13}C, should be nearly the same. Therefore, the observed peak should split into a doublet due to the hyperfine splitting of the single ^{13}C. This is indicated by the two dotted components with an assumed hyperfine splitting of 3.0 mT (see the left pattern of Figure 1.6b). On the other hand, if the excess electron resides in the n-orbital, the spin density at one of the two divalent carbon atoms with a closed-shell structure will be zero whether the atom is ^{12}C or ^{13}C and the density at the other atom with an open-shell structure will be essentially the same as the quintet *m*-PBPM whose hfcc of the divalent ^{13}C atom is known to be ≃3.5 mT [Teki *et al.* to be published.]. Therefore, in this case of n-anion the observed peak should comprise, with an equal intensity, a singlet and a doublet. In the right pattern of Figure 1.6b a singlet and the two components of the doublet are shown in dotted lines where the hyperfine splitting of the doublet is assumed to be 3.0 mT in conformity with the left pattern of Figure 1.6b. The integrated intensity of the singlet is the same as that of the doublet and they are halved relative to the integrated intensity of the doublet in the case of the π-anion above. The observed peak coincides with the former case and not with the latter case, which reenforces the conclusion of the previous subsection that the π-anion is favored over the n-anion. The anisotropic component of the hfcc is totally neglected in the analysis of the *Y*-axis canonical peak at ≃200 mT. However, because all the other *X* and *Y*-axis canonical peaks can be regarded as comprising the two components with a separation of ≃3.0 mT, the isotropic part of the hfcc's of the two divalent carbon atoms are considered to be approximately equal, which is consistent with the conclusion of the π-anion. The neglected anisotropic components of the hfcc could not be analyzed because the hyperfine splittings were not resolved enough for the analysis. The line-shape of all the *Z*-axis canonical peaks could not be analyzed since the signals were too weak.

Since the accurate hfcc cannot be obtained from the above argument based on the line-shape of the ESR signal, we attempted to observe the ^{13}C-ENDOR signal. However, the signal to noise ration was too small to detect the signal.

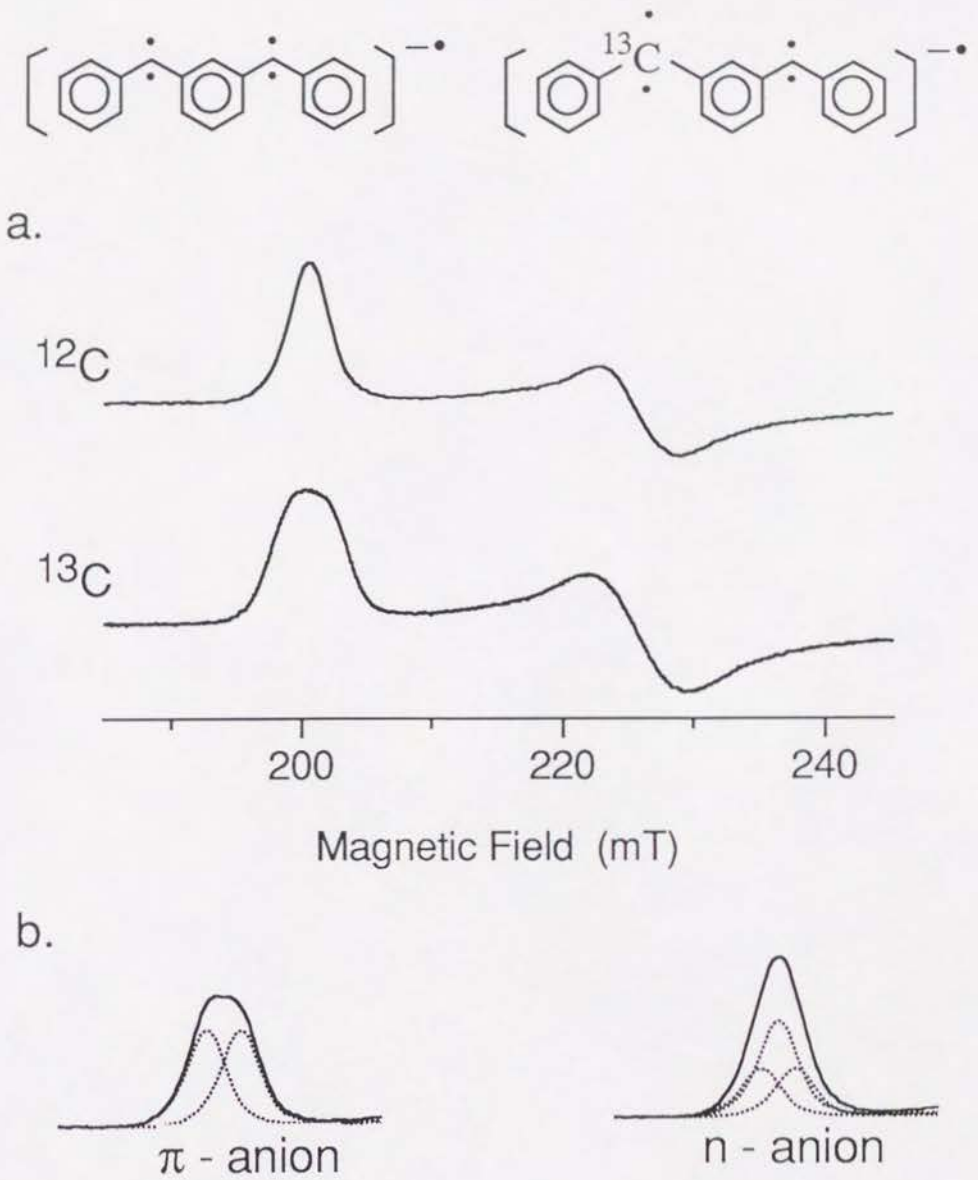

Figure 1.6a. ESR spectrum of ^{13}C substituted *m*-PBPM$^{-\bullet}$ in which one of the two divalent carbon atoms was replaced by ^{13}C. The spectrum of the un-substituted is also shown for comparison.

b. Synthetic peaks consisting of ^{12}C isotopomers. Left; the one corresponding to the spectrum of the π-anion of ^{13}C isotopomer which has a single ^{13}C hfcc of 3.0 mT. Right; the one corresponding to the spectrum of the n-anion of ^{13}C isotopomer which has ^{13}C hfcc's of 0 mT and 3.0 mT.

The isotropic hfcc of the divalent ^{13}C atom of the anion is expected to be nearly equal to that of the neutral *m*-PBPM which is ≃3.5 mT [Teki *et al.* to be published.], whereas the isotropic hfcc of the divalent ^{13}C atom of diphenylmethylene (DPM) is reported as 173.3 MHz (6.184 mT) [Brandon *et al.* (1965)]. Since the spin density of the n-orbital of DPM and *m*-PBPM is essentially the same, eq. (1.4) predicts that the isotropic hfcc of the divalent ^{13}C atom of *m*-PBPM is 1/2 of that of DPM, which agrees with the observation. Thus, the semi-quantitative argument here works fine in the neutral systems. However, the isotropic hfcc of the anion of ≃3.0 mT does not agree with the estimation based on eq. (1.5) which predicts that the hfcc of the anion should be 4/3 of that of the neutral *m*-PBPM, i.e., ≃4.7 mT. Plausible reasons for the discrepancy are an incomplete separation of the π-orbitals and n-orbitals and the change of the C-C-C angle at the divalent carbon atom upon charging which should change the ratio of s-p mixing in the in-plane n-orbital.

7. Conformation of *m*-PBPM$^{-\bullet}$. Since the fine structure parameters of the anion are now determined as $D = +0.1200\ \mathrm{cm}^{-1}$ and $|E| = 0.0045\ \mathrm{cm}^{-1}$ and the excess electron is in the p-orbital, we can discuss the conformation of the anion by comparing the fine structure parameters with those of diphenylmethylene (DPM) and *m*-PBPM: We employ a semi-quantitative expression for the fine structure tensor that was used for the determination of the conformation of the nonet tetracarbene [Teki *et al.* (1986)]. In ordinary non-degenerate electronic states the fine structure tensor $\boldsymbol{D}$ is expressed by the electron spin-spin interaction, because the second order perturbation of the spin-orbit interaction is usually negligibly small in hydrocarbons. When the electronic state of the molecule is approximated by a single electronic configuration, the *ij* component of the fine structure tensor is given by eq. (1.6) [Higuchi (1963a)].

$$D_{ij} = -\left(\frac{e^2\hbar^2}{2m^2c^2}\right)\frac{2!(2S-2)!}{(2S)!} \times \sum_{p,q} \langle p(1)q(2) - q(1)p(2) | \frac{3i_{12}j_{12} - r_{12}^2\delta_{ij}}{r_{12}^5} | p(1)q(2)\rangle \qquad i, j = X, Y, Z \qquad (1.6)$$

where $p(i)$ and $q(i)$ are the molecular orbitals occupied by the i'th electron. In aromatic polycarbenes such as *m*-PBPM, the one-center n-π interaction at a divalent carbon atom is dominant in comparison with other combinations of spin-spin interaction [Higuchi (1963a, b)]. Neglecting the latter, eq (1.6) becomes

$$D_{ij} = [S(2S-1)]^{-1} \sum_k \rho_k \left(\mathbf{U}_k \cdot \mathbf{d} \cdot \mathbf{U}_k^{-1}\right)_{ij} \qquad (1.7)$$

where

$$d_{ij} = -\left(\frac{e^2\hbar^2}{2m^2c^2}\right)\langle n(1)\pi(2) - \pi(1)n(2)|\frac{3i_{12}j_{12} - r_{12}^2\delta_{ij}}{r_{12}^5}|n(1)\pi(2)\rangle \qquad (1.8)$$

The subscript k runs over all the divalent carbon atoms and the symbol ρ_k denotes the spin density of the π-electron at the kth divalent carbon atom. The tensor **d** represents the fine structure tensor due to the one-center spin-spin interaction between n and π-electrons at a divalent carbon atom. The orthogonal matrix $\mathbf{U}_k$ transforms the principal axes of the tensor **d** at the kth divalent carbon atom to the molecule fixed axes. The tensor **d** can be approximated as $\mathbf{D}_{\mathrm{DPM}}/\rho_{\mathrm{DPM}}$, where $\mathbf{D}_{\mathrm{DPM}}$ and ρ_{DPM} are the fine structure tensor and the π-electron spin density on the divalent carbon atom of diphenylmethylene, respectively. Thus, we obtain the semi-empirical expression for the fine structure tensor [Teki *et al.* (1986)],

$$D_{ij} = [S(2S-1)]^{-1}\sum_k (\rho_k/\rho_{\mathrm{DPM}})\left(\mathbf{U}_k \cdot \mathbf{D}_{\mathrm{DPM}} \cdot \mathbf{U}_k^{-1}\right)_{ij}$$
$$i, j = X, Y, Z \qquad (1.9)$$

Since a simple LCAO-MO calculation gives the spin densities of $\rho_{\mathrm{DPM}} = 2/5$ and $\rho_{m\text{-PBPM}} = 0.4040$, the ratio $\rho_{m\text{-PBPM}}/\rho_{\mathrm{DPM}}$ can be regarded as unity. We must take into account the projection factor $[S(2S-1)]^{-1}$ which is 1 for the triplet DPM, 1/3 for the quartet anion, and 1/6 for the quintet *m*-PBPM. Since the excess electron of the anion occupies the π-orbital, the π-electron spin density will be reduced to $\rho_k \simeq \rho_{m\text{-PBPM}}/2$.

If the conformation of the anion remains the same as that of the neutral *m*-PBPM which is known to assume Conformation A shown below [Itoh (1978)], the orthogonal matrices $\mathbf{U}_k$'s should be almost the same as those of the neutral *m*-PBPM. Noticing that the projection factor of the anion is twice as large as that of *m*-PBPM together with the relation of $\rho_k(\text{anion}) \simeq \rho_{m\text{-PBPM}}/2$, we find $D_{ij}(\text{anion}) = D_{ij}(m\text{-PBPM})$. Thus, the fine structure parameters of the anion would have to be close to those of the neutral *m*-PBPM, i.e., D = +0.07131 cm^{-1} and $|E| = 0.01902\ \mathrm{cm}^{-1}$ [Itoh (1967)]. However, the observed parameters of the anion are far from those of *m*-PBPM. The $|E/D|$ value for the anion, 0.038, which is the measure of the deviation from the axial symmetry of the tensor, is also quite different from that for *m*-PBPM, i.e., 0.2667 (see Table 1.1).

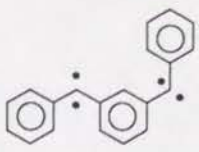

A

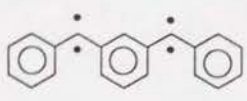

B

However, if the conformation of the anion is in a trans-trans type as depicted in B, the two one-center interaction tensors at the divalent carbon atoms are roughly parallel so that the sum in eq. (1.9), $\sum_k (\rho_k/\rho_{DPM})(\mathbf{U}_k \cdot \mathbf{D}_{DPM} \cdot \mathbf{U}_k^{-1})_{ij}$, will be close to $1/2 \times 2\mathbf{D}_{DPM} \simeq \mathbf{D}_{DPM}$. Since the projection factor $[S(2S-1)]^{-1}$ is 1 for DPM and 1/3 for the anion, the fine structure parameters of the anion will be about 1/3 of those of DPM. The fine structure parameters of DPM are $D = +0.40505$ cm^{-1} and $|E| = 0.01918$ cm^{-1} with the $|E/D|$ value being 0.04735 [Brandon *et al.* (1965)]. From these values the parameters of the anion are estimated as $D \simeq D(\text{DPM})/3 = +0.135$ cm^{-1}, $|E| \simeq |E(\text{DPM})|/3 = 0.0064$ cm^{-1}, and $|E/D| \simeq |E/D(\text{DPM})| = 0.0047$, which are close to the experimental values for the monoanion, $D = +0.1200$ cm^{-1}, $|E| = 0.0045$ cm^{-1}, and $|E/D| = 0.0038$ (see Table 1.1).

Using the fact that the fine structure tensor of aromatic polycarbenes can be approximated as the superposition of the one-center interaction at each divalent carbon atom and the p-electron spin density of the anion is about one half of that of *m*-PBPM, the conformation of the anion is now suggested as to be in a trans-trans type such as B.

Table 1.1 Comparison of D, $|E|$, and $|E/D|$ of monoions of *m*-phenylenebis(phenylmethylene) (*m*-PBPM) with those of diphenylmethylene (DPM) and the neutral *m*-PBPM.

		S	D (cm^{-1})	$\lvert E\rvert$ (cm^{-1})	$\lvert E/D\rvert$
diphenylmethylene (DPM)[a]		1	+0.40505	0.01918	0.04735
m-phenylenebis(phenylmethylene) (*m*-PBPM)[b]		2	+0.07131	0.01902	0.2667
monoanion of *m*-PBPM[c]		3/2	+0.1200	0.0045	0.038
monocation of *m*-PBPM	conformer I[d]	3/2	+0.1350	0.0040	0.030
ditto	conformer II[d]	3/2	+0.1285	0.0055	0.043

[a]Brandon *et al.* (1965).

[b]Itoh (1967).

[c]Matsushita *et al.* (1990b).

[d]Matsushita *et al.* to be published.

Results and discussion for a monocation of *m*-PBPM (*m*-PBPM$^{+\bullet}$)

1. Optical and ESR spectra. The solution of 1,3-BDB in BuCl becomes a glassy solid at 77 K with purple color (see curve 1 in Figure 1.7). The color is ascribable to the $n\pi^*$-transition of diazo group with $\varepsilon = 254$ at $\lambda_{max} = 530$ nm [Itoh *et al.* (1968)]. From the value of ε, we can estimate the concentration of the dissolved 1,3-BDB as 5 – 10 mM. The samples were γ-irradiated at 77 K. As described in Chapter 0 the major products of the reactions upon γ-irradiation are the butyl radical, the chloride anion, and the radical cation of 1,3-BDB. It is emphasized that high energy γ photon does not cause violent radiolysis to extensive fragmentations of the solvent and the solute but result mostly in thermal ionization of the solute by the intermolecular charge transfer (see reaction (0.7)). The possibility of formation of dication is ignorable because of the Coulombic repulsion between two positive charges. The electron absorption spectrum at this stage is shown in curve 2 of Figure 1.7. Since the butyl radical and the chloride anion are colorless in the observed region, the spectrum in curve 2 is attributed to the radical cation of 1,3-BDB, although part of the $n\pi^*$-transition due to the intact 1,3-BDB (curve 1) is superposed. The absorption spectrum of curve 2 has a characteristic peak at 630 nm in contrast to the absorption spectrum of γ-irradiated 1,3-BDB in MTHF solution, which exhibits strong absorption at $\lambda < 500$ nm and feeble absorption in the near-IR region (see curve 2 in Figure 1.1). The difference between the two spectra clearly indicates that the species produced by γ-irradiation in BuCl is different from that in MTHF and reenforces the assignment that the former is the radical cation and the latter the radical anion of 1,3-BDB. A further confirmation of this assignment of 1,3-BDB$^{+\bullet}$ was made by running a parallel optical study of a solution of 1,3-BDB ($\approx$10 mM) plus triethylamine (TEA, $\approx$100 mM) in BuCl; since TEA is known to be an efficient positive charge scavenger [Shida *et al.* (1984), Shida (1988, 1991)], the yield of the absorption in curve 2 of Figure 1.7 should be suppressed drastically, which was indeed observed.

The X-band ESR spectrum after γ-irradiation showed signals in a range of 0.32 – 0.34 T as shown in the inset of Figure 1.8, which is consistent with the formation of the spin-doublet 1,3-BDB$^{+\bullet}$ and the butyl radical.

When the γ-irradiated sample exhibiting the optical spectrum in curve 2 of Figure 1.7 was photolyzed with $\lambda > 620$ nm, several new ESR signals appeared in the range of the magnetic field 0 – 0.6 T (see Figure 1.8). Concomitantly, the optical spectrum changed from curve 2 to 3 in Figure 1.7. The appearance of new ESR signals indicates the formation of a new high-spin species. Since these signals did not appear in the experiment of the 1,3-BDB + TEA/BuCl system, the new signals are associated with a high-spin species originating from the radical cation of 1,3-BDB. By analogy of the photolytic

denitrogenation of the parent 1,3-BDB molecule [Itoh (1967)], the observed spectral change is accounted for by the following series of reaction.

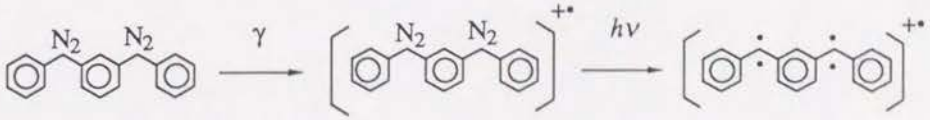

(1.10)

1,3-BDB 1,3-BDB$^{+\bullet}$ *m*-PBPM$^{+\bullet}$

Since γ-irradiation of BuCl solution at 77 K should lead solely to the monocation of the solute molecule, and since photon energy in reaction (1.10) is less than ≈2 eV, there is no possibility of the photoionization to the dications of 1,3-BDB or *m*-PBPM in reaction (1.10). Since only the doublet and the quartet is allowed for the spin multiplicity of *m*-PBPM$^{+\bullet}$, the fine structure observed at 0 – 0.6 T must be associated with *m*-PBPM$^{+\bullet}$ in the quartet state. The accompanying optical change from curve 2 to 3 in Figure 1.7 is, thus, attributed to the formation of quartet *m*-PBPM$^{+\bullet}$. Since the optical absorption spectrum shown in curve 3 is different from the corresponding spectrum of the anionic system of MTHF solution, the spin quartet species generated in BuCl must be different from that in MTHF even if the ESR spectrum in Figure 1.8 resembles to some extent the spectrum of the monoanion of *m*-PBPM. The resemblance will be discussed later invoking the pairing theorem of conjugated π-electron systems [McLachlan (1959, 1961), Koutecký (1966)]. A closer analysis of the observed ESR spectrum in Figure 1.8 reveals that there are two conformers of *m*-PBPM$^{+\bullet}$ as will be discussed in the following section.

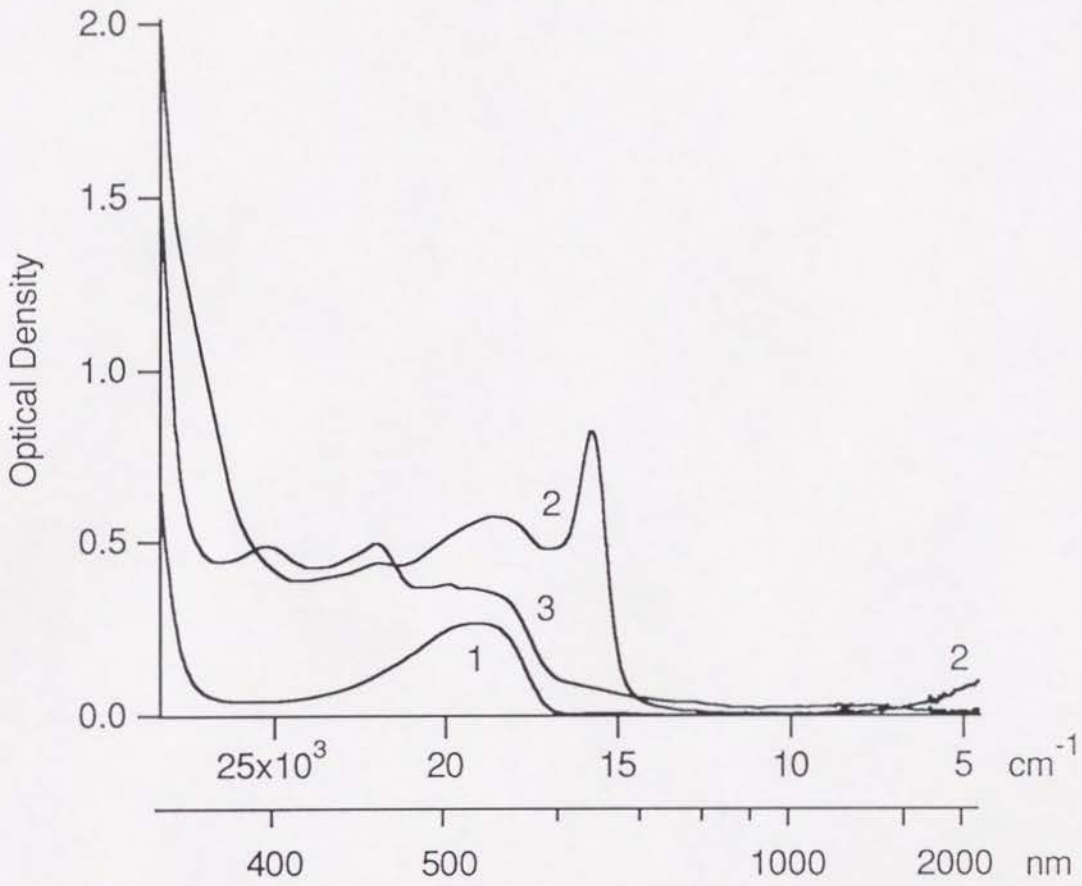

Figure 1.7 Optical absorption spectra of 1,3-BDB/BuCl solution at 77 K:
1, Before γ-irradiation.
2, After γ-irradiation.
3, Same as 2 but followed by photolysis with $\lambda > 550$ nm.
Optical path length 1.5 mm.

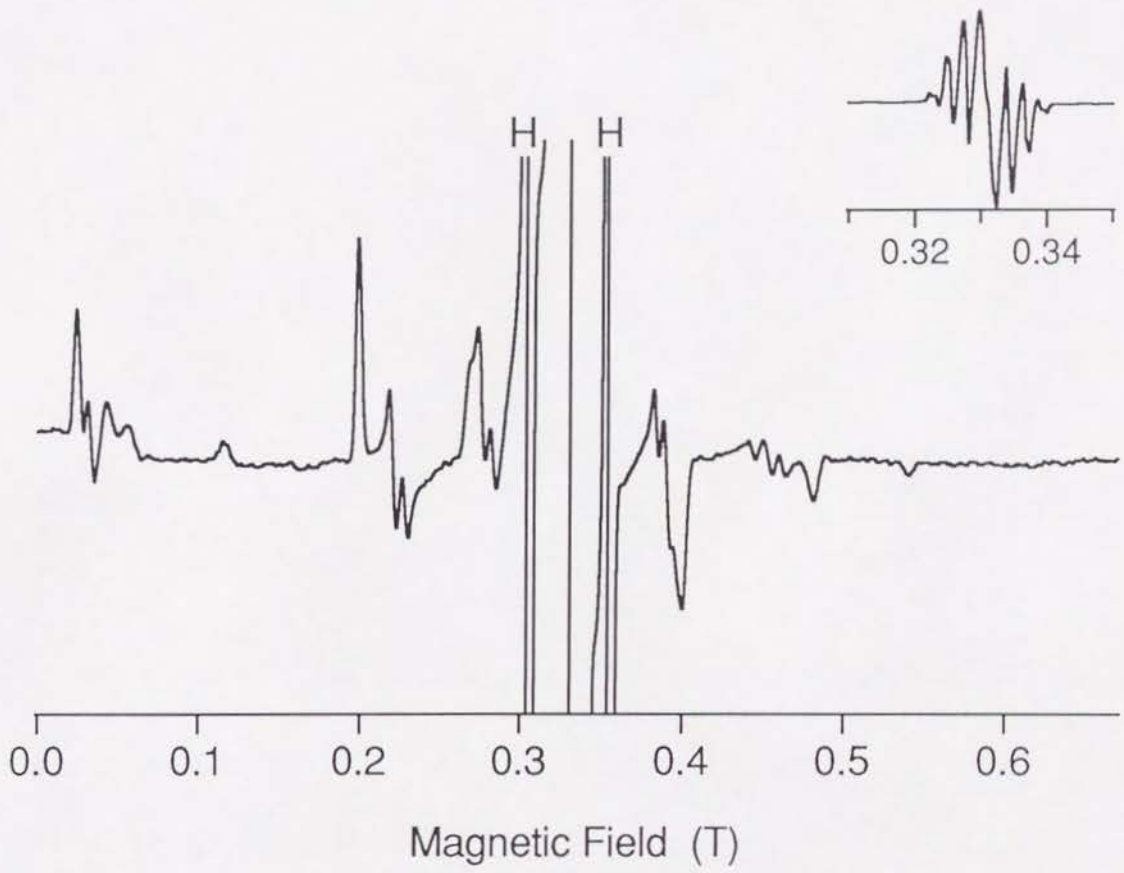

Figure 1.8 X-Band ESR spectra for a γ-irradiated and subsequently photolyzed 1,3-BDB/BuCl solution at 36 K. Prior to photolysis the spectrum showed only the signal at 0.32 −0.34 T, which is shown in the inset, and the doublet due to the hydrogen atom produced in the quartz cell by γ-irradiation. Upon photolysis several new peaks appeared in the ESR spectrum over a wide range of 0 − 0.6 T. The new peaks are assigned to the spin quartet state of *m*-PBPM$^{+\bullet}$.

2. Analysis of the X-band ESR spectrum of *m*-PBPM$^{+\bullet}$. As in the case of the monoanion of *m*-PBPM [Matsushita *et al.* (1990b)], the ESR assignment was confirmed by the simulation based on the following spin Hamiltonian.

$$\mathcal{H} = g\beta\tilde{\mathbf{S}}\cdot\mathbf{H} + D\left[S_Z^2 - S(S+1)/3\right] + E\left(S_X^2 - S_Y^2\right) \qquad (1.2)$$

The Hamiltonian corresponding to a particular orientation of the magnetic field was diagonalized to obtain the resonant field and the transition probability. Then, the spectrum was summed up over one eighth of the whole spherical angle to get the powder-pattern spectrum (see Appendix B). The total 13,000 orientations were sampled and a common Gaussian line-width of 4.0 mT was assumed.

After several trials of simulation we concluded that the observed spectrum is a superposition of two spin-quartet constituents having slightly different fine structure parameters. The spectrum at the bottom of Figure 1.9 shows the constituent spectra and the one in the middle is their superposition. For the sake of convenience the principal axis transitions X and Y are labeled under the assumption of $D > 0$ (which was found to be the case (see below)) and $E > 0$. In the superposed spectrum the low and the high-field pairs of the *Y*-axis canonical peaks coincide accidentally and the corresponding pairs of the *X*-axis peaks show a doublet structure. These features are in a good agreement with the observed spectrum. Likewise, the other pairs of the *X* and *Y*-axis peaks and "forbidden" transitions of $\Delta m_S = \pm 2$ and ± 3 marked by F as well as the off-axis extra lines denoted by A altogether give a satisfactory agreement with the observed spectrum. However, the predicted *Z*-axis canonical peaks are not seen in the observed spectrum because the low and the middle-field peaks are hidden by the signals of by-produced triplet carbenes and doublet radicals, respectively. The high-field *Z*-axis peaks also cannot be distinguished from the noise because of the weak intensity. In order to confirm the generation of the two conformers, the high-field *Z*-axis canonical peaks were disclosed by averaging the signals over 100 times of scans. The detected spectrum is shown in Figure 1.10, where the base line correction was carried out. The spectrum reveals the anticipated doublet feature of the *Z*-axis peak. Once the peak positions of the high-field *Z*-axis canonical peaks are known, the fine structure parameter *D* can be determined accurately. Since the fine structure parameters of the two conformers are very close, the difference of the conformations must be small to rule out such a distinct difference as the cis-trans isomerism. It might be that the two conformers are different in the degree of planarity and/or the bond angles at the divalent carbon atoms. The intensities of the two conformers are nearly equal. The best fit parameters are found as to be $g = 2.003$ (isotropic), $D = +0.1350$ cm^{-1}, and $|E| = 0.0040$ cm^{-1} for conformer I and $g = 2.003$ (isotropic), $D = +0.1285$ cm^{-1}, and $|E| = 0.0055$ cm^{-1} for conformer II. The sign of *D* was determined from the effect of Boltzmann factor

on the relative intensity of ESR transitions (see below). The parameters are found to be close to those of the anion of *m*-PBPM (g = 2.003 (isotropic), D = +0.1200 cm^{-1}, and $|E|$ = 0.0045 cm^{-1}) [Matsushita *et al.* (1990b)].

As is mentioned for the spectrum of the monoanion, the off-axis extra lines in the powder-pattern spectrum should be characteristic of the spin multiplicity and the fine structure parameters [Teki *et al.* (1988)]. Figure 1.11 shows the calculated angular dependence of resonant fields and powder-pattern first derivative ESR spectra for conformers I and II. The off-axis extra lines denoted by A assure that the observed fine structure pattern, indeed, arises from the spin-quartet species.

At temperatures as low as 1.4 K the relative intensity of ESR transitions in the quartet state should depend sensitively on the thermal population among the sublevels. As the temperature is lowered, the intensity of transitions between higher sublevels should become weak relative to those between lower sublevels. The intensity of the high-field *Y*-axis canonical peak was compared with that low-field peak for the randomly oriented sample. The intensity was calculated by double integration of the first derivative spectrum. From the temperature dependence of the intensity ratio of the high-field to the low-field *Y*-axis peak, the sign of D was determined to be positive. Since the relative intensity of the low-field X-axis canonical peak of conformer I to that of conformer II does not change with the temperature, the ground state of both I and II must be the same, which was found to be quartet as will be discussed in detail in the next section. The same temperature dependence of I and II also implies that the sign of D is the same for the two conformers: If the sign of D were different, the order of sublevels must be reversed, and the low-field *X*-axis peak of one conformer would be due to the transition between the highest two sublevels of the quartet state, whereas that of the other conformer would be the transition between the lowest sublevels.

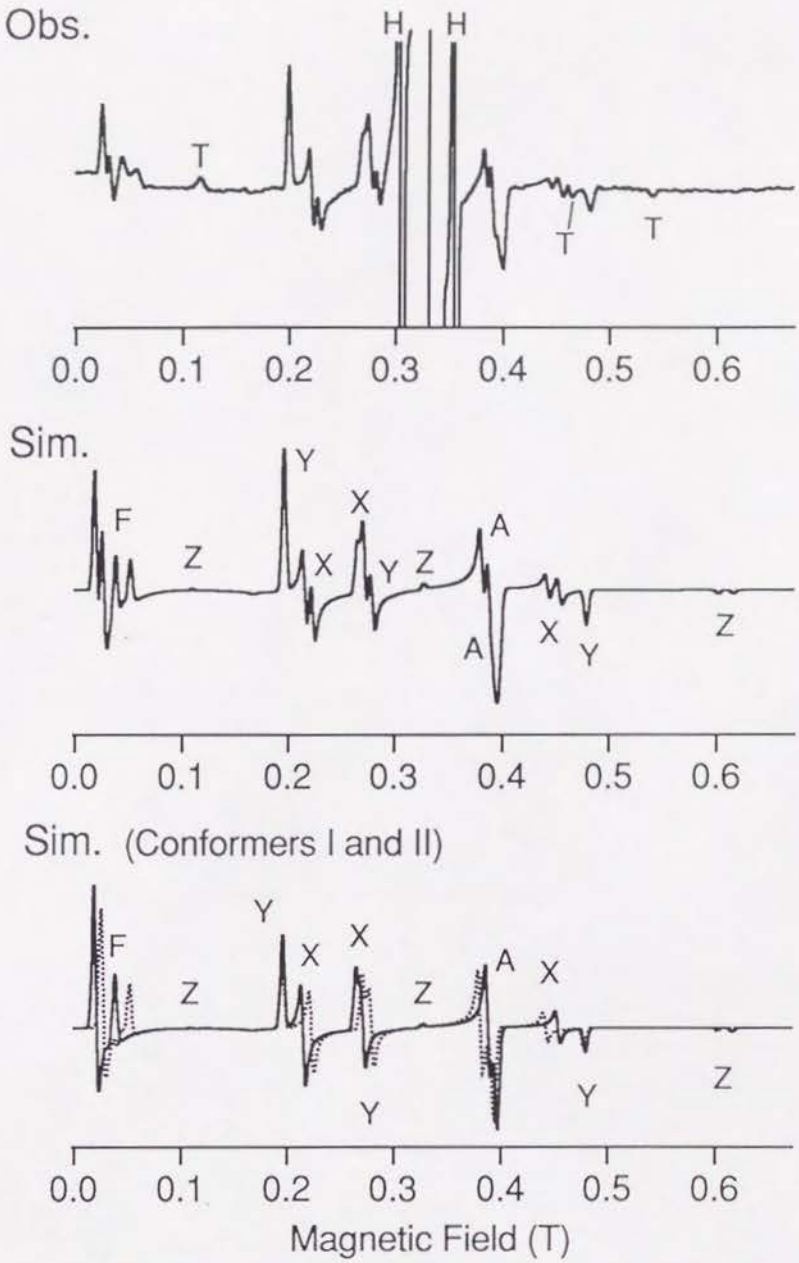

Figure 1.9 Observed and simulated X-band ESR spectra for the quartet state of *m*-PBPM$^{+\bullet}$. The symbol T in the observed spectrum indicates the signals due to by-produced triplet carbenes. Microwave frequency employed is 9.175 GHz. Symbols A and F in the simulated spectra denote the off-axis extra line and the "forbidden" transition with $\Delta m_s = \pm 2$ and 3. The parameters used for the simulation are $g = 2.003$ (isotropic), $D = +0.1350$ cm^{-1}, and $|E| = 0.0040$ cm^{-1} for conformer I and $g = 2.003$ (isotropic), $D = +0.1285$ cm^{-1}, and $|E| = 0.0055$ cm^{-1} for conformer II, and the ratio of conformer I to II is 1:1. The spectrum at the bottom shows the simulated spectra of conformer I (solid line) and II (dotted line) and the spectrum in the middle is the superpotition of the two. The sign of D was determined from the temperature dependence of the ESR spectrum (see the text).

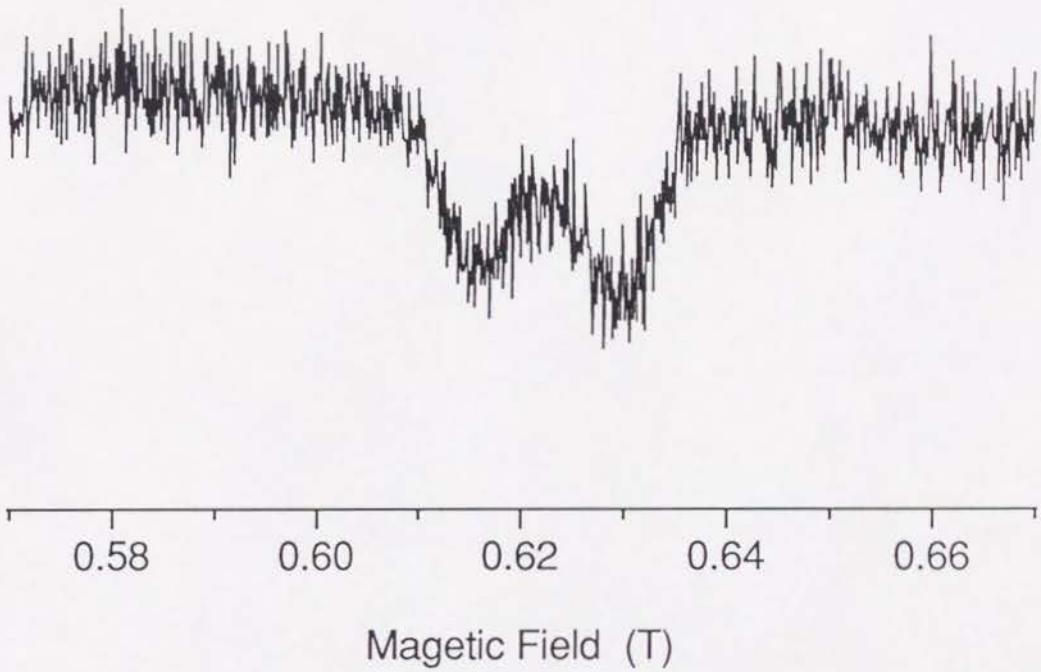

Figure 1.10 Observed X-band ESR spectrum around the high-field Z- axis canonical peak of *m*-PBPM$^{+\bullet}$. The spectrum was obtained by accumulating the signals over 100 times of scans and the base line correction was carried out. Mocrowave frequency is 9.56262 GHz. The doublet structure of the Z-axis peak clearly shows the formation of two conformers of *m*-PBPM$^{+\bullet}$.

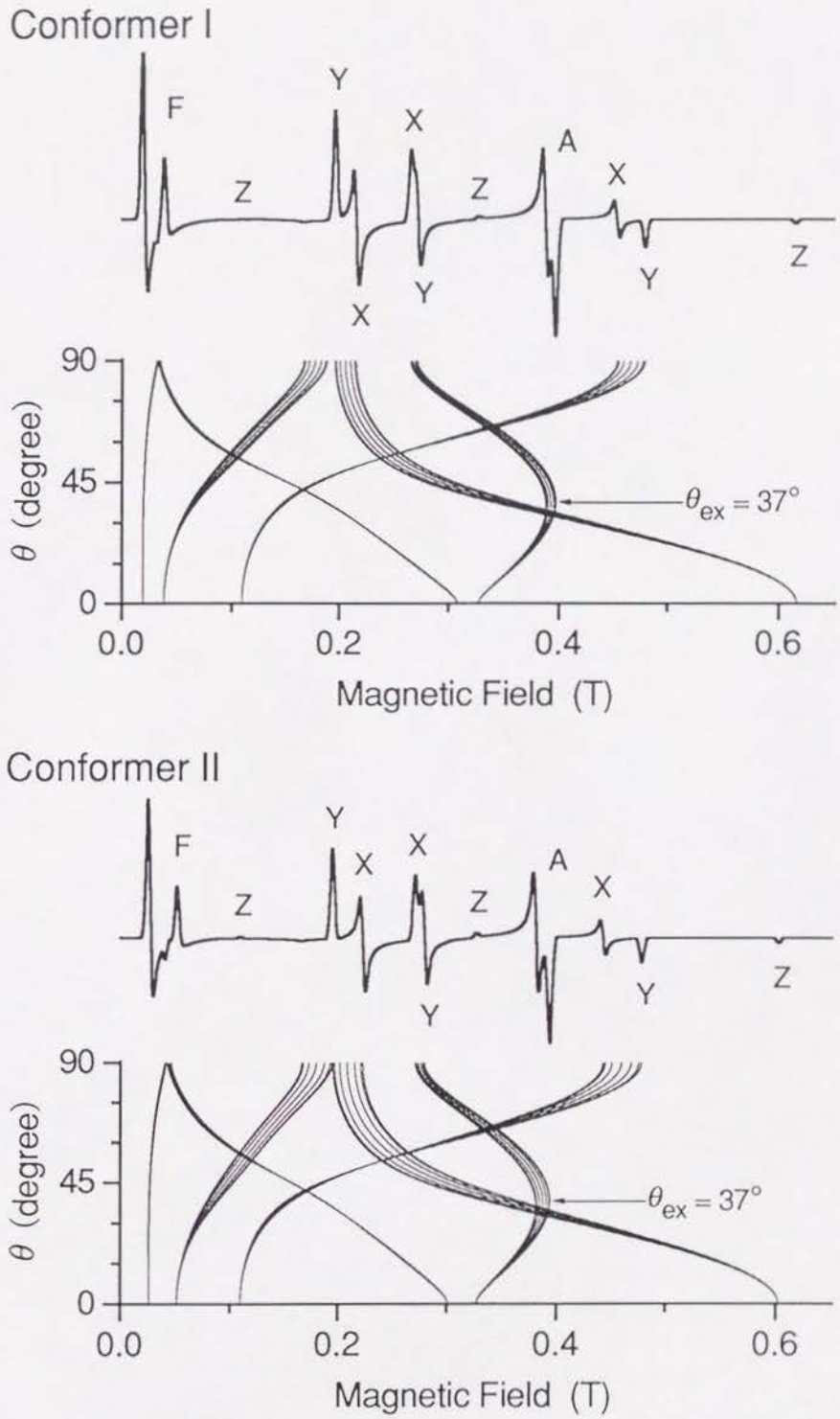

Figure 1.11 Calculated angular dependence of resonance fields and powder-pattern first derivative ESR spectra for conformers I and II of *m*-PBPM$^{+\bullet}$. Microwave frequency is set to be 9.175 GHz. The parameters are $g = 2.003$ (isotropic), $D = +0.1350$ cm^{-1}, and $|E| = 0.0040$ cm^{-1} for conformer I and $g = 2.003$ (isotropic), $D = +0.1285$ cm^{-1}, and $|E| = 0.0055$ cm^{-1} for conformer II. θ_{ex} denotes the angle corresponding to the extra line.

3. Spin multiplicity of the ground state of *m*-PBPM$^{+\bullet}$. To determine the spin multiplicity of the ground state of *m*-PBPM$^{+\bullet}$, the temperature dependence of the intensity of the quartet signal was examined by monitoring the low-field *Y*-axis canonical peak (see the spectrum in Figure 1.12). The intensity was calculated by double integration of the first derivative peak. For the measurement of the temperature of the sample the neutral *m*-PBPM was used as an internal standard of the temperature as in the case of the anionic system. In brief, the γ-irradiated sample was photolyzed to produce the neutral *m*-PBPM from the remaining 1,3-BDB by the well-known denitrogenation [Itoh (1967), Teki *et al.* (1986)]. To get a proper intensity of *m*-PBPM for the comparison with that of the monocation shown in Figure 1.12a, the yield of *m*-PBPM was controlled by using visible light with $\lambda > 510$ nm instead of UV light. By obtaining both *m*-PBPM and its cation in this way, the temperature of the sample was calibrated referring to the signal intensity of *m*-PBPM. The observed intensity is represented by circles in Figure 1.12b. The approximately linear plot indicates that the ground state is quartet.

In order to exclude definitely the possibility that the ground state is doublet, the temperature dependence of the signal was calculated for several values of $\Delta\varepsilon \equiv \varepsilon(\text{quartet}) - \varepsilon(\text{doublet})$ as indicated by solid lines in Figure 1.12b. In the calculation for the curve denoted by $\Delta\varepsilon = -\infty$ the population in the doublet state was totally ignored. The curve of $\Delta\varepsilon = -\infty$ corresponds to the case that the ground state is quartet. Thus, from the observed temperature dependence, it is safely concluded that the ground state of *m*-PBPM$^{+\bullet}$ is quartet.

4. ^{1}H-ENDOR spectra of *m*-PBPM$^{+\bullet}$. The neutral *m*-PBPM has four SOMO's, two of which are the non-bonding π-orbitals and the other two are the in-plane n-orbitals localized at the divalent carbon atoms [Itoh (1967, 1978)]. Therefore, there are two possibilities for the cation, that is, a π- and n-cation as in the case of the anion. In the case of the π-cation, the spin density of the π-orbital will be about one half of that of the neutral *m*-PBPM, whereas it will be almost the same as that of *m*-PBPM for the n-cation. To compare the hfcc of the quartet cation with that of the quintet *m*-PBPM, the difference of the spin multiplicity must be taken into account. According to the projection theorem [Rose (1957)], the hfcc is proportional to $\rho/2S$ where S denotes the total electron spin quantum number and ρ is the spin density. Therefore, for the π- and n-cation the hfcc of the protons will be 2/3 and 4/3 of those of *m*-PBPM.

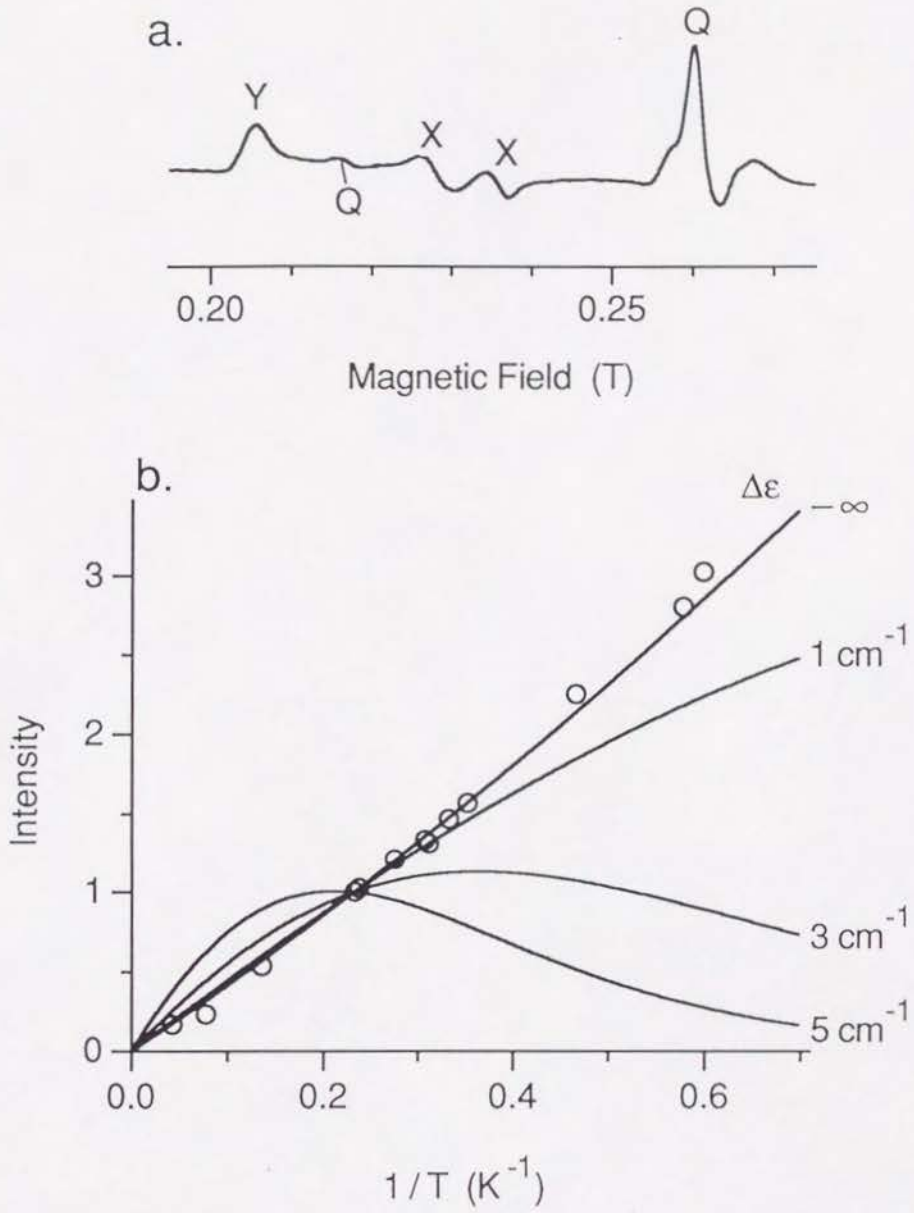

Figure 1.12 **a.** Typical ESR spectrum used for the calculation of the temperature dependence of the low-field *Y*-axis canonical peak of the quartet state. The symbols X and Y indicate the low-field *X* and *Y*-axis canonical peaks of the quartet cation. The signals due to the neutral quintet are denoted by Q. The temperature was calibrated by the intensity of the signal of the neutral *m*-PBPM at ≈0.26 T.

b. Temperature dependence of the intensity of the ESR signal of the low-field *Y*-axis canonical peak. The circles are experimental, and the curves are the calculated for several values of $\Delta\varepsilon = \varepsilon(\text{quartet}) - \varepsilon(\text{doublet})$. All the experimental and theoretical intensities are normalized at T = 4.3 K.

^{1}H-ENDOR spectra were measured by monitoring the *X*, *Y*-axis canonical peaks and the off-axis extra line. The ENDOR signals were weaker than those of the monoanion in MTHF and clear spectra were obtained only for the three ESR peaks at 202.5 mT, 281.4 mT, and 396.1 mT (see Figure 1.9). Since all the three peaks consist of the peaks due to conformers I and II, the observed ENDOR signals are superposition of the signals due to conformer I and those due to conformer II. The weak ENDOR signals were accumulated over several hundred scans to obtain the spectra shown in Figure 1.13. The measurements were carried out at 3.0 K. Since the hfcc due to each proton cannot be distinguished, only a semi-quantitative discussion can be made as in the case of *m*-PBPM$^{-\bullet}$. Each spectrum is quite similar to the corresponding ^{1}H-ENDOR spectrum of the anion. The hfcc's of the protons of the cation should, therefore, be very close to those of the anion. The spin density of the π-orbital of the cation is about one half of that of *m*-PBPM as in the case of the anion; The hfcc's of the cation are within 9 – 10 MHz in all of the observed spectra and most of those are within 2 MHz. They are about 2/3 of those of *m*-PBPM, which are reported as $a_{iso} = -8.0 \sim 3.6$ MHz and $|a_{aniso}| \leq 4$ MHz [Takui *et al.* (1989)]. Thus, it is concluded that the hole in the cation is in the π-orbital.

The close agreement of the hfcc's of the anion and the cation is consistent with the conclusion that both the anion and the cation are of π-type ions, because the pairing theorem [McLachlan (1959, 1961), Koutecký (1966)] should hold good in larger π-systems [Weissman *et al.* (1957), Boer and Weissman (1958), Carrington *et al.* (1959)]. The difference in the optical absorption spectra of the anion and the cation does not contradict the agreement of the hfcc's, because both of the electronic ground and excited states are involved in the absorption spectrum whereas the hfcc is determined by the spin density distribution of the electronic ground state.

The observed ENDOR spectra of Figure 13a, b, and c correspond to the orientation of the principal *Y*-axis, *X* and *Y* axes ($\theta = 0°$), and the direction of the extra-line [Teki *et al.* (1988)] ($\theta = 37°$), respectively. Although the observed ENDOR spectra are the superposition of the signals due to conformer I and conformer II, the hfcc's in the three different directions agree fairly well with those of the monoanion. Therefore, the orientations of each hfcc tensor of the two conformers should be close to each other and also close to that of the monoanion. Thus, we can expect that the conformations of the two conformers of the cation and the conformation of the anion are basically similar. Then, the fine structure parameters of the cation should be close to those of the anion, which was indeed observed. The conformation of the cation will be discussed further in a later section.

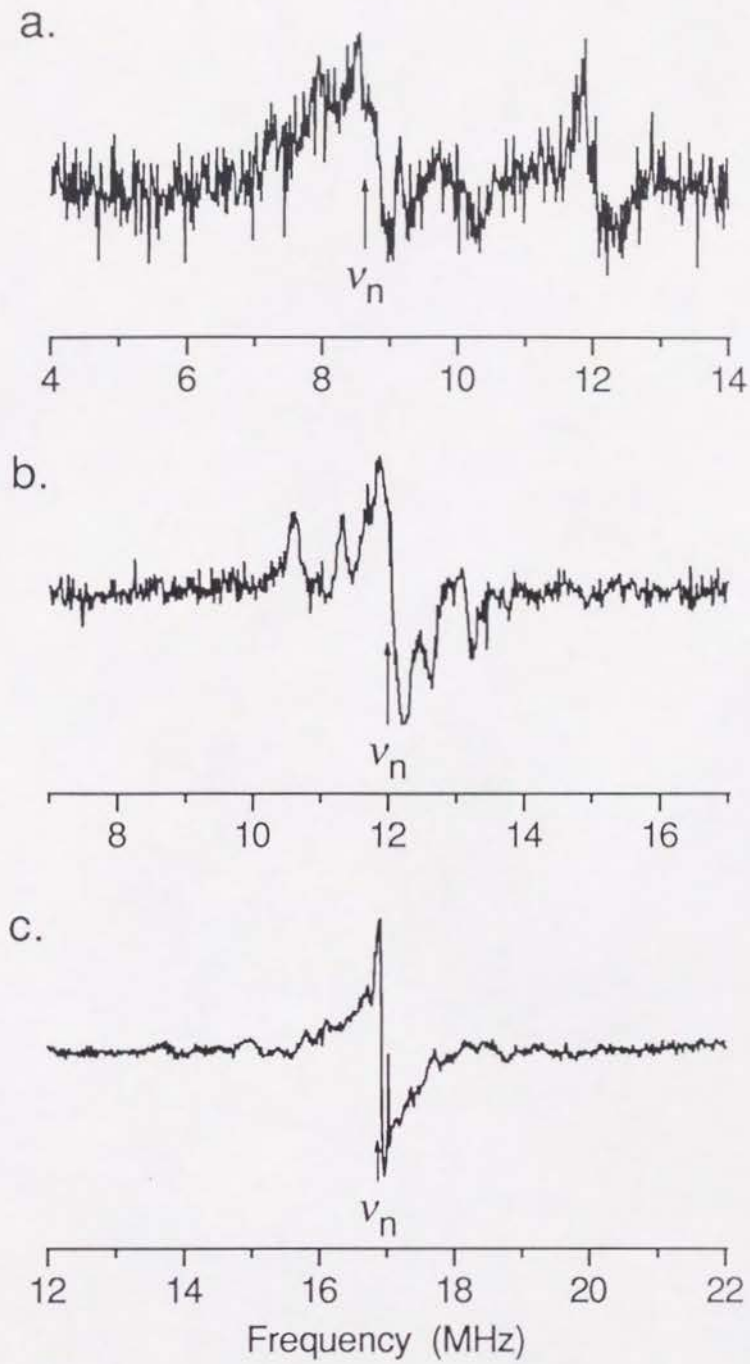

Figure 1.13 ^{1}H-ENDOR spectra of *m*-PBPM$^{+\bullet}$ in glassy solid of BuCl. The measurements were performed at 3.0 K. The magnetic field employed and the number of scans are as follows: **a.** 202.5 mT (*Y*-axis canonical peak of the transition from m_S = -3/2 to -1/2 sublevels) with 530 scans. **b.** 281.4 mT (*X* and *Y*-axis canonical peaks of the transition from m_S = -1/2 to 1/2 sublevels) with 337 scans. **c.** 396.1 mT (extra-line of the transition from m_S = -1/2 to 1/2 sublevels) with 340 scans.

5. ESR spectrum of the ^{13}C isotopomer. If the hole of the cation resides on the singly-occupied π-orbital, the spin density of the two n-orbitals must be essentially the same as that in *m*-PBPM and the isotropic hfcc's of the two divalent carbon atoms are approximately equal. In order to ensure the assignment of the π-cation, we examined a ^{13}C-labeled isotopomer in which one of the two divalent carbon atoms is substituted by ^{13}C. Figure 14 compares the low-field *Y* and *X*-axis canonical peaks of the ^{13}C isotopomer with those of the ^{12}C isotopomer. Each peak of the ^{13}C isotopomer is broadened by the unresolved hyperfine splitting due to ^{13}C. The broad bell-shaped peak of the ^{13}C isotopomer indicates that the hfcc's of the two ^{13}C atoms are approximately equal (see Figure 1.6b and the corresponding discussion on the anion). If the hole occupied the n-orbital, the spin density of one of the two n-orbitals should vanish and the hfcc of that carbon atom must be very small whereas the other carbon atom has essentially the same hfcc as that of the neutral *m*-PBPM, 35 mT [Teki *et al.* to be published.], except for the difference of the spin projection factor 1/2*S*. The superposition of the two components never reproduces the unresolved bell-shaped peak (see Figure 1.6b). Thus, the ESR spectrum of ^{13}C isotopomer indicates that the hole of the cation is in the π-orbital, which is consistent with the result of ^{1}H-ENDOR measurements described above.

We attempted to observe the ^{13}C ENDOR spectrum to determine the hfcc of ^{13}C. However, we failed to detect the signal because of low signal to noise ratio.

6. Conformation of *m*-PBPM$^{+\bullet}$. The fine structure tensor of aromatic polycarbenes can be represented approximately as a superposition of the one center spin-spin interaction of n-π type at each divalent carbon atom [Higuchi (1963a, b)]. Therefore, the fine structure tensor is determined mainly by the relative orientation of the one-center interaction tensors and the spin density at the divalent carbon atoms. Since the fine structure parameters and the electronic structure of the cation are now determined, we can estimate the conformation of the cation by considering the relative orientation of the one-center interaction tensors: Since the one-center interaction tensor can be approximated by the fine structure tensor of diphenylmethylene (DPM), the semi-quantitative expression for the fine structure tensor is given by eq. (1.9) [Teki *et al.* (1986)].

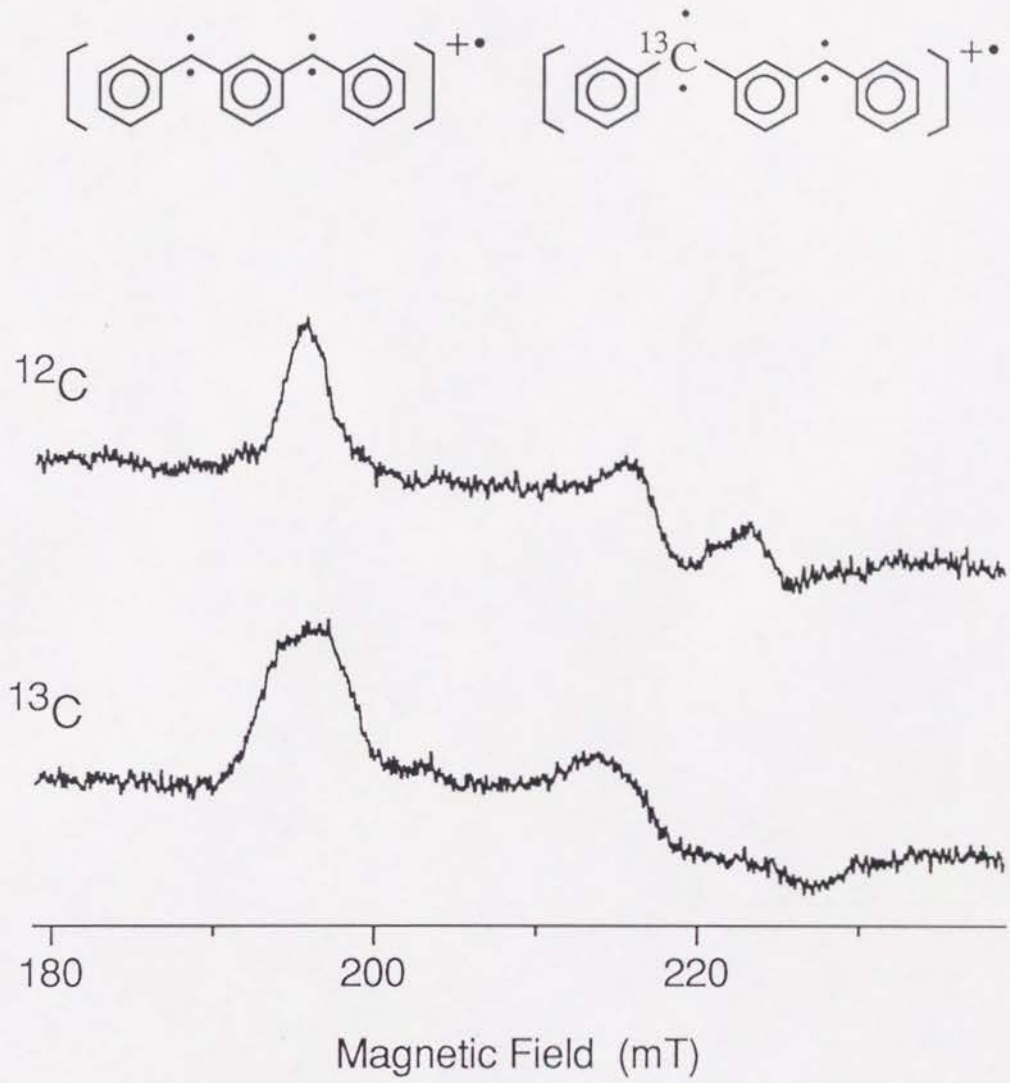

Figure 1.14 The ESR spectrum of ^{13}C substituted *m*-PBPM$^{+\bullet}$ in which one of the two divalent carbon atoms was substituted by ^{13}C. The spectrum of ^{12}C isotopomer is also shown for comparison.

$$D_{ij} = [S(2S-1)]^{-1} \sum_k (\rho_k/\rho_{\mathrm{DPM}}) \left(\mathbf{U}_k \cdot \mathbf{D}_{\mathrm{DPM}} \cdot \mathbf{U}_k^{-1}\right)_{ij}$$

$$i, j = X, Y, Z \qquad (1.9)$$

where the subscript k runs over all the divalent carbon atoms and $\mathbf{D}_{\mathrm{DPM}}$ denotes the fine structure tensor of DPM. The symbols ρ_k and ρ_{DPM} represent the spin density of the π-electron at the kth divalent carbon atom and that at the divalent carbon atom of DPM,respectively. The orthogonal matrix $\mathbf{U}_k$ transforms the principal axes of the tensor $\mathbf{D}_{\mathrm{DPM}}$ at the kth divalent carbon atom to the molecule fixed axes. Since a simple LCAO-MO calculation gives the spin densities of $\rho_{\mathrm{DPM}} = 2/5$ and $\rho_{m\text{-PBPM}} = 0.4040$, the ratio $\rho_{m\text{-PBPM}}/\rho_{\mathrm{DPM}}$ can be regarded as unity. Table 1.1 compares the fine structure parameters of the monoions with those of DPM and *m*-PBPM. If the conformation of the cation was the same as that of the neutral *m*-PBPM which is known to be a cis-trans type as shown in Conformation A [Itoh (1978)], the fine structure tensor of the cation would be approximately equal to that of *m*-PBPM, because in the π-cation the π-electron density would be halved but the projection factor $[S(2S-1)]^{-1}$ should be doubled against the quintet *m*-PBPM (the factor is 1/6 for the quartet and 1/12 for the quintet). On the other hand, when the conformation of the cation is of a trans-trans type where the two one-center interaction tensors are roughly parallel, the fine structure parameters are estimated as 1/3 of those of DPM, because the sum in eq. (6) $\sum_k (\rho_k/\rho_{\mathrm{DPM}}) \left(\mathbf{U}_k \cdot \mathbf{D}_{\mathrm{DPM}} \cdot \mathbf{U}_k^{-1}\right)_{ij}$ would be approximately equal to $\mathbf{D}_{\mathrm{DPM}}$ and the projection factor $[S(2S-1)]^{-1}$ is 1/6 for the quartet and 1/2 for the triplet DPM. The experimentally determined values for both of the two conformers are closer to the latter value of $D_{\mathrm{DPM}}/3 = +0.135$ cm^{-1} and $|E_{\mathrm{DPM}}|/3 =$ 0.0064 cm^{-1} (see Table 1.1). The $|E/D|$ ratio, which is the measure of the deviation from the axial symmetry of the tensor, also supports the latter case; the ratio is 0.030 for conformer I and 0.043 for conformer II and they are close to that of DPM, 0.04735, but far from that of *m*-PBPM, 0.2667. Thus, the conformation of the cation is plausibly in a trans-trans type as indicated by Conformation B.

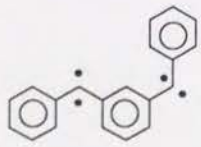

A

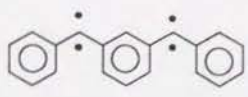

B

Conclusion.

We have detected for the first time negatively and positively charged high-spin molecules and have shown that the ground state of the monoanion and of the monocation of *m*-PBPM are both quartet. A suggestion of the possible reversal of the order of spin states upon charging [Yamaguchi *et al.* (1987)] was not substantiated in both the monoanion and monocation of *m*-PBPM. From the ^{1}H-ENDOR measurements the hole and the excess electron in the cation and the anion are found to reside in the non-bonding π-orbital. The result is compatible with the ESR measurements of the monoions of ^{13}C substituted isotopomer. From the fine structure parameters and the electronic state the conformations of the ions are considered to be in a trans-trans conformation in contrast to the cis-trans conformation of the neutral *m*-PBPM [Itoh (1978)]. The result of the present study should be significant for elucidating the relation between the excess charge and the spin alignment. In order to clarify the difference between electron attachment and removal and to make a more detailed discussion on the electronic structure of charged high-spin systems, experimental and theoretical studies of smaller π-conjugated systems are now in progress.

Chapter 2. ESR Study of a Non-Rigid Jahn-Teller Active Cation: $CH_4^{+\bullet}$

Introduction

The Jahn-Teller distortion [Jahn and Teller (1937)] of CH_4 has been subject to a number of theoretical studies [Coulson and Strauss (1962), Arents and Allen (1970), Dixon (1971), Meyer (1973), Paddon-Row *et al.* (1985), Takeshita (1987), Frey and Davidson (1988), Marinelli and Roche (1990), Reeves and Davidson (1991)]. Experimentally, direct spectroscopic observation of $CH_4^{+\bullet}$ in the gas phase has not been made so far except for the photoelectron spectroscopy [Al-Joboury and Turner (1964, 1967), Brehm and Puttkamer (1967), Baker *et al.* (1968), Pullen *et al.* (1970), Brundle *et al.* (1970)] and a coincidence spectroscopy utilizing the Coulomb-explosion [Vager *et al.* (1986)]. Theoretical studies have been tested by comparison with the line profile of the first photoelectron peak of methane [Rabalais *et al.* (1971), Takeshita (1987), Marinelli and Roche (1990)] and with limited information of ESR [Knight *et al.* (1984), Paddon-Row *et al.* (1985)]. Some time ago Knight *et al.* have detected the radical cation in the neon matrix and reported the isotropic hyperfine coupling constants (hfcc's) of the protons [Knight *et al* (1984)]. In this chapter we will analyze the ESR spectroscopic data in detail on the basis of the dynamic Jahn-Teller distortion of the radical cation.

First, we briefly recapitulate the previous communication by Knight *et al.* in 1984. The spectrum of $CH_2D_2^{+\bullet}$ is an isotropic triplet-quintet with $|A_{iso}(2H)| = 121.7(3)$ G and $|A_{iso}(2D)| = 2.22(6)$ G (see Figure 2.1). The central peaks of the triplet family shift each other slightly due to the second order effect of the two protons of a large hfcc of 121.7 G. As discussed in the previous paper, the spectrum indicates unambiguously that the cation has a C_{2v} symmetry with the electronic state of $^2B_1$ symmetry, the unpaired electron occupying dominantly the $2p_y$ orbital of the carbon atom (the molecule fixed axes are defined in the figure in Table 2.1). The C_{2v} structure with a $^2B_1$ electronic state is also favored by theoretical calculations [Knight *et al.* (1984), Paddon-Row *et al.* (1985), Frey and Davidson (1988)]. In particular, it was shown that among the three possible $CH_2D_2^{+\bullet}$ conformers of C_{2v} symmetry the one having two shorter C-D bonds in the nodal plane of the $2p_y$ orbital has the lowest vibrational zero-point energy [Paddon-Row *et al.* (1985), Frey and Davidson (1988)]. The calculated hfcc's, $|A_{iso}(2H)| = 137$ G and $|A_{iso}(2D)| = -2.6$ G, are in a good agreement with the experimental values [Knight *et al.* (1984)]. As for $CH_4^{+\bullet}$ an isotropic quintet with $|A_{iso}| = 54.8(2)$ G was recorded at 4 K which is

close to the weighted average of the hfcc's of $CH_2D_2^{+\bullet}$ ($[2 \times 121.7 - 2 \times 14.6]/4 = 53.6$ G). This proximity was considered as due to some dynamic averaging of the four hydrogen atoms in $CH_4^{+\bullet}$. However, the question of the averaging mechanism was left open [Knight *et al.* (1984)].

In this chapter we will resolve this unanswered question of $CH_4^{+\bullet}$. All the deuterated radical cations will also be studied both experimentally and analytically. The main part of the chapter will be divided into three sections, i.e., the systems of $CH_2D_2^{+\bullet}$, $CH_4^{+\bullet}$ and $CD_4^{+\bullet}$, and $CH_3D^{+\bullet}$ and $CD_3H^{+\bullet}$. The reason for starting with $CH_2D_2^{+\bullet}$ is twofold; firstly, the previous paper on $CH_2D_2^{+\bullet}$ [Knight *et al.* (1984)] was a short communication without detailed discussions. Secondly, the $CH_2D_2^{+\bullet}$ system provides an easy access to the analysis of the other systems in terms of the permutation-inversion group theory. The third section on the deuterated systems is added for the sake of the integrity of the study on the methane cation.

Experimental

All the experiments were carried out by the group of Professor L. B. Knight, Jr. in South Carolina. The basic design of the formation and trapping of the methane cation in the neon matrix is described elsewhere [Knight *et al.* (1984), Knight (1986)]. In brief, approximately 0.1 % methane in neon gas purchased from Matheson (research grade) is introduced into an open-tube resonance lamp with a continuous neon flow of 3 sccm powered by a microwave generator. The predominant output of this power source occurs at 16.8 eV, which is well above the ionization energy of the methane molecule. The lamp is a 9-mm o.d. quartz tube whose open end is located 5 cm from the deposition target. The target is a round copper rod (1/8" diameter and 1-1/2" long) with the deposition side slightly flattened. The rod is cooled by an Air Products' liquid helium Heli-Tran cryostat. The temperature of the target is maintained at approximately 3 K. After the deposition of photoionized methane and cocondensing neon atoms the target is transferred to the ESR cavity by use of a hydraulic lifter. The ESR spectrometer is a Varian E-109 system with the 102-4 microwave bridge. An Air Products' temperature controller and digital thermocouple readout is used (Model APD-E) with which the temperature of the ESR measurement is covered from approximately 4 to 11 K. Weak ESR background signals due to H_2O^+ [Knight and Steadman (1983)], CH_3, and other foreign species are unavoidably observed. However, these impurity signals can be easily identified to extract the genuine signals due to the methane cation.

Results and discussion

Introductory remark

Since $CH_4^{+\bullet}$ is a non-rigid system with four equivalent hydrogen atoms, the permutation-inversion (PI) group [Longuet-Higgins (1963), Bunker (1979), Dyke (1977)] is to be used for the analysis of ESR spectra. Another fundamental basis for the analysis is the assumption that the wavefunction of the radical cation can be approximated as the product of the rovibronic, the electron spin, and the nuclear spin wavefunctions,

$$\Phi_{total} = \phi_{rve}\,\phi_{es}\,\phi_{ns}. \qquad (2.1)$$

According to the statistics of equivalent particles, the total wavefunction of the molecule must be antisymmetric and symmetric with respect to odd and even permutations of fermions and symmetric for both permutations of bosons. When the irreducible representation of the PI group satisfying this requirement is denoted by $\Gamma(A)$, the restriction of the symmetry of the total wavefunction is expressed as

$$\Gamma_{total} = \Gamma(A), \qquad (2.2)$$

which can be rewritten as

$$\Gamma_{rve} \otimes \Gamma_{es} \otimes \Gamma_{ns} \supset \Gamma(A), \qquad (2.3)$$

Since both the Fermi-Dirac and the Bose-Einstein statistics impose no restriction on the inversion operation, two irreducible species are equally permissible in which the characters of permutation-inversion operations differ (see, e.g., B_1 and B_2 for G_4, A_1 and B_1 for G_8, and A_1 and A_1 for G_{24} in Tables 2.1, 2.3, and 2.5, respectively) [Longuet-Higgins (1963)].

In the static magnetic field it is convenient to take the electron and the nuclear spin projections along the space-fixed axis parallel to the field. Space-fixed spin functions are invariant with respect to the inversion of the spatial coordinates of all particles (electrons and nuclei) in the molecule, so that only the permutation effects of permutation-inversion operations must be considered [Hougen (1976)]. Since the electron spin wavefunctions are not affected by nuclear permutations, the space-fixed electron spin functions are totally symmetric. Thus, the space-fixed nuclear spin functions must be subject to the restriction,

$$\Gamma_{rve} \otimes \Gamma_{ns} \supset \Gamma(A), \qquad (2.4)$$

In the following analysis we assume that there is no accidental degeneracy in rovibronic states and the separation between each rovibronic state is much larger than the Zeeman splitting. Then, the hyperfine interaction between the different rovibronic states can be neglected and the hyperfine Hamiltonian matrix can be set up for each rovibronic state. Thus, the observed ESR spectrum should be expressed as a superposition of the ESR spectrum originating from each rovibronic state with the weight of the Boltzmann factor. Furthermore, we neglect the anisotropic component of the hyperfine tensor because the observed spectra appear almost isotropic.

The symmetrized representation of the nuclear spin function and the hyperfine Hamiltonian are compiled in Tables 2.2, 2.4, 2.6, and 2.10. For a given symmetry Γ and a given nuclear spin quantum number J the relative phase of nuclear spin functions among M sublevels has been chosen so that the operation of the totally symmetric ladder operator $I_{\pm}$ on an M sublevel leads to $M \pm 1$ sublevels with positive coefficients. Similar Tables for the nuclear spin function are given in literatures [Hougen (1976), McConnell *et al.* (1955)].

$CH_2D_2^{+\bullet}$

We first reanalyze the ESR spectrum of $CH_2D_2^{+\bullet}$ reported earlier [Knight *et al.* (1984)] (see Figure 2.1). Since the spectrum reveals clearly the second order shift in the central region of spectrum, the analysis should be made in terms of the symmetrized nuclear spin functions. The use of the symmetrized functions makes also the evaluation of the rotational energy from the ESR intensity much more lucid [McConnell (1958)].

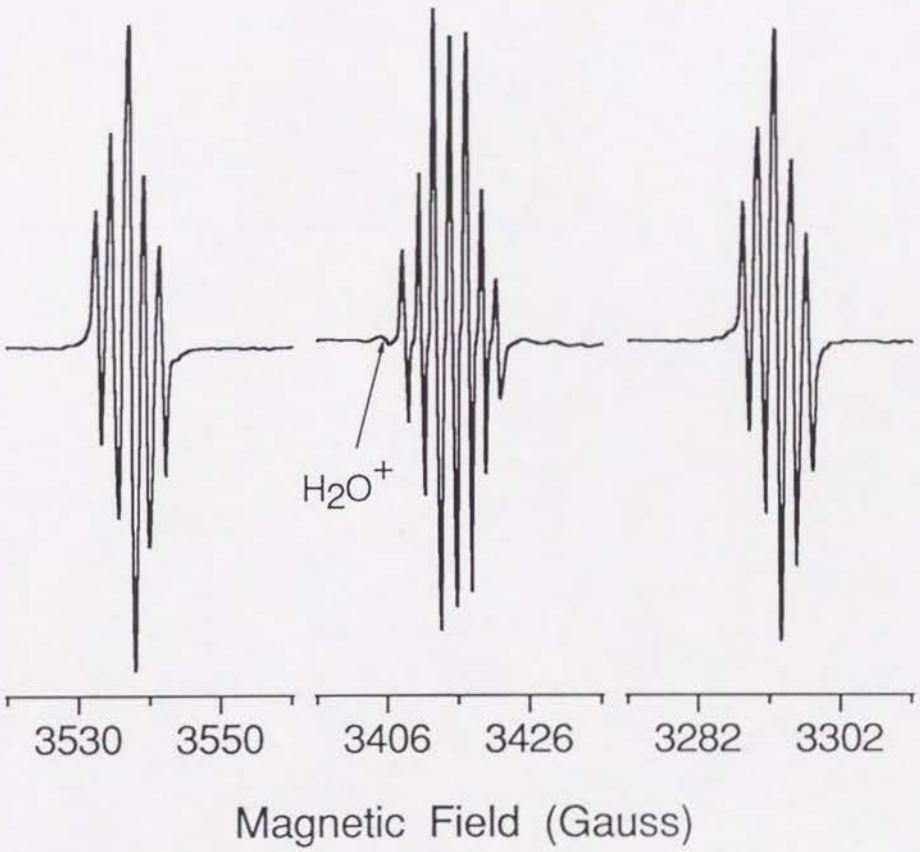

Figure 2.1 ESR spectrum of $CH_2D_2^{+\bullet}$ isolated in neon matrix at 4 K. The vertical expansion is 4 times greater for the wing quintets relative to the central region. The lowest field component of the background impurity species, $H_2O^{+\bullet}$ is indicated. The magnetic field position of g_e occurs at 3421.2 G.

Having two H and two D atoms $CH_2D_2^{+\bullet}$ belongs to the complete nuclear permutation-inversion (CNPI) group G_8 ($= S_2 \times S_2 \times \mathcal{E}^*$) where S_n denotes the nuclear permutation group of degree n and $\mathcal{E}^*$ represents the inversion group. However, out of the total eight elements only four are "feasible" in the sense of Longuet-Higgins for the rigid cation having the C_{2v} symmetry [Longuet-Higgins (1963), Bunker (1979)]. Therefore, we can analyze $CH_2D_2^{+\bullet}$ by the molecular symmetry group G_4 which is a subgroup of the CNPI group and is isomorphous to the point group C_{2v} [Hougen (1962,1963)]. The characters are given in Table 2.1. According to the Fermi-Dirac and the Bose-Einstein statistics, the allowed irreducible representations of the total wave function of $CH_2D_2^{+\bullet}$ are either B_1 or B_2 (see the character for the operation of (12)(34) in Table 2.1).

$$\Gamma_{\text{total}} = B_1 \text{ or } B_2 \quad \text{for } CH_2D_2^{+\bullet} (G_4), \tag{2.5}$$

that is to say,

$$\Gamma_{\text{elec}} \otimes \Gamma_{\text{vib}} \otimes \Gamma_{\text{rot}} \otimes \Gamma_{\text{ns}} \supset B_1 \text{ or } B_2. \tag{2.6}$$

where the rovibronic part is separated into the electronic, vibrational, and rotational wavefunctions by the Born-Oppenheimer approximation. Since the electronic and the vibrational parts are, respectively, of $^2B_1$ and of A_1 symmetry at low temperatures below $\approx$10 K [Knight *et al.* (1984)], we have,

$$\Gamma_{\text{rot}} \otimes \Gamma_{\text{ns}} \supset A_1 \text{ or } A_2. \tag{2.7}$$

The nuclear spin functions to be designated by $|\Gamma; J_H, M_H; J_D, M_D\rangle$ are given as the product of the symmetrized spin functions for the two protons and the two deuterons given in Table 2.2. Therefore, Γ_{ns} can be A_1, A_2, B_1, and B_2 so that the restriction of eq. (2.7) requires that the the rotational states of A_1 or A_2 symmetry be associated with the nuclear spin functions of symmetries of A_1 and A_2 (Case 1 below) and that the rotational states of B_1 or B_2 symmetry with the spin functions of symmetries of B_1 and B_2 (Case 2).

	Γ_{rot}	Γ_{ns}
Case 1	A_1 or A_2	A_1 and A_2
Case 2	B_1 or B_2	B_1 and B_2

(2.8)

Table 2.1 Character table of G_4 used for rigid $CH_2D_2^{+\bullet}$ [Bunker (1979)].

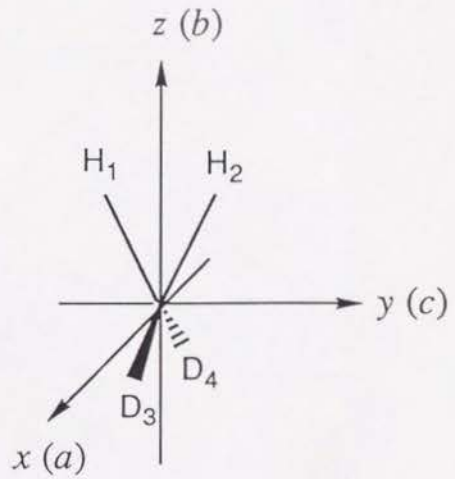

G_4	E	(12)(34)	(12)*	(34)*		
C_{2v}	E	C_{2b}	σ_{ab}	σ_{bc}		
Equiv. rot.	R^0	$R_b\pi$	$R_c\pi$	$R_a\pi$		K_aK_c
A_1	1	1	1	1		ee
A_2	1	1	−1	−1	J_b	oo
B_1	1	−1	−1	1	J_a	eo
B_2	1	−1	1	−1	J_c	oe

Table 2.2 Symmetrized operators and nuclear spin functions used for $CH_2D_2^{+\bullet}$ of G_4 symmetry.

Symmetrization of the set of operators $\{X_1, X_2\}$ and $\{X_3, X_4\}$[a].

$$X^{A_1} = X_1 + X_2$$
$$X^{B_1} = X_1 - X_2$$
$$X^{A_1} = X_3 + X_4$$
$$X^{B_2} = X_3 - X_4$$

Symmetrized representations of the hyperfine Hamiltonian[b].

$$\mathcal{H}_{hfc} = \mathcal{H}_{hfc}(H) + \mathcal{H}_{hfc}(D)$$
$$= \frac{1}{2}\mathbf{S}\cdot\left\{\mathbf{T}(H)^{A_1}\cdot\mathbf{I}(H)^{A_1} + \mathbf{T}(H)^{B_1}\cdot\mathbf{I}(H)^{B_1}\right\} + \frac{1}{2}\mathbf{S}\cdot\left\{\mathbf{T}(D)^{A_1}\cdot\mathbf{I}(D)^{A_1} + \mathbf{T}(D)^{B_2}\cdot\mathbf{I}(D)^{B_2}\right\}$$

Symmetrized nuclear spin functions with the notation of $|\text{nucleus}; \Gamma, J, M_J\rangle$.

$$|\mathrm{H}; A_1; 1, 1\rangle = |\alpha\alpha\rangle$$
$$|\mathrm{H}; A_1; 1, 0\rangle = \frac{1}{\sqrt{2}}(|\alpha\beta\rangle + |\beta\alpha\rangle)$$
$$|\mathrm{H}; A_1; 1, -1\rangle = |\beta\beta\rangle$$
$$|\mathrm{H}; B_1; 0, 0\rangle = \frac{1}{\sqrt{2}}(|\alpha\beta\rangle - |\beta\alpha\rangle)$$

$$|\mathrm{D}; A_1; 2, 2\rangle = |1\ 1\rangle$$
$$|\mathrm{D}; A_1; 2, 1\rangle = \frac{1}{\sqrt{2}}(|0\ 1\rangle + |1\ 0\rangle)$$
$$|\mathrm{D}; A_1; 2, 0\rangle = \frac{1}{\sqrt{6}}(|1\ -1\rangle + |-1\ 1\rangle + 2|0\ 0\rangle)$$
$$|\mathrm{D}; A_1; 2, -1\rangle = \frac{1}{\sqrt{2}}(|0\ -1\rangle + |-1\ 0\rangle)$$
$$|\mathrm{D}; A_1; 2, -2\rangle = |-1\ -1\rangle$$
$$|\mathrm{D}; A_1; 0, 0\rangle = \frac{1}{\sqrt{6}}(|1\ -1\rangle + |-1\ 1\rangle - 2|0\ 0\rangle)$$
$$|\mathrm{D}; B_2; 1, 1\rangle = \frac{1}{\sqrt{2}}(-|0\ 1\rangle + |1\ 0\rangle)$$
$$|\mathrm{D}; B_2; 1, 0\rangle = \frac{1}{\sqrt{2}}(|1\ -1\rangle - |-1\ 1\rangle)$$
$$|\mathrm{D}; B_2; 1, -1\rangle = \frac{1}{\sqrt{2}}(|0\ -1\rangle - |-1\ 0\rangle)$$

[a] X_i is the hyperfine interaction operator $\mathbf{T}_i$ or the nuclear spin operator $\mathbf{I}_i$.

[b] The anisotropy of $\mathbf{T}$ tensor is neglected in the present analysis and only the Fermi term T_f is considered.

Since we assume that the separation of rotational states are much larger than the Zeeman splitting, the hyperfine interaction between different rotational states is neglected. Thus, the hyperfine Hamiltonian is blocked out for each rotational state. In order to evaluate the hyperfine coupling energy of a non-degenerate rovibronic state, it is convenient to compute the expectation value of the Fermi interaction operator T_f in the hyperfine Hamiltonian in Table 2.2 with regard to the non-degenerate rovibronic coordinate. Then, we have the spin Hamiltonian consisting only of totally symmetric operators as follows,

$$\mathcal{H}_{spin} = \mathcal{H}_{spin}(H) + \mathcal{H}_{spin}(D) = \frac{1}{2} A(H)^{A_1}\, \mathbf{S}\cdot\mathbf{I}(H)^{A_1} + \frac{1}{2} A(D)^{A_1}\, \mathbf{S}\cdot\mathbf{I}(D)^{A_1} \tag{2.9}$$

where the non-zero isotropic hyperfine coupling constants are

$$\begin{aligned} A(H)^{A_1} &= \langle \mathrm{rve};\, \Gamma_{\mathrm{rve}} \,|\, T_f(H)^{A_1} \,|\, \mathrm{rve};\, \Gamma_{\mathrm{rve}} \rangle \\ A(D)^{A_1} &= \langle \mathrm{rve};\, \Gamma_{\mathrm{rve}} \,|\, T_f(D)^{A_1} \,|\, \mathrm{rve};\, \Gamma_{\mathrm{rve}} \rangle \end{aligned} \tag{2.10}$$

The Hamiltonian matrix is diagonal with respect to the quantum numbers J for H and D because the spin Hamiltonian commutes with $J(H)^2$ and $J(D)^2$. Then, we only have to evaluate the spin Hamiltonian matrix element for each $J(H)$ and $J(D)$ block using the symmetrized nuclear spin functions given in Table 2.2. The matrix elements of the first term in eq. (2.9) is represented as follows (the quantum numbers for D are omitted for brevity).

$$\langle \alpha; J_H, M_H \,|\, \mathcal{H}_{spin}(H) \,|\, \alpha; J_H, M_H \rangle = +\frac{1}{2} M_H\, A_{iso}(H) \tag{2.11a}$$

$$\langle \beta; J_H, M_H \,|\, \mathcal{H}_{spin}(H) \,|\, \beta; J_H, M_H \rangle = -\frac{1}{2} M_H\, A_{iso}(H) \tag{2.11b}$$

$$\langle \alpha; J_H, M_H \,|\, \mathcal{H}_{spin}(H) \,|\, \beta; J_H, M_H + 1 \rangle = \sqrt{J_H(J_H+1) - M_H(M_H+1)}\; A_{iso}(H) \tag{2.11c}$$

$$\langle \beta; J_H, M_H \,|\, \mathcal{H}_{spin}(H) \,|\, \alpha; J_H, M_H - 1 \rangle = \sqrt{J_H(J_H+1) - M_H(M_H-1)}\; A_{iso}(H) \tag{2.11d}$$

where α and β represent the electron spin function, and $A_{iso}(H)$ is given as below.

$$A_{iso}(H) = \frac{1}{2} A(H)^{A_1} \tag{2.12}$$

The non-zero matrix elements of the second term of eq. (2.9) are obtained by replacing the symbol H in eqs. (2.11) and (2.12) with D.

Eqs. (2.13) are reproduced from Table 2.2 which will be used in the calculations of both Cases 1 and 2 below.

$$|A_1; J_H{=}1, M_H; J_D{=}2, M_D\rangle = |A_1; J_H{=}1, M_H\rangle\ |A_1; J_D{=}2, M_D\rangle \quad (2.13a)$$

$$|A_1; J_H{=}1, M_H; J_D{=}0, M_D\rangle = |A_1; J_H{=}1, M_H\rangle\ |A_1; J_D{=}0, M_D\rangle \quad (2.13b)$$

$$|A_2; J_H{=}0, M_H; J_D{=}1, M_D\rangle = |B_1; J_H{=}0, M_H\rangle\ |B_2; J_D{=}1, M_D\rangle \quad (2.13c)$$

$$|B_1; J_H{=}0, M_H; J_D{=}2, M_D\rangle = |B_1; J_H{=}0, M_H\rangle\ |A_1; J_D{=}2, M_D\rangle \quad (2.13d)$$

$$|B_1; J_H{=}0, M_H; J_D{=}0, M_D\rangle = |B_1; J_H{=}0, M_H\rangle\ |A_1; J_D{=}0, M_D\rangle \quad (2.13e)$$

$$|B_2; J_H{=}1, M_H; J_D{=}1, M_D\rangle = |A_1; J_H{=}1, M_H\rangle\ |B_2; J_D{=}1, M_D\rangle \quad (2.13f)$$

Case 1 ($\Gamma_{rot} = A_1$ or A_2);

In this case the nuclear spin functions can be of A_1 and A_2 symmetries. The spin Hamiltonian has three blocks which are expanded in terms of the functions of (2.13a), (2.13b) and (2.13c). Once the spin Hamiltonian matrix is blocked out, it is straightforward to obtain the resonant fields for the ESR transition correct to the second order approximation which are given in eqs. (2.14) – (2.16). Since the hfcc of the D atoms is two orders of magnitude smaller than that of the H atoms, the second order effect of the D atoms has been ignored in the analysis of spectrum in Figure 2.1. The three-armed fork at the top of Figure 2.2 indicates the resonance fields corresponding to the set of $J_H = 1$, $M_H = -1, 0, 1$ correct to the second order approximation. The upper two stick spectra in Figure 2.2 with the notation of A_1 correspond to eqs. (2.14) and (2.15) and the next one with A_2 to eq. (2.16). It happens to be that the resonance field corresponding to $J_H = 1$, $M_H = 0$, $J_D = 2$, $M_D = -2$ is approximately the same as the field corresponding to $J_H = 0$, $M_H = 0$ (which is shown by the single stick spectrum with the notation of B_1 to be discussed in connection with eq. (2.18) below). The sum of the stick spectra of A_1 and A_2 is also shown for Case 1.

Nuclear spin states of A_1 with $J_H = 1$ and $J_D = 2$:

$$H = H_0 - A_{iso}(H)\, M_H - \frac{1}{2H_0} A_{iso}(H)^2 \left[J_H(J_H+1) - M_H{}^2\right] - A_{iso}(D)\, M_D$$

$$\text{with } M_H = -1,\ 0,\ 1, \text{ and } M_D = -2, -1,\ 0,\ 1,\ 2 \quad (2.14)$$

Nuclear spin states of A_1 with $J_H = 1$ and $J_D = 0$:

$$H = H_0 - A_{iso}(H)\, M_H - \frac{1}{2H_0} A_{iso}(H)^2 \left[J_H (J_H + 1) - M_H{}^2 \right]$$

$$\text{with } M_H = -1,\ 0,\ 1 \qquad (2.15)$$

Nuclear spin states of A_2 with $J_H = 0$ and $J_D = 1$:

$$H = H_0 - A_{iso}(D)\, M_D \qquad \text{with } M_D = -1,\ 0,\ 1 \qquad (2.16)$$

Case 2 ($\Gamma_{rot} = B_1$ or B_2);

In this case the spin Hamiltonian is blocked into three parts corresponding to eqs. (2.13d) – (2.13f). The resonant fields for the ESR transitions are given by eqs. (2.17) – (2.19). The lower half of Figure 2.2 demonstrates the spectral components and the sum as in the upper half.

Nuclear spin states of B_1 with $J_H = 0$ and $J_D = 2$:

$$H = H_0 - A_{iso}(D)\, M_D \qquad \text{with } M_D = -2,\ -1,\ 0,\ 1,\ 2 \qquad (2.17)$$

Nuclear spin states of B_1 with $J_H = 0$ and $J_D = 0$:

$$H = H_0 \qquad (2.18)$$

Nuclear spin states of B_2 with $J_H = 1$ and $J_D = 1$:

$$H = H_0 - A_{iso}(H)\, M_H - \frac{1}{2H_0} A_{iso}(H)^2 \left[J_H (J_H + 1) - M_H{}^2 \right] - A_{iso}(D)\, M_D$$

$$\text{with } M_H = -1,\ 0,\ 1, \text{ and } M_D = -1,\ 0,\ 1 \qquad (2.19)$$

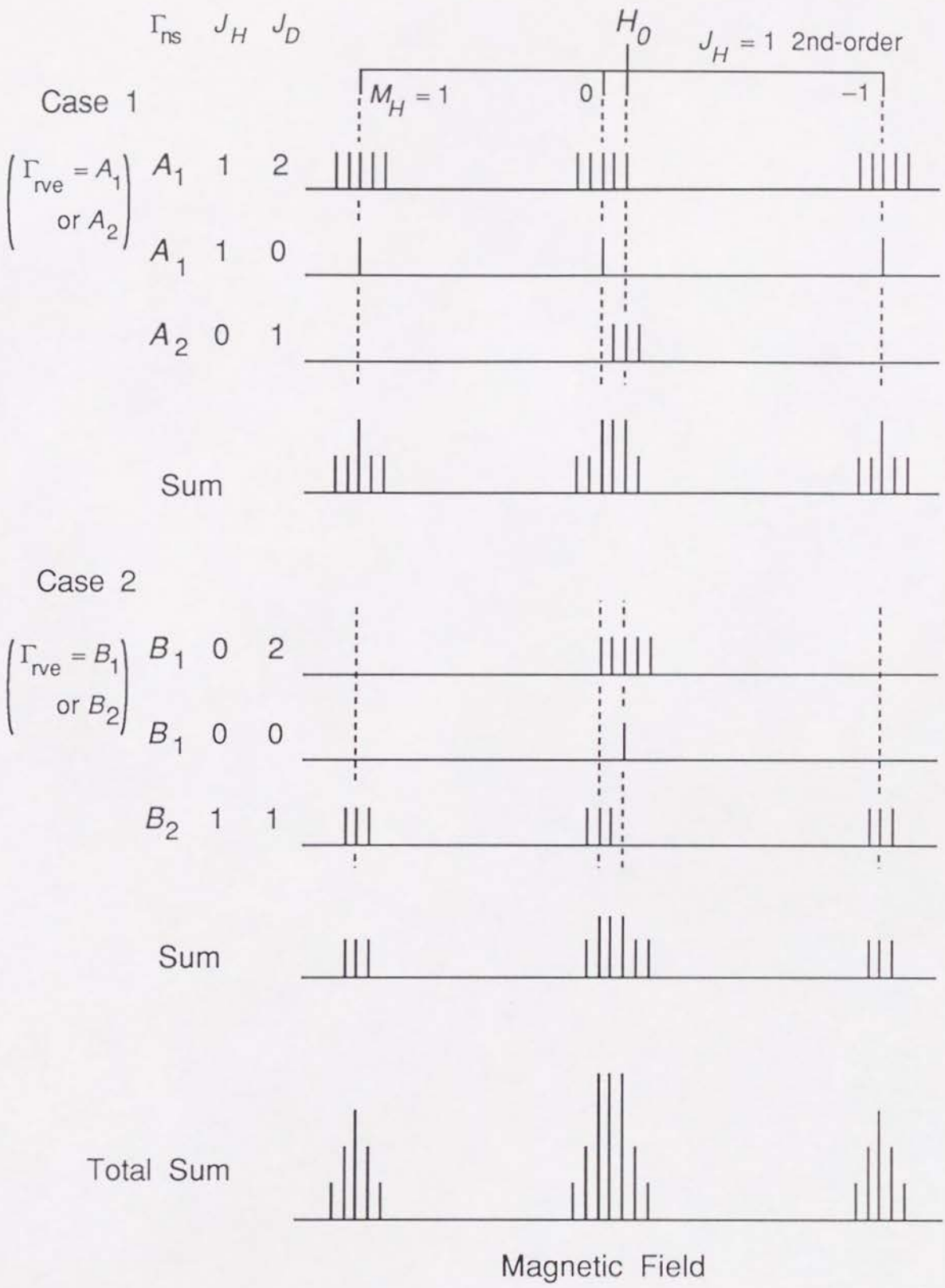

Figure 2.2 ESR spectral pattern of $CH_2D_2^{+\bullet}$.

Due to the symmetry restriction of eq. (2.7) the rotational ground state of the A_1 symmetry must be associated with the nuclear spin states of A_1 and A_2. Likewise, the first rotationally excited state of B_1 must be combined with the nuclear spin states of B_1 and B_2 and so on. In order to estimate the energy of the rotational states we refer to the rotational constants of $CH_2D_2^{+\bullet}$ calculated for an optimized geometry [Takeshita (1987)], which are A = 128 GHz, B = 114 GHz, and C = 72 GHz. The correspondence of the *abc* and *xyz* axis systems is $abc \equiv xzy$ (see Table 2.1). Thus, if the rotation of $CH_2D_2^{+\bullet}$ were completely free as in the gas phase, the rotational energy levels should be nearly of the oblate type and the three lowest excited rotational states of symmetries of B_1, A_2, and B_2 are estimated at about 180, 190, and 250 GHz above the ground state. The symmetry species of the rotational angular momentum J and the symmetry of the rotational states labelled by K_a and K_c are shown in Table 2.1. Since the observed ESR spectrum is the superposition of spectra associated with each rotational state, the Boltzmann distribution at 4 K must be taken into account, the result of which turned out to be that the gross population summing up both B_1 and B_2 rotational states (Case 2) amounts only to ca.15 % of that of A_1 and A_2 states. Therefore, the Boltzmann-weighted spectrum should be modified so as to reduce the intensity of the transitions involving rotational energy levels of B_1 and B_2, e.g., the transitions corresponding to the highest field manifold among the total seven central peaks belonging to the family of $M_H = 0$ be much weaker than the lowest field manifold. However, the spectrum of $CH_2D_2^{+\bullet}$ [Knight *et al.* (1984)] shows that the highest field manifold of the central peaks is only slightly weaker than the lowest giving the approximate intensity distribution of 1:2:4:4:4:2:1 which is just equal to the intensity ratio obtained by the simple sum of the ESR spectral patterns of the rotational levels with an equal weight (compare Figure 2.1 with the bottom of Figure 2.2). This fact implies that the population difference between the ground and the first rotationally excited states is not such that as predicted by the rotational constants calculated for the ion in the free space but that the rotational energy levels corresponding to Cases 1 and 2 are almost equally populated in the solid matrix. Therefore, it should be interpreted that the effective rotational constants in the matrix are much larger than those in the free space. Since the observed ESR spectrum does not show any significant anisotropy of the g- and the hfc tensors at 4 K [Knight, *et al.* (1984)], however, we conjecture that $CH_2D_2^{+\bullet}$ is rotating to annihilate the anisotropy in the ESR time scale but the influence of the crystalline field prevents depiction of the rotation as completely free as in the gas phase. On the other hand, the present result indicates that the wavefunction of the cation in the matrix can be meaningfully labelled by the irreducible species of group G_4. In this context we cite relevant references dealing with the rotation of methane in rare gas matrices as studied by infrared absorption spectroscopy [Cabana *et al.* (1963), Frayer and Ewing (1968), Jones *et al.* (1986)] and by theoretical analyses [King and Hornig (1966), Nishiyama and Yamamoto (1973), Miller and Decius (1973)]. As for

methane isolated in the neon matrix the possibility of a highly hindered rotation has been suggested [Jones *et al.* (1986)].

In conclusion, the observed spectrum of $CH_2D_2^{+\bullet}$ [Knight *et al* (1984)] is now understood in detail. The above argument in terms of the molecular symmetry group G_4 is not necessary in so far as $CH_2D_2^{+\bullet}$ is distorted permanently to C_{2v}. However, as mentioned in the beginning our main subject is the non-rigid $CH_4^{+\bullet}$ and the above treatment of $CH_2D_2^{+\bullet}$ in terms of the molecular symmetry group can be immediately extended for the analysis of the main subject.

$CH_4^{+\bullet}$

Although not mentioned in our previous paper [Knight *et al* (1984)], the spectrum of $CH_4^{+\bullet}$ at temperatures between 4 – 11 K exhibits weak but definite lines in addition to the major quintet lines reported as shown in Figure 2.3. The weak lines change continuously and reversibly up to about 11 K at which the matrix softens. In this section we will analyze these lines and will conclude that the origin of the additional lines is due to the removal of the degeneracy of the rovibronic wavefunction on account of the nuclear hyperfine interaction.

The primary feature of the spectra in Figure 2.3 is the quintet due to the four equivalent protons which are indicated by $M_J = 2, 1, 0, -1, -2$. Besides the quintet the unwanted methyl radical denoted by Me appears throughout the whole temperature region. The signal due to the water cation is also seen at about 4 K but it disappears rapidly with the temperature (in fact, this reversible water signal may be called the most sensitive "thermometer" in this temperature region [Knight *et al.* (1983)]). Hereafter, we will ignore these two foreign signals. Then, the essential spectral features intrinsic to $CH_4^{+\bullet}$ can be summarized as;

(i) the quintet appears at all the temperatures tested, and the change in the line width with temperature is rather small although sharpening at higher temperatures is slightly noticeable.

(ii) "extra" lines appear at 3335 – 3350 G and at 3425 – 3440 G between the $M_J = \pm 1$ of $CH_4^{+\bullet}$ and the methyl lines. They are very broad at 4.2 and 6.4 K but start to reveal a doublet feature at 7.4 K up to the highest temperature measured. The separation between the doublet becomes smaller with temperature and at 11.1 K it merges almost into a singlet. The behavior of these "extra" signals is completely reversible with respect to the temperature.

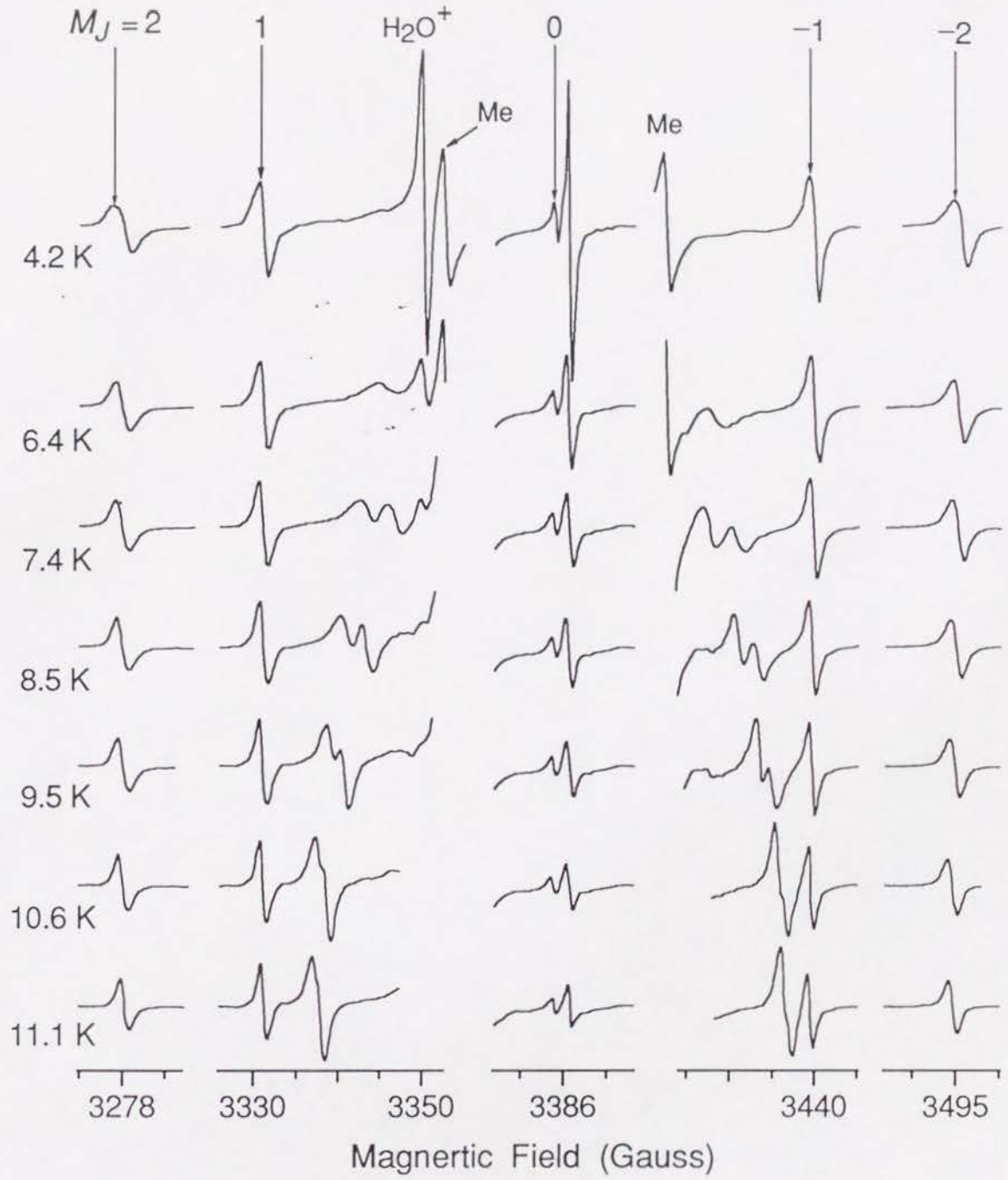

Figure 2.3 ESR spectra of $CH_4^{+\bullet}$ isolated in neon matrix at 4.2 – 11.1 K. The vertical scale of the central region is reduced to 1/6.3 relative to the other parts. The signals due to the methyl radical are indicated by the symbol Me. The background signal due to $H_2O^{+\bullet}$ disappears with the temperature.

In the rest of this subsection we will focus on the above spectral features. We first investigate the effect of the Jahn-Teller distortion from T_d to C_{2v}, and then the effect of the distortion to other symmetries although the latter will be ruled out eventually.

There are two possible shufflings that make the four hydrogen atoms dynamically equivalent; one is the tunneling between the two C_{2v} structures which are interconverted with a common single C_2 axis as shown in Scheme 2.1; the other is the tunneling involving the six equivalent C_{2v} as shown in Scheme 2.2. We will analyze the two possibilities separately to conclude that the observed spectral change is compatible with the latter shufflings but not with the former.

Scheme 2.1

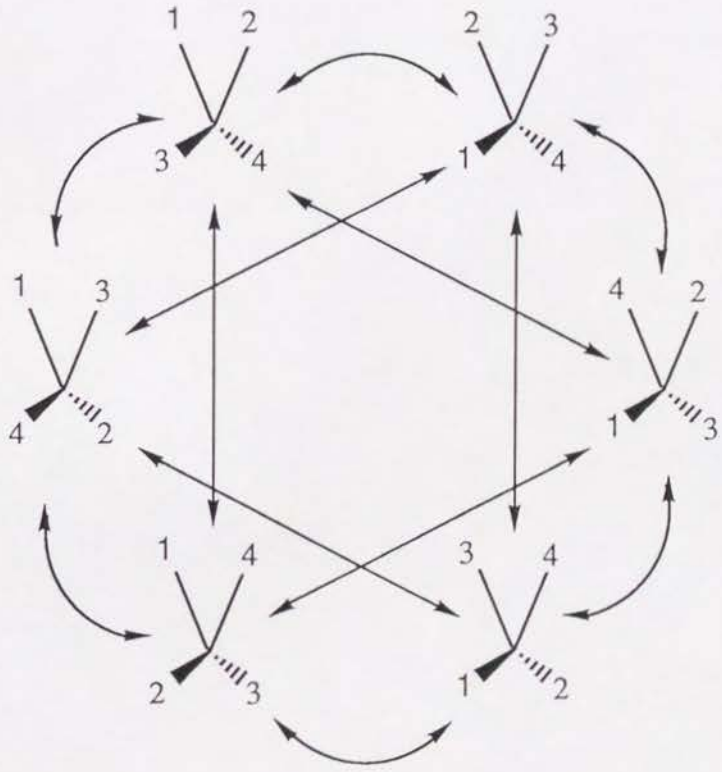

Scheme 2.2

1) Tunneling Between the Two C_{2v} Structures

The molecular symmetry group for the system executing the tunneling in Scheme 2.1 is G_8 which is isomorphous with the point group D_{2d} of the order of 8. From Table 2.3 the nuclear spin statistically allowed symmetry species for the total wavefunction must be A_1 or B_1 because the operations (12)(34) and (14)(23) must have the character of +1. Thus, the direct product of Γ_{rve} and Γ_{ns} must include A_1 or B_1 by eq. (2.4). Since the symmetry species for Γ_{ns} given in Table 2.4 are A_1, B_1, B_2, and E with A_2 being missing, the possible combinations are restricted as in eq. (2.20),

	Γ_{rve}	Γ_{ns}
Case 1	A_1 or B_1	A_1 and B_1
Case 2	A_2 or B_2	B_2
Case 3	E	E

(2.20)

(Note that $E \otimes E = A_1 + B_1 + A_2 + B_2$)

From the correlation diagram between G_4 and G_8 in Scheme 2.3, the A_1 state in the rigid system of G_4 is to split into A_1 and B_2 states by tunneling, and the A_2 state into A_2 and B_1 states. However, the B_1 and B_2 states do not split but become doubly degenerate with the symmetry of E. We assume that there is no accidental degeneracy in the non-rigid system and the separation between the neighboring rovibronic levels is much larger than the electron Zeeman energy so that the hyperfine interaction between the different rovibronic levels can be neglected. Then, the ESR spectrum can be determined from the hyperfine Hamiltonian for each rovibronic state. In the following we will analyze the above three cases.

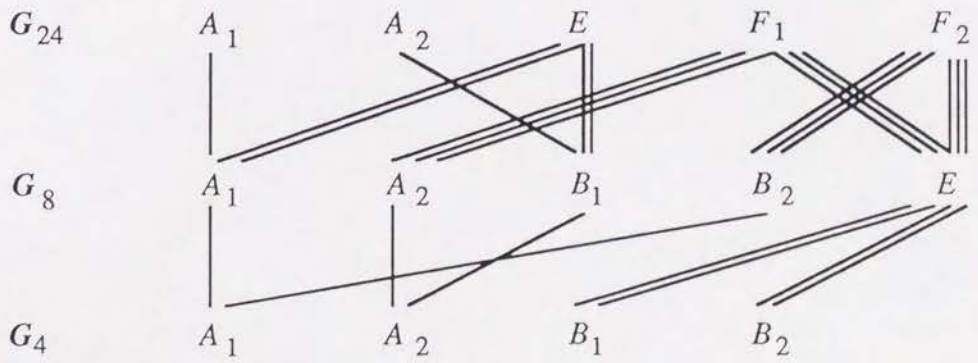

Scheme 2.3 Correlation among symmetry species of G_4, G_8, and G_{24}.

Table 2.3 Character table of G_8 used for the analysis of non-rigid $CH_4^{+\bullet}$.

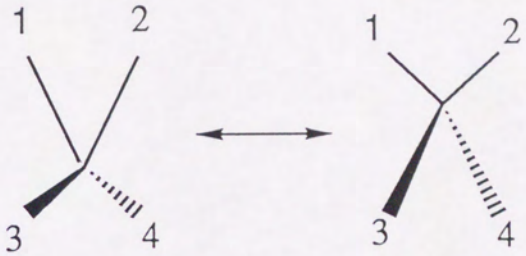

G_8	E	(1324)* (1423)*	(12)(34)	(14)(23) (13)(24)	(12)* (34)*
A_1	1	1	1	1	1
A_2	1	1	1	−1	−1
B_1	1	−1	1	1	−1
B_2	1	−1	1	−1	1
E	2	0	−2	0	0

Table 2.4 Symmetrized operators and nuclear spin functions used for $CH_4^{+\bullet}$ of G_8 symmetry.

Symmetrization of set of operators $\{\mathbf{X}_1, \mathbf{X}_2, \mathbf{X}_3, \mathbf{X}_4\}$[a]

$$\mathbf{X}^{A_1} = \mathbf{X}_1 + \mathbf{X}_2 + \mathbf{X}_3 + \mathbf{X}_4$$
$$\mathbf{X}^{B_2} = \mathbf{X}_1 - \mathbf{X}_2 + \mathbf{X}_3 - \mathbf{X}_4$$
$$\mathbf{X}^{E_x} = \sqrt{2}\,(\mathbf{X}_3 - \mathbf{X}_4)$$
$$\mathbf{X}^{E_y} = \sqrt{2}\,(-\mathbf{X}_1 + \mathbf{X}_2)$$

Symmetrized representation of hyperfine Hamiltonian[b]

$$\mathcal{H}_{hfc} = \frac{1}{4}\,\mathbf{S}\cdot\left(\mathbf{T}^{A_1}\cdot\mathbf{I}^{A_1} + \mathbf{T}^{B_2}\cdot\mathbf{I}^{B_2} + \mathbf{T}^{E_x}\cdot\mathbf{I}^{E_x} + \mathbf{T}^{E_y}\cdot\mathbf{I}^{E_y}\right)$$

Symmetrized nuclear spin functions of the four protons

$$|A_1;2,2\rangle = |\alpha\alpha\alpha\alpha\rangle$$
$$|A_1;2,1\rangle = \frac{1}{\sqrt{4}}\left(|\beta\alpha\alpha\alpha\rangle + |\alpha\beta\alpha\alpha\rangle + |\alpha\alpha\beta\alpha\rangle + |\alpha\alpha\alpha\beta\rangle\right)$$
$$|A_1;2,0\rangle = \frac{1}{\sqrt{6}}\left(|\alpha\beta\alpha\beta\rangle + |\beta\alpha\beta\alpha\rangle + |\beta\alpha\alpha\beta\rangle + |\alpha\beta\beta\alpha\rangle + |\alpha\alpha\beta\beta\rangle + |\beta\beta\alpha\alpha\rangle\right)$$
$$|A_1;2,-1\rangle = \frac{1}{\sqrt{4}}\left(|\alpha\beta\beta\beta\rangle + |\beta\alpha\beta\beta\rangle + |\beta\beta\alpha\beta\rangle + |\beta\beta\beta\alpha\rangle\right)$$
$$|A_1;2,-2\rangle = |\beta\beta\beta\beta\rangle$$

$$|B_2;1,1\rangle = \frac{1}{\sqrt{4}}\left(-|\beta\alpha\alpha\alpha\rangle - |\alpha\beta\alpha\alpha\rangle + |\alpha\alpha\beta\alpha\rangle + |\alpha\alpha\alpha\beta\rangle\right)$$
$$|B_2;1,0\rangle = \frac{1}{\sqrt{2}}\left(|\alpha\alpha\beta\beta\rangle - |\beta\beta\alpha\alpha\rangle\right)$$
$$|B_2;1,-1\rangle = \frac{1}{\sqrt{4}}\left(|\alpha\beta\beta\beta\rangle + |\beta\alpha\beta\beta\rangle - |\beta\beta\alpha\beta\rangle - |\beta\beta\beta\alpha\rangle\right)$$

$$|E_x;1,1\rangle = \frac{1}{\sqrt{2}}\left(-|\alpha\alpha\beta\alpha\rangle + |\alpha\alpha\alpha\beta\rangle\right)$$
$$|E_x;1,0\rangle = \frac{1}{\sqrt{4}}\left(|\alpha\beta\alpha\beta\rangle - |\beta\alpha\beta\alpha\rangle + |\beta\alpha\alpha\beta\rangle - |\alpha\beta\beta\alpha\rangle\right)$$
$$|E_x;1,-1\rangle = \frac{1}{\sqrt{2}}\left(|\beta\beta\alpha\beta\rangle - |\beta\beta\beta\alpha\rangle\right)$$

$$|E_y;1,1\rangle = \frac{1}{\sqrt{2}}\left(|\beta\alpha\alpha\alpha\rangle - |\alpha\beta\alpha\alpha\rangle\right)$$
$$|E_y;1,0\rangle = \frac{1}{\sqrt{4}}\left(-|\alpha\beta\alpha\beta\rangle + |\beta\alpha\beta\alpha\rangle + |\beta\alpha\alpha\beta\rangle - |\alpha\beta\beta\alpha\rangle\right)$$
$$|E_y;1,-1\rangle = \frac{1}{\sqrt{2}}\left(-|\alpha\beta\beta\beta\rangle + |\beta\alpha\beta\beta\rangle\right)$$

$$|A_1;0,0\rangle = \frac{1}{\sqrt{12}}\left(-|\alpha\beta\alpha\beta\rangle - |\beta\alpha\beta\alpha\rangle - |\beta\alpha\alpha\beta\rangle - |\alpha\beta\beta\alpha\rangle + 2|\alpha\alpha\beta\beta\rangle + 2|\beta\beta\alpha\alpha\rangle\right)$$
$$|B_1;0,0\rangle = \frac{1}{\sqrt{4}}\left(|\alpha\beta\alpha\beta\rangle + |\beta\alpha\beta\alpha\rangle - |\beta\alpha\alpha\beta\rangle - |\alpha\beta\beta\alpha\rangle\right)$$

[a] $\mathbf{X}_i$ is the hyperfine interaction operator $\mathbf{T}_i$ or the nuclear spin operator $\mathbf{I}_i$.

[b] The anisotropy of $\mathbf{T}$ tensor is neglected in the present analysis and only the Fermi term T_f is considered.

Case 1 ($\Gamma_{rve} = A_1$ or B_1) and *Case 2 ($\Gamma_{rve} = A_2$ or B_2);*

In both cases the rovibronic levels are non-degenerate so that only the totally symmetric Fermi term has a non-zero expectation value given in eq. (2.21) (see also the symmetrized hyperfine Hamiltonian in Table 2.4).

$$A^{A_1} = \langle \text{rve}; \Gamma_{\text{rve}} | T_f^{A_1} | \text{rve}; \Gamma_{\text{rve}} \rangle \tag{2.21}$$

The isotropic spin Hamiltonian for these non-degenerate rovibronic states becomes,

$$\mathcal{H}_{spin} = \frac{1}{4} A^{A_1} \mathbf{S} \cdot \mathbf{I}^{A_1} \tag{2.22}$$

According to Table 2.4 the spin Hamiltonian matrix consists of the three blocks of A_1 symmetry with $J = 2$, A_1 symmetry with $J = 0$, and B_1 symmetry with $J = 0$ in Case 1, and one block of B_2 symmetry with $J = 1$ in Case 2. The non-zero matrix elements in each block are determined by the operator $\mathbf{S}\cdot\mathbf{I}^{A_1}$ and are exactly the same as those given in eq. (2.11) except for the constant A_{iso}.

$$\langle \alpha; J, M_J | \mathcal{H}_{spin} | \alpha; J, M_J \rangle = + \frac{1}{2} M_J A_{iso} \tag{2.23a}$$

$$\langle \beta; J, M_J | \mathcal{H}_{spin} | \beta; J, M_J \rangle = - \frac{1}{2} M_J A_{iso} \tag{2.23b}$$

$$\langle \alpha; J, M_J | \mathcal{H}_{spin} | \beta; J, M_J + 1 \rangle = \sqrt{J(J+1) - M_J(M_J+1)}\, A_{iso} \tag{2.23c}$$

$$\langle \beta; J, M_J | \mathcal{H}_{spin} | \alpha; J, M_J - 1 \rangle = \sqrt{J(J+1) - M_J(M_J-1)}\, A_{iso} \tag{2.23d}$$

where

$$A_{iso} = \frac{1}{4} A^{A_1} \tag{2.24}$$

The resonant fields for the ESR transitions to the second order correction becomes as follows.

Nuclear spin states of A_1 symmetry with $J = 2$ (Case 1)

$$H = H_0 - A_{iso} M_J - \frac{1}{2H_0} A_{iso}{}^2 \left[J(J+1) - M_J{}^2 \right]$$

$$\text{with } M_J = -2, -1, 0, 1, 2 \tag{2.25}$$

Nuclear spin states of A_1 symmetry with $J = 0$ and of B_1 symmetry with $J = 0$ (Case 1)

$$H = H_0 \tag{2.26}$$

Nuclear spin states of B_2 symmetry with $J = 1$ (Case 2)

$$H = H_0 - A_{iso} M_J - \frac{1}{2H_0} A_{iso}{}^2 \left[J(J+1) - M_J{}^2 \right] \quad \text{with } M_J = -1, 0, 1 \tag{2.27}$$

Case 3 ($\Gamma_{rve} = E$);

Considering that the direct product of E for the rovibronic part and E for the nuclear spin part contains A_1, B_1, A_2, and B_2, and that A_1 and B_1 are allowed by the nuclear spin statistics, the total wave functions without the electron spin part must be in either form of eq. (2.28).

$$\begin{aligned} \Psi_{A_1} &= \frac{1}{\sqrt{2}} \left(|\text{rve}; E_x\rangle |\text{ns}; E_x\rangle + |\text{rve}; E_y\rangle |\text{ns}; E_y\rangle \right) \\ \Psi_{B_1} &= \frac{1}{\sqrt{2}} \left(|\text{rve}; E_x\rangle |\text{ns}; E_x\rangle - |\text{rve}; E_y\rangle |\text{ns}; E_y\rangle \right) \end{aligned} \tag{2.28}$$

The matrix elements of the isotropic hyperfine Hamiltonian are calculated by evaluating the expectation value of the Hamiltonian with the above Ψ_{A_1} or Ψ_{B_1}, and it can be shown that the elements are of the same forms as those in eq. (2.23) with $J = 1$ (see eq. (2.29)). In the evaluation of the matrix elements not only the Fermi term of A_1 symmetry but also that of B_2 symmetry have non-zero expectation values as shown by eq. (2.31).

$$\langle \alpha; J, M_J | \mathcal{H}_{hfc} | \alpha; J, M_J \rangle = +\frac{1}{2} M_J \widetilde{A}_{iso} \tag{2.29a}$$

$$\langle \beta; J, M_J | \mathcal{H}_{hfc} | \beta; J, M_J \rangle = -\frac{1}{2} M_J \widetilde{A}_{iso} \tag{2.29b}$$

$$\langle \alpha; J, M_J | \mathcal{H}_{hfc} | \beta; J, M_J + 1 \rangle = \sqrt{J(J+1) - M_J(M_J+1)}\, \widetilde{A}_{iso} \tag{2.29c}$$

$$\langle \beta; J, M_J | \mathcal{H}_{hfc} | \alpha; J, M_J - 1 \rangle = \sqrt{J(J+1) - M_J(M_J-1)}\, \widetilde{A}_{iso} \tag{2.29d}$$

where

$$\widetilde{A}_{iso} = \frac{1}{4}\left(A^{A_1} + A^{B_2}\right) \tag{2.30}$$

with

$$A^{A_1} = \langle \mathrm{rve}; E_x \,|\, T_f^{A_1} \,|\, \mathrm{rve}; E_x \rangle = \langle \mathrm{rve}; E_y \,|\, T_f^{A_1} \,|\, \mathrm{rve}; E_y \rangle$$
$$A^{B_2} = \langle \mathrm{rve}; E_x \,|\, T_f^{B_2} \,|\, \mathrm{rve}; E_x \rangle = \langle \mathrm{rve}; E_y \,|\, T_f^{B_2} \,|\, \mathrm{rve}; E_y \rangle \tag{2.31}$$

The resonant field for the ESR transition is

$$H = H_0 - \widetilde{A}_{iso} M_J - \frac{1}{2H_0} \widetilde{A}_{iso}{}^2 \left[J(J+1) - M_J{}^2\right]$$
$$\text{with } J = 1 \text{ and } M_J = -1, 0, 1 \tag{2.32}$$

Thus, it is predicted that the rovibronic states of A_1 or B_1 symmetry treated in Case 1 give ESR spectra of $J = 2$ and 0, and those of A_2 or B_2 symmetry in Case 2 give the spectrum of $J = 1$ both with the hfcc of $A^{A1}/4$, whereas the rovibronic states of E symmetry in Case 3 yield the spectrum of $J = 1$ with a different hfcc of $(A^{A1} + A^{B2})/4$. To the first order approximation the separation among the quintet components in Case 1 is equal to the separation among the triplet components in Case 2, that is, $A^{A1}/4$. However, due to the second order shift the former is larger than the latter on account of the larger value of $J(J+1)$. Therefore, the $M_J = \pm 1$ lines of the triplet in Case 2 must appear slightly to the right (high field side) of the $M_J = \pm 1$ signals of the quintet in Case 1 as shown in Figure 2.4. Meanwhile, another triplet in Case 3 is associated with a different separation $(A^{A1} + A^{B2})/4$ from those in Cases 1 and 2. If the latter separation is smaller than $A^{A1}/4$, we could correspond them to the "extra" lines between the $M_J = \pm 1$ of $J = 2$ states of $CH_4^{+\bullet}$ and the methyl lines which were mentioned in item (ii) above. However, this possibility can be denied because in the observed spectrum we do not see any sign of the appearance of the $M_J = \pm 1$ lines of the triplet expected in Case 2 which should appear to the right (high field side) of the $M_J = \pm 1$ lines of the quintet in Case 1 by a distinguishable amount of separation of $\Delta \frac{1}{2H_0} A_{iso}{}^2 \left[J(J+1) - M_J{}^2\right] \cong 1.8$ G. Thus, the tunneling between the two C_{2v} structures is ruled out.

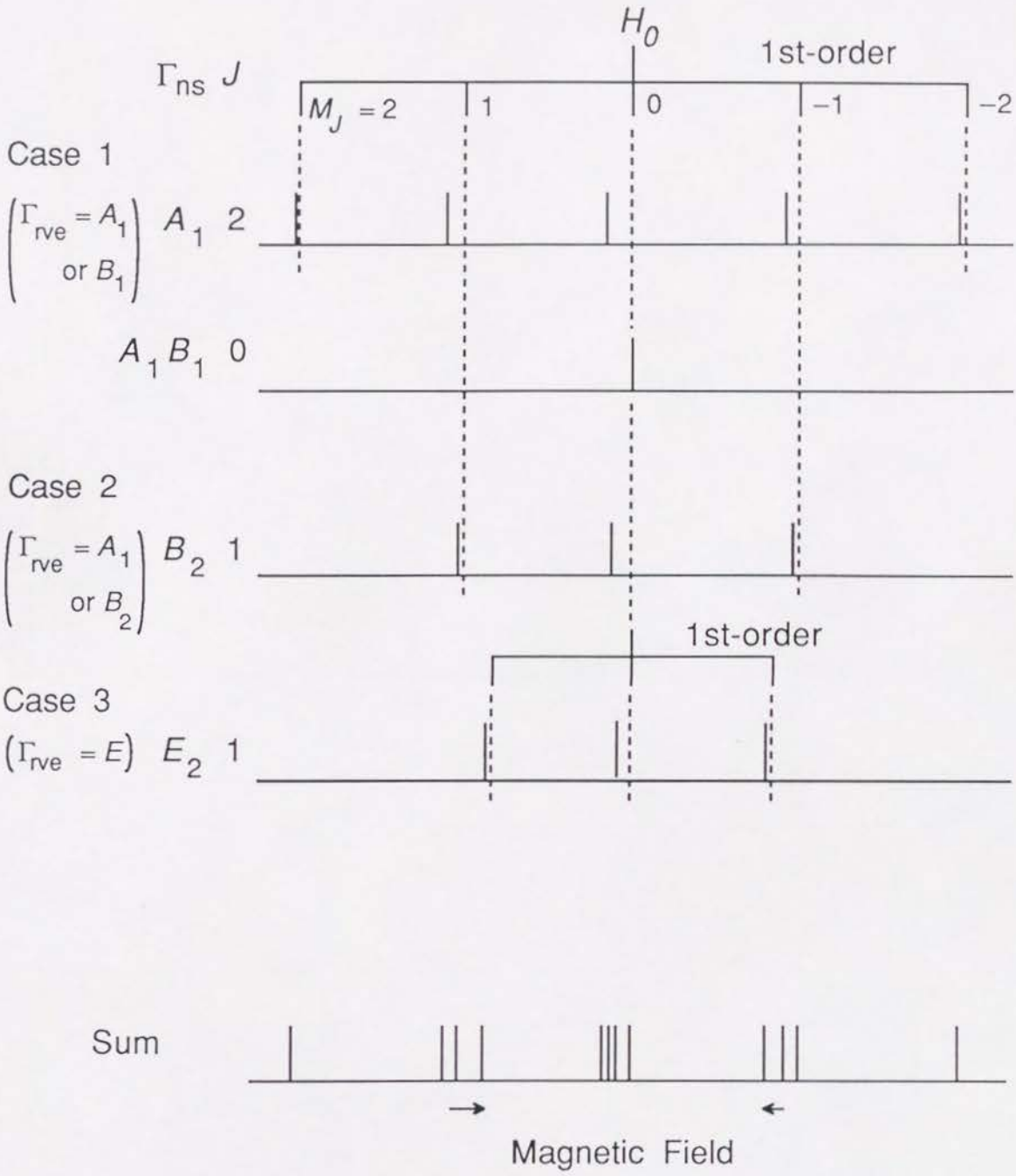

Figure 2.4 ESR spectral pattern of $CH_4^{+\bullet}$ of G_8 symmetry.

2) Tunneling Among the Six C_{2v} Structures

We will next consider the tunneling among the six equivalent C_{2v} structures shown in Scheme 2.2. The molecular symmetry group of the system is G_{24} which is isomorphous with the point group T_d of order of 24. According to Table 2.5 the symmetry of the total wavefunction must be A_1 or A_2 and from Table 2.6 the relation between Γ_{rve} and Γ_{ns} is restricted as follows.

	Γ_{rve}	Γ_{ns}
Case 1	A_1 or A_2	A_1
Case 2	E	E
Case 3	F_1 or F_2	F_2 (and F_1)

(2.33)

The nuclear spin state of F_1 symmetry is missing in $CH_4^{+\bullet}$, but the F_1 state is permissible for $CD_4^{+\bullet}$ as will be shown later by referring to Table 2.7. The parenthesis in Case 3 above is intended to call attention to this point.

From the correlation table between G_4 and G_{24} shown in Scheme 2.3, A_1 state in the rigid configuration will split into A_1, E, and F_2 states,whereas A_2 state splits into A_2, E, and F_1 states. Similarly, B_1 and B_2 states split into F_1 and F_2 states. As in the previous section, we assume that there is no accidental degeneracy and the hyperfine interaction between different rovibronic states can be neglected. Thus, the ESR spectrum can be predicted from the hyperfine Hamiltonian for each rovibronic level using the symmetrized nuclear spin functions given in Table 2.6. The analysis can be made in a similar way as before.

Table 2.5 Character table and direct product table of G_{24} of non-rigid $CH_4^{+\bullet}$.

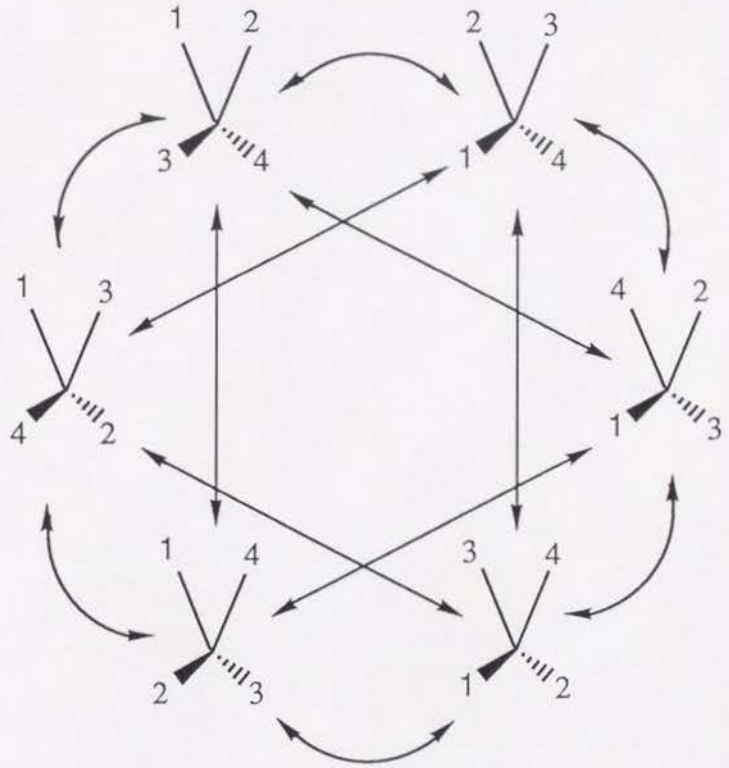

G_{24}	E	8 (123)	3 (14)(23)	6 (1423)*	6 (23)*
A_1	1	1	1	1	1
A_2	1	1	1	−1	−1
E	2	−1	2	0	0
F_1	3	0	−1	1	−1
F_2	3	0	−1	−1	1

G_{24}	A_1	A_2	E	F_1	F_2
A_1	A_1	A_2	E	F_1	F_2
A_2	A_2	A_1	E	F_2	F_1
E	E	E	$A_1 + \{A_2\} + E$	$F_1 + F_2$	$F_1 + F_2$
F_1	F_1	F_2	$F_1 + F_2$	$A_1 + E + \{F_1\} + F_2$	$A_2 + E + F_1 + F_2$
F_2	F_2	F_1	$F_1 + F_2$	$A_2 + E + F_1 + F_2$	$A_1 + E + \{F_1\} + F_2$

Table 2.6 Symmetrized operators and nuclear spin functions used for $CH_4^{+\bullet}$ of G_{24} symmetry.

Symmetrization of set of operators $\{X_1, X_2, X_3, X_4\}$[a]

$$X^{A_1} = X_1 + X_2 + X_3 + X_4$$
$$X^{F_{2x}} = X_1 - X_2 + X_3 - X_4$$
$$X^{F_{2y}} = -X_1 + X_2 + X_3 - X_4$$
$$X^{F_{2z}} = X_1 + X_2 - X_3 - X_4$$

Symmetrized representation of hyperfine Hamiltonian[b]

$$\mathcal{H}_{hfc} = \frac{1}{4}\mathbf{S}\cdot\left\{\mathbf{T}^{A_1}\cdot\mathbf{I}^{A_1} + \mathbf{T}^{F_{2x}}\cdot\mathbf{I}^{F_{2x}} + \mathbf{T}^{F_{2y}}\cdot\mathbf{I}^{F_{2y}} + \mathbf{T}^{F_{2z}}\cdot\mathbf{I}^{F_{2z}}\right\}$$

Symmetrized nuclear spin functions of the four protons [Hougen (1976)].

$$|A_1;2,2\rangle = |\alpha\alpha\alpha\alpha\rangle$$
$$|A_1;2,1\rangle = \frac{1}{\sqrt{4}}\left(|\beta\alpha\alpha\alpha\rangle + |\alpha\beta\alpha\alpha\rangle + |\alpha\alpha\beta\alpha\rangle + |\alpha\alpha\alpha\beta\rangle\right)$$
$$|A_1;2,0\rangle = \frac{1}{\sqrt{6}}\left(|\alpha\beta\alpha\beta\rangle + |\beta\alpha\beta\alpha\rangle + |\beta\alpha\alpha\beta\rangle + |\alpha\beta\beta\alpha\rangle + |\alpha\alpha\beta\beta\rangle + |\beta\beta\alpha\alpha\rangle\right)$$
$$|A_1;2,-1\rangle = \frac{1}{\sqrt{4}}\left(|\alpha\beta\beta\beta\rangle + |\beta\alpha\beta\beta\rangle + |\beta\beta\alpha\beta\rangle + |\beta\beta\beta\alpha\rangle\right)$$
$$|A_1;2,-2\rangle = |\beta\beta\beta\beta\rangle$$

$$|F_{2x};1,1\rangle = \frac{1}{\sqrt{4}}\left(-|\beta\alpha\alpha\alpha\rangle + |\alpha\beta\alpha\alpha\rangle - |\alpha\alpha\beta\alpha\rangle + |\alpha\alpha\alpha\beta\rangle\right)$$
$$|F_{2x};1,0\rangle = \frac{1}{\sqrt{2}}\left(|\alpha\beta\alpha\beta\rangle - |\beta\alpha\beta\alpha\rangle\right)$$
$$|F_{2x};1,-1\rangle = \frac{1}{\sqrt{4}}\left(|\alpha\beta\beta\beta\rangle - |\beta\alpha\beta\beta\rangle + |\beta\beta\alpha\beta\rangle - |\beta\beta\beta\alpha\rangle\right)$$

$$|F_{2y};1,1\rangle = \frac{1}{\sqrt{4}}\left(|\beta\alpha\alpha\alpha\rangle - |\alpha\beta\alpha\alpha\rangle - |\alpha\alpha\beta\alpha\rangle + |\alpha\alpha\alpha\beta\rangle\right)$$
$$|F_{2y};1,0\rangle = \frac{1}{\sqrt{2}}\left(|\beta\alpha\alpha\beta\rangle - |\alpha\beta\beta\alpha\rangle\right)$$
$$|F_{2y};1,-1\rangle = \frac{1}{\sqrt{4}}\left(-|\alpha\beta\beta\beta\rangle + |\beta\alpha\beta\beta\rangle + |\beta\beta\alpha\beta\rangle - |\beta\beta\beta\alpha\rangle\right)$$

$$|F_{2z};1,1\rangle = \frac{1}{\sqrt{4}}\left(-|\beta\alpha\alpha\alpha\rangle - |\alpha\beta\alpha\alpha\rangle + |\alpha\alpha\beta\alpha\rangle + |\alpha\alpha\alpha\beta\rangle\right)$$
$$|F_{2z};1,0\rangle = \frac{1}{\sqrt{2}}\left(|\alpha\alpha\beta\beta\rangle - |\beta\beta\alpha\alpha\rangle\right)$$
$$|F_{2z};1,-1\rangle = \frac{1}{\sqrt{4}}\left(|\alpha\beta\beta\beta\rangle + |\beta\alpha\beta\beta\rangle - |\beta\beta\alpha\beta\rangle - |\beta\beta\beta\alpha\rangle\right)$$

$$|E_a;0,0\rangle = \frac{1}{\sqrt{12}}\left(2|\alpha\alpha\beta\beta\rangle + 2|\beta\beta\alpha\alpha\rangle - |\alpha\beta\alpha\beta\rangle - |\beta\alpha\beta\alpha\rangle - |\beta\alpha\alpha\beta\rangle - |\alpha\beta\beta\alpha\rangle\right)$$
$$|E_b;0,0\rangle = \frac{1}{\sqrt{4}}\left(|\alpha\beta\alpha\beta\rangle + |\beta\alpha\beta\alpha\rangle - |\beta\alpha\alpha\beta\rangle - |\alpha\beta\beta\alpha\rangle\right)$$

[a] $\mathbf{X}_i$ is the hyperfine interaction operator $\mathbf{T}_i$ or the nuclear spin operator $\mathbf{I}_i$.

[b] The anisotropy of $\mathbf{T}$ tensor is neglected in the present analysis and only the Fermi term T_f is considered.

Case 1 ($\Gamma_{rve} = A_1$ or A_2);

Since the rovibronic level is non-degenerate and the associated nuclear spin function is of A_1 symmetry with $J = 2$, the spin Hamiltonian and the matrix elements are exactly the same as in eqs. (2.22) and (2.23). The resonant field for the ESR transition is

$$H = H_0 - A_{iso} M_J - \frac{1}{2H_0} A_{iso}{}^2 \left[J(J+1) - M_J{}^2 \right]$$

$$\text{with } J = 2 \; M_J = -2, -1, 0, 1, 2 \qquad (2.34)$$

with

$$A_{iso} = \frac{1}{4} A^{A_1} \quad \text{and} \quad A^{A_1} = \langle \text{rve}; \Gamma_{\text{rve}} | T_f^{A_1} | \text{rve}; \Gamma_{\text{rve}} \rangle \qquad (2.24,21)$$

Case 2 (Γ_{rve} =E);

Since the symmetry of the total wavefunction must be A_1 or A_2, the total wave functions without the electron spin part are given by,

$$\Psi_{A_1} = \frac{1}{\sqrt{2}} \left(|\text{rve}; E_a\rangle |\text{ns}; E_a\rangle + |\text{rve}; E_b\rangle |\text{ns}; E_b\rangle \right)$$
$$\Psi_{A_2} = \frac{1}{\sqrt{2}} \left(|\text{rve}; E_a\rangle |\text{ns}; E_a\rangle - |\text{rve}; E_b\rangle |\text{ns}; E_b\rangle \right) \qquad (2.35)$$

Since the accompanying nuclear spin functions of E symmetry have $J = 0$, there is no hyperfine interaction in these levels. The resonant field for ESR transition is just equal to the field corresponding to the Zeeman interaction,

$$H = H_0 \qquad (2.36)$$

Case 3 ($\Gamma_{rve} = F_1$ or F_2);

From the triply degenerate rovibronic states of symmetry of F_1 and F_2 a total wavefunction of A_2 and of A_1 symmetry is constructed, respectively, as follows (see the direct product table in Table 2.5).

$$\Psi_{A_2} = \frac{1}{\sqrt{3}}\left(|\mathrm{rve};F_{1_x}\rangle|\mathrm{ns};F_{2_x}\rangle + |\mathrm{rve};F_{1_y}\rangle|\mathrm{ns};F_{2_y}\rangle + |\mathrm{rve};F_{1_z}\rangle|\mathrm{ns};F_{2_z}\rangle\right)$$
$$\Psi_{A_1} = \frac{1}{\sqrt{3}}\left(|\mathrm{rve};F_{2_x}\rangle|\mathrm{ns};F_{2_x}\rangle + |\mathrm{rve};F_{2_y}\rangle|\mathrm{ns};F_{2_y}\rangle + |\mathrm{rve};F_{2_z}\rangle|\mathrm{ns};F_{2_z}\rangle\right) \quad (2.37)$$

Being not a simple product of the rovibronic and the spin parts, the calculation of the matrix elements of the hyperfine Hamiltonian is a little bit complicated. However, it can be shown that the matrix elements are of the same forms as those in eqs. (2.29a) – (2.29d) but the constant is to be replaced from that in eq. (2.29) to that in eq. (2.38).

$$\tilde{A}_{iso} = \frac{1}{4}\left(A^{A_1} + 2A^{F_2}\right) \quad (2.38)$$

where

$$A^{A_1} = \langle \mathrm{rve};F_{1_x}|T_f^{A_1}|\mathrm{rve};F_{1_x}\rangle \quad \text{and} \quad A^{F_2} = \langle \mathrm{rve};F_{1_x}|T_f^{F_{2y}}|\mathrm{rve};F_{1_z}\rangle \quad (2.39)$$

for the rovibronic state of F_1 symmetry and

$$A^{A_1} = \langle \mathrm{rve};F_{2_x}|T_f^{A_1}|\mathrm{rve};F_{2_x}\rangle \quad \text{and} \quad A^{F_2} = \langle \mathrm{rve};F_{2_x}|T_f^{F_{2y}}|\mathrm{rve};F_{2_z}\rangle \quad (2.40)$$

for the rovibronic state of F_2 symmetry.

The resonant field for the ESR transition is given by,

$$H = H_0 - \tilde{A}_{iso}M_J - \frac{1}{2H_0}\tilde{A}_{iso}^{\,2}\left[J(J+1) - M_J^{\,2}\right]$$
$$\text{with } J = 1 \text{ and } M_J = -1, 0, 1 \quad (2.41)$$

Thus, the rovibronic state of A_1 or A_2 symmetry in Case 1 gives the ESR spectrum of $J = 2$ with the hyperfine coupling constant of $A^{A1}/4$, and the rovibronic state of E symmetry in Case 2 gives the spectrum of $J = 0$. All the $J = 1$ spin states are associated with F_1 or F_2 rovibronic states in Case 3 to give a different hfcc of $(A^{A1} + 2A^{F2})/4$. These spectral features are schematically shown in Figure 2.5 under the assumption that the hfcc for Case 3 is smaller than that for Case 1.

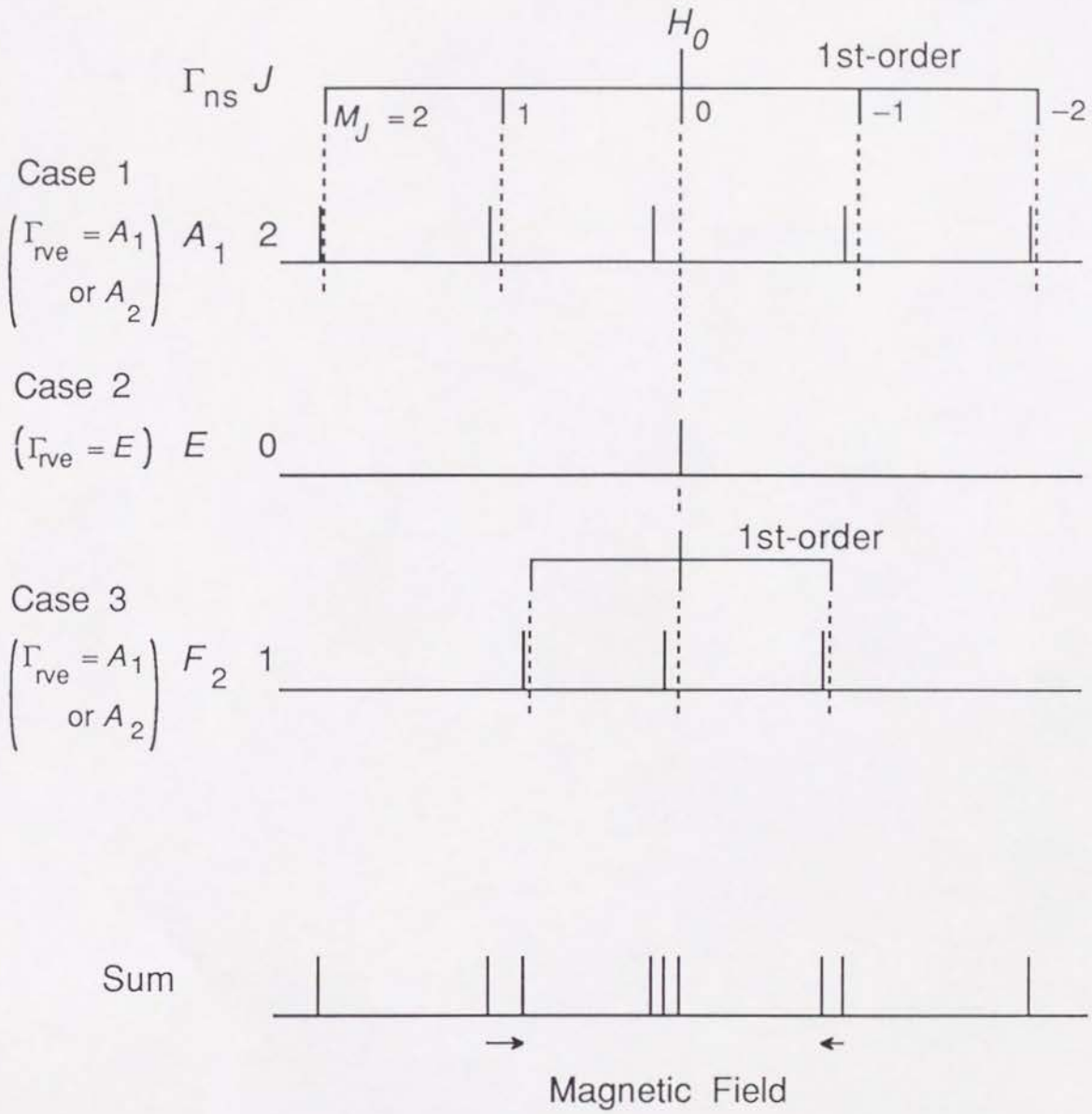

Figure 2.5 ESR spectral pattern of $CH_4^{+\bullet}$ of G_{24} symmetry..

The spectral pattern is consistent with the observed spectra. In particular, the appearance of the "extra" lines is now understood as due to the triplet originating from Case 3 discussed above. It is noteworthy that the separation between the two manifolds of $M_J = -1$ originating from Cases 1 and 3 is smaller than the separation between the manifolds of $M_J = +1$ on account of the second order shift (see the horizontal arrows in Figure 2.5), which is in agreement with the observed spectra. Since the rotational energy gap in the local C_{2v} structure should be very small as judged from the result of the analysis of $CH_2D_2^{+\bullet}$, the thermal population of $\Gamma_{ns} = F_2$ states is considered to be enough to give an observable intensity of the transitions at 4 K. The apparent disappearance of the "extra" lines at 4 K is, therefore, considered as due to an extreme line broadening in the part of 2 A^{F2} at 4 K probably owing to an increased inhomogeneity of the medium at the low temperature. As for the splitting of the "extra" lines into doublets and the gradual widening of the hyperfine splitting with the temperature further considerations are needed. At present we conjecture that the gradual change of the hyperfine splitting with the temperature may be a reflection of some crystalline field effect which cannot be dealt with the present molecular symmetry group theoretic analysis. A method of extending the molecular symmetry group theory to treat molecules in crystalline fields has been proposed [Miller and Decius (1973)]. However, since the experimental information about the crystal field of the methane cation in solid neon is scarce [Jones *et al.* (1986)], we will not go further at the moment.

$CD_4^{+\bullet}$

The ESR spectra of $CD_4^{+\bullet}$ at 2.8 K and 6.5 K are shown in Figure 2.6. The equally spaced 9 lines with $A_{iso}(D) = 7.9$ G are comparable with the quintet of $CH_4^{+\bullet}$ because $A_{iso}(D) = 7.9$ G corresponds to 52 G on the H scale. The good correspondence implies that a similar averaging process to that in $CH_4^{+\bullet}$ is operative in $CD_4^{+\bullet}$ also. However, since the second order shift is so small in the latter, i.e., $A_{iso}^2/2H_0 \approx 0.01$ G, we cannot distinguish J in the same M_J manifold. In a remarkable contrast to $CH_4^{+\bullet}$ the "extra" lines with different hfcc's do not appear in the spectra which prevents similar analyses to those made for $CH_4^{+\bullet}$. However, the deviation of the intensity pattern from the normal 1:4:10:16:19:16:10:4:1 ratio at 2.8 K gives a useful clue for unveiling the averaging process in $CD_4^{+\bullet}$: Since the symmetry of the total wavefunction of $CD_4^{+\bullet}$ must be A_1 or A_2, the nuclear spin state must be restricted by the symmetry of the rovibronic state as is summarized in Table 2.7. The non-zero isotropic hfcc's in the fourth column of Table 2.7 can be determined from these rovibronic states, and the spectral pattern is given as in the fifth column. The hfcc's of the F_1 and F_2 nuclear spin states can be different on account of the additional component of A^{F2}. If this value of A^{F2} is very sensitive to the crystalline field and subject to broadening due to the inhomogenity of the field as the component of A^{F2} in $CH_4^{+\bullet}$ at 4 K, the ESR lines originating from the F_1 and F_2 nuclear spin states are spread out and only the lines of A_1 and E spin states should be observed. Under such a circumstance the observed spectral pattern would be the Boltzmann-weighted average of the two states. However, if the effect of the thermal population is negligible, the intensity ratio will be given by just the sum of the patterns originating from the nuclear spin functions of symmetries of A_1 and E, and we will have the intensity ratio of the statistical, or the high-temperature limit, i.e., 1:1:4:4:7:4:4:1:1. This ratio turned out to be close to the observed intensity pattern at 2.8 K. The approximately normal intensity ratio of 1:4:10:16:19:16:10:4:1 at 6.5 K is regarded as similar to the dwindling of the contribution of A^{F2} in the case of $CH_4^{+\bullet}$. The behavior of the F_1 and F_2 nuclear spin states could be different from that of $CH_4^{+\bullet}$, because the tunneling could be very sensitive to the crystalline field so that the change in the (zero point) vibrational energy could cause a significant change in the additional term of A^{F2} in the F_1 and F_2 states. Thus, it is understandable that the extra transitions with a different hfcc cannot be observed in $CD_4^{+\bullet}$ contrary to the case of $CH_4^{+\bullet}$.

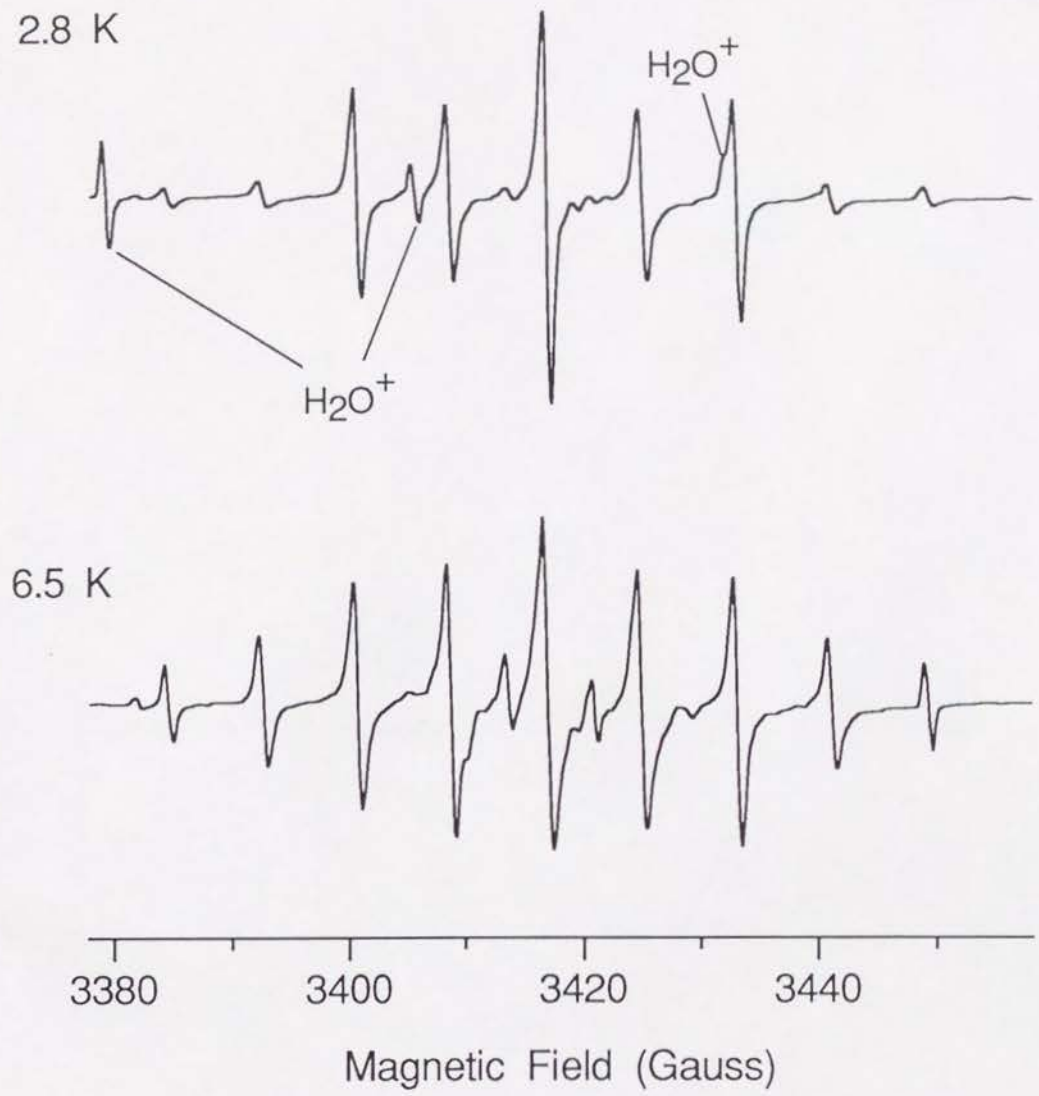

Figure 2.6 ESR spectra of $CD_4^{+\bullet}$ isolated in neon matrix at 2.8 K and 6.5 K. The background signals due to $H_2O^{+\bullet}$ almost disappear at 6.5 K.

Table 7 The ESR intensity pattern predicted for each rovibronic state of $CD_4^{+\bullet}$.

Γ_{rve}	Γ_{ns}[a]	Γ_{total}	non-zero A_{iso}	ESR intensity pattern
A_1 or A_2	A_1 ($J = 4, 2, 0$)	A_1 or A_2	A^{A1}	1 : 1 : 2 : 2 : 3 : 2 : 2 : 1 : 1
E	E ($J = 2, 0$)	A_1 and A_2	A^{A1}	2 : 2 : 4 : 2 : 2
F_1 or F_2	F_1 ($J = 1$) and F_2 ($J = 3, 2, 1$)	A_1 and A_2	A^{A1} and A^{F2}	1 : 2 : 4 : 4 : 4 : 2 : 1

[a]Hougen (1976).

On the possibility of D_{2d} or C_{3v} distortion of $CH_4^{+\bullet}$ and $CD_4^{+\bullet}$

In the preceding section we have shown that the observed ESR spectra can be accounted for by the tunneling among the six C_{2v} structures. In this section we will examine the possibility of the tunneling among C_{3v} and D_{2d} structures. This is a necessary procedure because the argument on $CH_4^{+\bullet}$ and $CD_4^{+\bullet}$ in terms of G_{24} is, in principle, compatible not only with the C_{2v} but also with the C_{3v} and D_{2d} distortion. Likewise, the argument on $CH_2D_2^{+\bullet}$ in terms of G_4 does not necessarily exclude the possibility of the C_{3v} distortion. It will be concluded, however, that these possibilities can be ruled out most probably by referring to the experimental ESR spectra of $CH_3D^{+\bullet}$ and $CD_3H^{+\bullet}$. Before proceeding to these systems we will enumerate pieces of counter evidence to the mentioned possibilities.

If the most stable structure of $CH_4^{+\bullet}$ and/or $CD_4^{+\bullet}$ were D_{2d} distorted and an averaging took place among the equivalent D_{2d} structures, the electronic structure of the local minimum would be different from that of $CH_2D_2^{+\bullet}$, which has been shown definitely to be of $^2B_1$ symmetry [Knight *et al.* (1984)]. If the electronic state of the stable structure were different from that of $CH_2D_2^{+\bullet}$, it would be difficult to account for the excellent agreement of the averaged hfcc's of $CH_4^{+\bullet}$ and $CD_4^{+\bullet}$ with that of $CH_2D_2^{+\bullet}$ on the H-scale. Moreover, theoretical calculations of $CH_4^{+\bullet}$ indicate that the D_{2d} structure corresponds to one of the saddle points on the potential surface of $CH_4^{+\bullet}$ [Paddon-Row *et al.* (1985), Takeshita (1987), Frey and Davidson (1988)].

If only the spectra of $CH_2D_2^{+\bullet}$, $CH_4^{+\bullet}$, and $CD_4^{+\bullet}$ were available, we could not conclude exclusively that the averaging in $CH_4^{+\bullet}$ be among the C_{2v} structures because the tunneling among the "C_{3v}" structures in Scheme 2.4 could also average the hfcc's of the two protons and the two deuterons of $CH_2D_2^{+\bullet}$. The vertical C-H bond in (A) and the vertical C-D bond in (B) are assumed to be the C_3 axis of the C_{3v} ion.
Therefore, one might have to worry about the possibility that the same C_{3v} tunneling were operative in $CH_4^{+\bullet}$ also. However, the following examination of this C_{3v} mechanism for $CH_2D_2^{+\bullet}$ eliminates the possibility: Since the experimental values of $CH_2D_2^{+\bullet}$ are $A_{iso}(2H) = +122$ G and $|A_{iso}(2D)| = 15$ G on the H-scale, the H-scale hfcc of the three basal "protons" in (A) must the -15 G if $A_{iso}(2D)$ of $CH_2D_2^{+\bullet}$ is negative and the hfcc of the proton on the C_3 axis be +259 G because the average of the hfcc's of the two protons in the system (A) must be equal to the observed hfcc of +122 G of $CH_2D_2^{+\bullet}$. Likewise, for the case of $A_{iso}(2D) > 0$ the three basal "protons" and the top proton must have hfcc's of +15 G and +229 G, respectively. Similarly, in the system (B) the three basal "protons" must have the hfcc of +122 G and the H-scale hfcc of the deuteron on the C_3 axis must be -152 G for the case of $A_{iso}(2D) < 0$ and be -92 G for the case of $A_{iso}(2D) > 0$. All these cases predicting hfcc's of +259, +229, -152 , and -92 G for the top "proton" are obviously unacceptable.

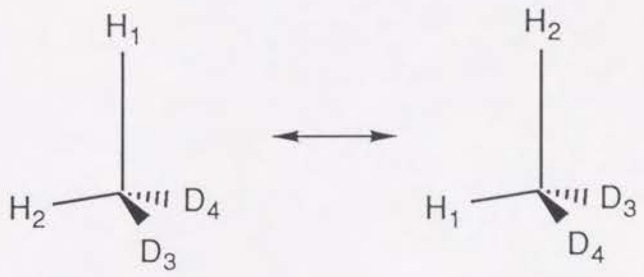

(A)

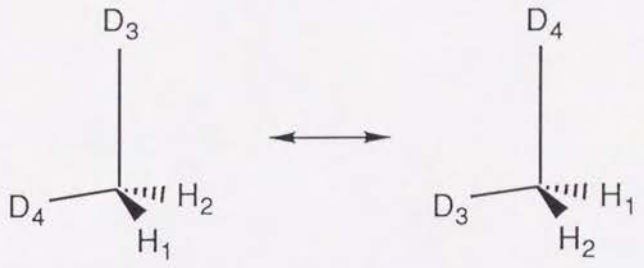

(B)

Scheme 2.4

$CH_3D^{+\bullet}$ and $CD_3H^{+\bullet}$

The ESR spectra of $^{12}CH_3D^{+\bullet}$ at 8 K and $^{13}CH_3D^{+\bullet}$ at 11K are shown in Figure 2.7. Although not shown, we also have observed the spectrum for $CD_3H^{+\bullet}$. Both spectra of $CH_3D^{+\bullet}$ and $CD_3H^{+\bullet}$ indicate that the three protons and the three deuterons are equivalent in the ESR time scale. However, these spectra cannot be associated with a rigid C_{3v} structure because the H-atom scale hfcc's of the two isotopomers are so different each other as shown in Table 2.8 that the rigid structures of the two isotopomers would have to be unnaturally different. Therefore, we should regard the systems as non-rigid as in the cases of $CH_4^{+\bullet}$ and $CD_4^{+\bullet}$ and consider an averaging process. If we consider tunnelings among the C_{2v} structures shown in Schemes 2.5 and 2.6, which are drawn under the assumption that the shorter bond length of C-D in $CH_2D_2^{+\bullet}$ is retained in $CH_3D^{+\bullet}$ and that the longer bond length of C-H in $CH_2D_2^{+\bullet}$ is retained in $CD_3H^{+\bullet}$ [Paddon-Row *et al.* (1985)], the three protons and the single deuteron in $CH_3D^{+\bullet}$ should be associated with the hfcc's of $(122 \times 2 - 15)/3 = 73$ G and -15 G, respectively, in reference to $CH_2D_2^{+\bullet}$. These are in a

good agreement with the observed values in Table 2.8. Likewise, for $CD_3H^{+\bullet}$ we should assign $(122 - 15 \times 2)/3 = 31$ G to $A_{iso}(3D)$ and +122 G to $A_{iso}(H)$, which are also in an excellent agreement with those in Table 2.8. Therefore, it is concluded that both $CH_3D^{+\bullet}$ and $CD_3H^{+\bullet}$ undergo the tunneling among the three equivalent C_{2v} structures. The conclusion of the C_{2v} local minimum for all the isotopomers is consistent with the experimental result of the coincidence spectroscopy utilizing Coulomb-explosion [Vager *et al.* (1986)] and with recent theoretical predictions [Meyer (1973), Paddon-Row *et al.* (1985), Takeshita (1987), Frey and Davidson (1988)]. With all these results we now recognize that all the tunneling processes operating in all the isotopomers are pseudo-rotation [Paddon-Row *et al.* (1985)]. Recently, the symmetries of the ground vibronic states are investigated by Reeves and Davidson (1991).

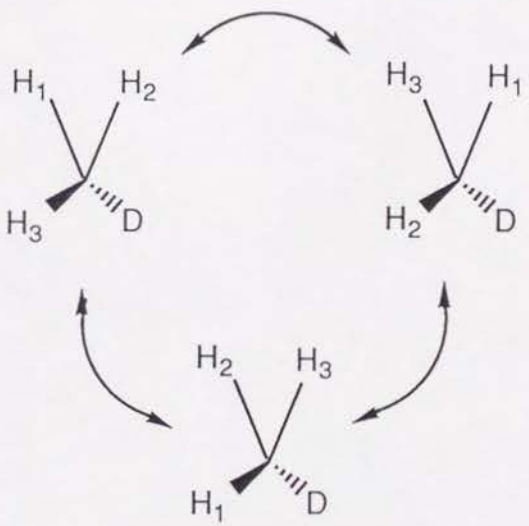

Scheme 2.5

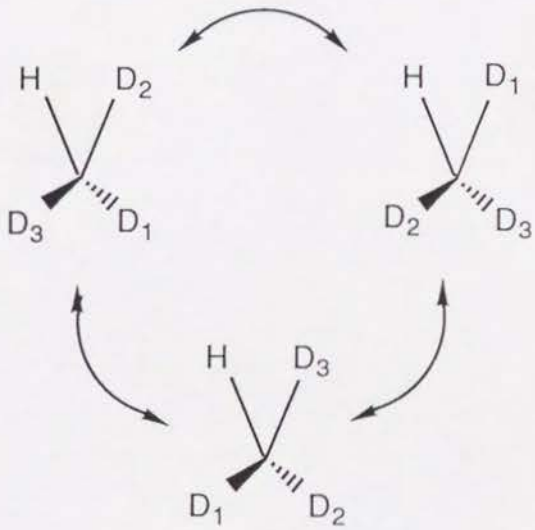

Scheme 2.6

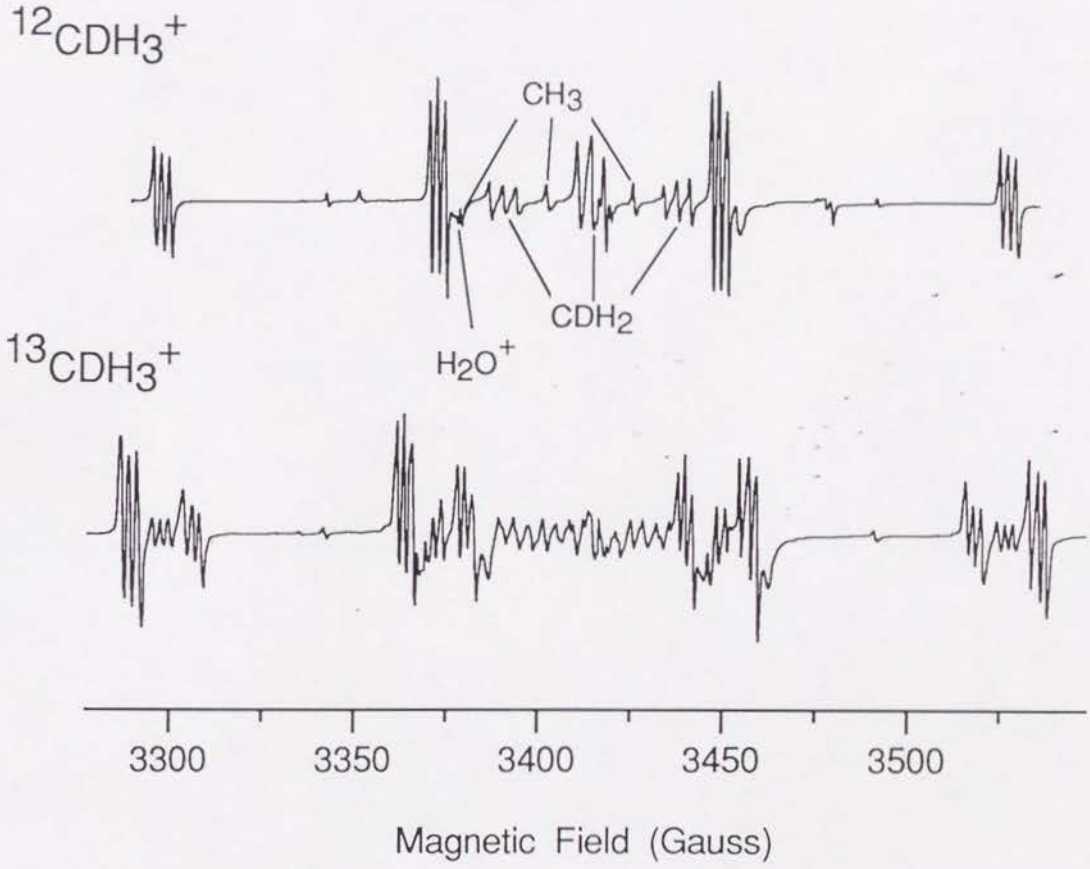

Figure 2.7 ESR spectra of $^{12}CH_3D^{+\bullet}$ and $^{13}CH_3D^{+\bullet}$ isolated in neon matrix at 8 K and 11 K, respectively. The spectrum of $^{12}CH_3D^{+\bullet}$ consists of a widely spaced quartet due to the three equivalent protons. Each quartet line shows a triplet hyperfine pattern associated with the deuteron ($I = 1$). The spectrum of $^{13}CH_3D^{+\bullet}$ reveals ^{13}C ($I = 1/2$) hyperfine doublets.

Table 2.8 Isotropic hyperfine coupling constants (hfcc's) of the radical cation of methane in neon matrices

	H	D[a]	^{13}C
$CH_4^{+\bullet}$	55	–	$A_\perp = +19$ $A_{\|\|} = +11$
$CH_3D^{+\bullet}$	76	−13	17
$CH_2D_2^{+\bullet}$	122	−15	–
$CD_3H^{+\bullet}$	125	30	–
$CD_4^{+\bullet}$	–	52	–

in units of Gauss.

[a]D hfcc on H atom scale.

The group theoretic analysis for $CH_3D^{+\bullet}$ and $CD_3H^{+\bullet}$ goes just like in the other cases; the appropriate molecular symmetry group for these systems is G_6 whose character table is given in Table 2.9. The symmetrized operators and nuclear spin functions for $CH_3D^{+\bullet}$ are given in Table 2.10.

In the following we will analyze the non-rigid system of $CH_3D^{+\bullet}$, representatively. The symmetry of the total wavefunction must be A_1 or A_2 and the relation between Γ_{rve} and Γ_{ns} becomes as follows.

	Γ_{rve}	Γ_{ns}
Case 1	A_1 or A_2	A_1
Case 2	E	E

(2.42)

As in the analysis of the other systems the above two cases will be treated separately. Since the spin function of the deuteron in $CH_3D^{+\bullet}$ is totally symmetric, we only need to concentrate our attention on the three protons in $CH_3D^{+\bullet}$.

Table 2.9 The character table of G_6 of non-rigid $CH_3D^{+\bullet}$ and $CD_3H^{+\bullet}$.

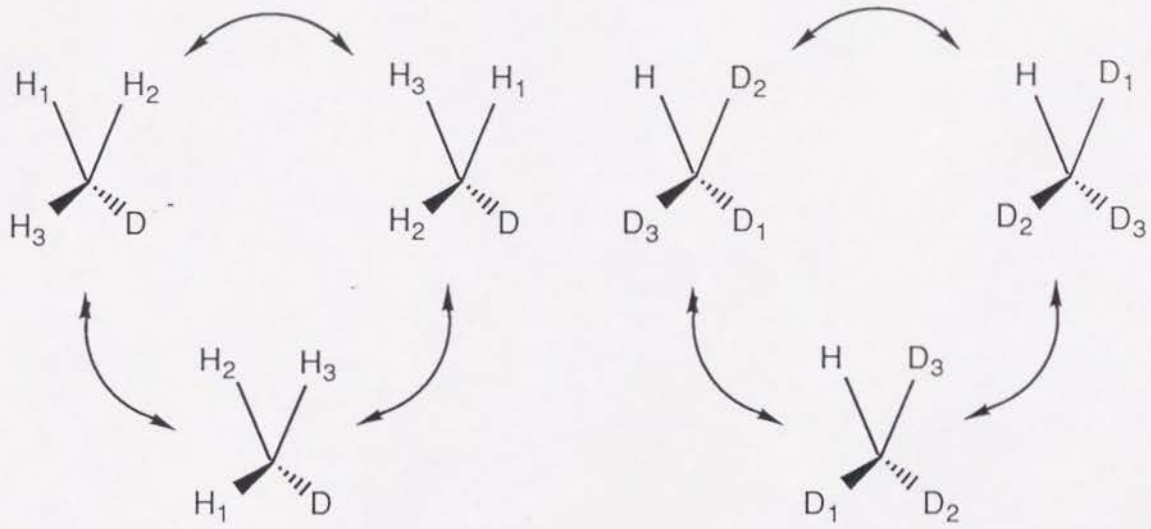

G_6	E	(123) (132)	(12)* (23)* (13)*
A_1	1	1	1
A_2	1	1	−1
E	2	−1	0

Table 2.10 **Symmetrized operators and nuclear spin functions used for $CH_3D^{+\bullet}$ of G_6 symmetry** [Freed (1965), Clough and Poldy (1969)].

Symmetrization of set of operators $\{X_1, X_2, X_3\}$[a]

$$X^{A_1} = X_1 + X_2 + X_3$$
$$X^{E_a} = X_1 + \varepsilon X_2 + \varepsilon^* X_3$$
$$X^{E_b} = X_1 + \varepsilon^* X_2 + \varepsilon X_3$$

where

$$\varepsilon = \exp(2\pi i/3)$$

Symmetrized representation of hyperfine Hamiltonian[b]

$$\mathcal{H}_{hfc} = \frac{1}{3}\,\mathbf{S}\cdot\left\{\mathbf{T}^{A_1}\cdot\mathbf{I}^{A_1} + \mathbf{T}^{E_a}\cdot\mathbf{I}^{E_b} + \mathbf{T}^{E_b}\cdot\mathbf{I}^{E_a}\right\}$$

Symmetrized nuclear spin functions of the three protons

$$|A_1; 3/2, 3/2\rangle = |\alpha\alpha\alpha\rangle$$
$$|A_1; 3/2, 1/2\rangle = \frac{1}{\sqrt{3}}\left(|\beta\alpha\alpha\rangle + |\alpha\beta\alpha\rangle + |\alpha\alpha\beta\rangle\right)$$
$$|A_1; 3/2, -1/2\rangle = \frac{1}{\sqrt{3}}\left(|\alpha\beta\beta\rangle + |\beta\alpha\beta\rangle + |\beta\beta\alpha\rangle\right)$$
$$|A_1; 3/2, -3/2\rangle = |\beta\beta\beta\rangle$$

$$|E_a; 1/2, 1/2\rangle = \frac{1}{\sqrt{3}}\left(-|\beta\alpha\alpha\rangle - \varepsilon|\alpha\beta\alpha\rangle - \varepsilon^*|\alpha\alpha\beta\rangle\right)$$
$$|E_a; 1/2, -1/2\rangle = \frac{1}{\sqrt{3}}\left(|\alpha\beta\beta\rangle + \varepsilon|\beta\alpha\beta\rangle + \varepsilon^*|\beta\beta\alpha\rangle\right)$$

$$|E_b; 1/2, 1/2\rangle = \frac{1}{\sqrt{3}}\left(-|\beta\alpha\alpha\rangle - \varepsilon^*|\alpha\beta\alpha\rangle - \varepsilon|\alpha\alpha\beta\rangle\right)$$
$$|E_b; 1/2, -1/2\rangle = \frac{1}{\sqrt{3}}\left(|\alpha\beta\beta\rangle + \varepsilon^*|\beta\alpha\beta\rangle + \varepsilon|\beta\beta\alpha\rangle\right)$$

[a] $\mathbf{X}_i$ is the hyperfine interaction operator $\mathbf{T}_i$ or the nuclear spin operator $\mathbf{I}_i$.

[b] The anisotropy of $\mathbf{T}$ tensor is neglected in the present analysis and only the Fermi term T_f is considered.

Case 1 ($\Gamma_{rve} = A_1$ or A_2);

For the non-degenerate rovibronic states the spin Hamiltonian is given by eq. (2.43).

$$\mathcal{H}_{spin} = \frac{1}{3} A^{A_1} \mathbf{S} \cdot \mathbf{I}^{A_1} \tag{2.43}$$

with

$$A^{A_1} = \langle \text{rve}; \Gamma_{\text{rve}} | T_f^{A_1} | \text{rve}; \Gamma_{\text{rve}} \rangle \tag{2.21}$$

The matrix elements of the Hamiltonian is given eq. (2.23) by substituting $J = 3/2$. The resonant field for the ESR transition including the second order correction is

$$H = H_0 - A_{iso} M_J - \frac{1}{2H_0} A_{iso}^2 \left[J(J+1) - M_J^2 \right]$$
$$\text{with } J = 3/2 \text{ and } M_J = -3/2, -1/2, 1/2, 3/2 \tag{2.44}$$

where

$$A_{iso} = \frac{1}{3} A^{A_1} \tag{2.45}$$

Case 2 ($\Gamma_{rve} = E$);

For the doubly degenerate rovibronic states, the total wave functions (except for the electron spin part) must have either of the following forms.

$$\Psi_{A_1} = \frac{1}{\sqrt{2}} \left(|\text{rve}; E_a\rangle |\text{ns}; E_a\rangle + |\text{rve}; E_b\rangle |\text{ns}; E_b\rangle \right)$$
$$\Psi_{A_2} = \frac{1}{\sqrt{2}} \left(|\text{rve}; E_a\rangle |\text{ns}; E_a\rangle - |\text{rve}; E_b\rangle |\text{ns}; E_b\rangle \right) \tag{2.46}$$

The matrix element of the hyperfine Hamiltonian again has the same form as eq. (2.29) to give an usual expression for the resonant field including the second order correction. However, the hfcc given in eq. (2.49) is different from A_{iso} in eq. (2.45).

$$H = H_0 - \tilde{A}_{iso} M_J - \frac{1}{4H_0} \tilde{A}_{iso}^{\,2}$$

$$\text{with } M_J = -1/2,\ 1/2 \tag{2.47}$$

where

$$\tilde{A}_{iso} = \frac{1}{3}\left(A^{A_1} - 2A^{E}\right) \qquad \text{for } \Psi_{A1} \tag{2.48}$$

$$\tilde{A}_{iso} = \frac{1}{3}\left(A^{A_1} + 2A^{E}\right) \qquad \text{for } \Psi_{A2}$$

and

$$A^{A_1} = \langle \text{rve};\, E_a \,|\, T_f^{A_1} \,|\, \text{rve};\, E_a \rangle = \langle \text{rve};\, E_b \,|\, T_f^{A_1} \,|\, \text{rve};\, E_b \rangle$$
$$A^{E} = \langle \text{rve};\, E_a \,|\, T_f^{E_b} \,|\, \text{rve};\, E_b \rangle = \langle \text{rve};\, E_b \,|\, T_f^{E_a} \,|\, \text{rve};\, E_a \rangle \tag{2.49}$$

The transitions of the states with $J = 1/2$ and $M_J = \pm 1/2$ will split into doublets by a separation of $2/3\ A^E$. Thus, the situation is the same as the tunneling rotation of the methyl group attached to a C or O atom having $2p$ unpaired electron, where the ESR transitions of the states with $J = 1/2$ and $M_J = \pm 1/2$ split into doublets at very low temperatures [Freed (1965), Clough and Poldy (1969), Davidson and Miyagawa (1970)].

The notable feature in the spectrum of $CH_3D^{+\bullet}$ is that the $J = 1/2$ lines is apparently missing; the positions of the four triplets at 3301.8, 3376.3, 3452.4, and 3530.5 G are in good agreement with the prediction by eq. (2.44) which are 3301.8, 3376.3, 3452.4, and 3530.2 G, respectively ($J = 3/2$, $A_{iso} = 76.2$ G). Therefore the four triplets are associated with the four sublevels of the proton spin functions of $J = 3/2$ and should have equal integrated intensity. Because the outer two triplets are slightly broader than the inner two, the peak height of the outer triplets in the derivative spectrum is smaller than that of inner two. A probable explanation of the apparent disappearance of the signals associated with $J = 1/2$ states is that the additional hfcc of A^E is subject to the broadening due to the static inhomogeneity of the crystal field just as the hfcc of the F_2 nuclear spin states of $CH_4^{+\bullet}$ and/or to the broadening due to the state-mixing between the two states in eq. (2.46), which is just like the tunneling rotation of the methyl group [Clough and Poldy (1969), Matsushita *et al.* (1990a)]. The broad hump on the right hand side (the higher-field side) of the inner two triplets associated with $J = 3/2$ and $M_J = 1/2$ states might be the broadened signals of $J = 1/2$ states.

A comment on the hfcc of ^{13}C

We have measured the hfcc of ^{13}C from the ESR spectra of $^{13}CH_3D^{+\bullet}$ and $^{13}CH_4^{+\bullet}$. From the spectrum of $^{13}CH_3D^{+\bullet}$ shown in Fig. 7 the hfcc of ^{13}C is determined as A_{iso} = 17 G. The other ^{13}C containing species, $^{13}CH_4^{+\bullet}$, shows an anisotropic feature in the ESR spectrum. The anisotropy is approximately axially symmetric and the hfcc's are $A_{\perp}$ = +19 G and $A_{||}$ = +11 G. Since the completely isolated $CH_4^{+\bullet}$ system described by G_{24} group must have an isotropic hfcc of ^{13}C, the observed anisotropy is due to the crystal field of the neon matrix.

Conclusion

The apparently anomalous behavior of the ESR pattern of $CH_4^{+\bullet}$ in the neon matrix can be elucidated by considering the tunneling among the six equivalent C_{2v} structures. All the deuterium substituted cations, i.e., $CH_3D^{+\bullet}$, $CH_2D_2^{+\bullet}$, $CD_3H^{+\bullet}$, and $CD_4^{+\bullet}$ have also been studied, the result of which indicates that the Jahn-Teller distortion to a C_{2v} conformation is common to all the radical cations of substituted and unsubstituted methanes. In $CH_3D^{+\bullet}$ and $CD_3H^{+\bullet}$ tunnelings among the three equivalent C_{2v} structures take place. The hyperfine coupling constant of ^{13}C has been obtained from the study of $^{13}CH_3D^{+\bullet}$ and $^{13}CH_4^{+\bullet}$.

Appendix A Molecular Symmetry Group

A brief outline of the concept of molecular symmetry group will be given following the textbook by Bunker (1979). The molecular symmetry group was first proposed by Longuet-Higgins [1963] and particularly useful for non-rigid systems such as the hydrogen fluoride dimer [Dyke *et al.* (1972)], the water dimer [Dyke (1977)], and the methane-HCl complex [Ohshima and Endo (1990)]. Matrix isolated molecules in static crystal fields have also been studied by way of the MS group [Miller and Decius (1973)].

1. Permutations and permutation groups

Permutation: $(abc \cdots yz)$

The symbol $(abc \cdots yz)$ represents a permutation that replaces a by b, b by c, c by d, ..., y by z, and z by a.

Example:

A permutation operation (123) on the three protons in a CH_3F molecule.

$$\begin{aligned}(123)\ &[X_1, Y_1, Z_1, X_2, Y_2, Z_2, X_3, Y_3, Z_3] \\ &= [\widetilde{X_1}, \widetilde{Y_1}, \widetilde{Z_1}, \widetilde{X_2}, \widetilde{Y_2}, \widetilde{Z_2}, \widetilde{X_3}, \widetilde{Y_3}, \widetilde{Z_3}] \\ &= [X_3, Y_3, Z_3, X_1, Y_1, Z_1, X_2, Y_2, Z_2]. \qquad \text{(A.1)}\end{aligned}$$

In eq. (A.1) (X_i, Y_i, Z_i) are the initial space fixed coordinates of proton i and $(\widetilde{X_i}, \widetilde{Y_i}, \widetilde{Z_i'})$ are the coordinates of proton i after the permutation has been performed.

The permutation group: S_n

A set of all possible permutation operations of n objects satisfies the group axioms. It is called the permutation group of degree n and denoted as S_n. There are $n!$ elements in S_n and the group is said to have order $n!$.

Example:

$$S_3 = \{E, (12), (23), (31), (123), (132)\}. \tag{A.2}$$

The group axioms:

1. The group S is closed with respect to an operation denoted by $\circ$.
   $\forall a, b \ni S, a \circ b = c \ni S$
2. The identity: E $\quad \exists E \ni S$, such that $a \circ E = E \circ a = a$
3. The reciprocal: a^{-1} $\quad \exists a^{-1} \ni S$, such that $a \circ a^{-1} = a^{-1} \circ a = E$
4. The operation $\circ$ is associative: $\quad (a \circ b) \circ c = a \circ (b \circ c)$

The CNP (complete nuclear permutation group) group of a molecule: G^{CNP}

The CNP group of a molecule is a group which contains all possible permutations of identical nuclei in the molecule. If the molecule has a chemical formula of $A_l B_m C_n \cdots$, the CNP group is the direct product group,

$$G^{\mathrm{CNP}} = S_l \otimes S_m \otimes S_n \otimes \cdots, \tag{A.3}$$

and the order of the group is $l! \times m! \times n! \times \cdots$.

Examples:

CH_3F $\quad G^{\mathrm{CNP}} = S_3.$ (A.4)

H_2O_2 $\quad G^{\mathrm{CNP}} = S_2 \otimes S_2.$ (A.5)

C_2H_4 $\quad G^{\mathrm{CNP}} = S_2 \otimes S_4.$ (A.6)

2. The inversion operation and permutation-inversion groups

The inversion operation: E^*

The inversion operation E^* is defined as the operation of inverting the spatial coordinates of all particles (nuclei and electrons) in a molecule through the molecular center of mass. When we use the space fixed (X, Y, Z) axis system with origin at the molecular center of mass, we can write

$$E^* [X_i, Y_i, Z_i] = [\widetilde{X}_i, \widetilde{Y}_i, \widetilde{Z}_i] = [-X_i, -Y_i, -Z_i]. \tag{A.7}$$

The inversion group: $\mathcal{E} = \{E, E^*\}$

A permutation inversion operation: P^*

Since the inversion operation E^* commutes with any permutation operation P, we can write the permutation inversion operation as P^*.

$$PE^* = E^*P = P^*. \tag{A.8}$$

The CNPI (complete nuclear permutation inversion) group: G^{CNPI}

The CNPI group of a molecule is a group which contains all possible permutations of identical nuclei in the molecule with and without inversion and is the direct product group of the complete nuclear permutation (CNP) group and the inversion group. The order of CNPI group is twice as many as the CNP group.

$$G^{\mathrm{CNPI}} = G^{\mathrm{CNP}} \otimes \mathcal{E}. \tag{A.9}$$

Examples:

C_2H_4

$$G^{\mathrm{CNPI}} = G^{\mathrm{CNP}} \otimes \mathcal{E} = S_2 \otimes S_4 \otimes \mathcal{E}. \tag{A.10}$$

H_2O

$$G^{\mathrm{CNPI}} = G^{\mathrm{CNP}} \otimes \mathcal{E} = S_2 \otimes \mathcal{E} = \{E, (12), E^*, (12)^*\}. \tag{A.11}$$

3. The molecular Hamiltonian and its true symmetry

The molecular Hamiltonian: $\mathcal{H}$

$$\mathcal{H} = \mathcal{T} + V + \mathcal{H}_{es} + \mathcal{H}_{ns}. \qquad \text{(A.12)}$$

where

$\mathcal{T}$: kinetic energy

V: electrostatic potential energy

$\mathcal{H}_{es}$: interaction energy of the electron spin magnetic moments

$\mathcal{H}_{so}$	electron spin-electron orbit	$S \cdot L$
$\mathcal{H}_{sr}$	electron spin-rotation (nuclear motion)	$S \cdot N$
$\mathcal{H}_{ss}$	electron spin-electron spin	$S \cdot S$

$\mathcal{H}_{ns}$: interaction energy of the nuclear spin magnetic moments

$\mathcal{H}_{nso}$	nuclear spin-electron orbit	$I \cdot L$
$\mathcal{H}_{nsr}$	nuclear spin-rotation	$I \cdot N$
$\mathcal{H}_{nsns}$	nuclear spin-nuclear spin	$I_i \cdot J \cdot I_j$
$\mathcal{H}_{nses}$	nuclear spin-electron spin	$S \cdot T \cdot I_j$
$\mathcal{H}_{quad}$	nuclear quadrupole	$\sum_{m=-2}^{2} Q_m^{(2)} V_{-m}^{(2)}$

The space fixed MCM (molecular center of mass) axis system: (X, Y, Z)

Separation of the kinetic energy of the center of mass

The kinetic energy operator $\mathcal{T}$ in an arbitrary space fixed (X, Y, Z) axis system is given by

$$\mathcal{T} = -\frac{\hbar^2}{2} \sum_{r=1}^{l} \frac{1}{m_r} \left(\frac{\partial^2}{\partial X_r^2} + \frac{\partial^2}{\partial Y_r^2} + \frac{\partial^2}{\partial Z_r^2} \right) \qquad \text{(A.13)}$$

where l is the total number of all the nuclei and electrons in the molecule We introduce the space fixed MCM (X, Y, Z) axis system parallel to the (X, Y, Z) system;

$$X_r = X_r + X_0, \tag{A.14}$$

$$Y_r = Y_r + Y_0, \tag{A.15}$$

and

$$Z_r = Z_r + Z_0, \tag{A.16}$$

where (X_0, Y_0, Z_0) are the coordinates of the molecular center of mass in the (X, Y, Z) axis system. To separate the translational kinetic energy we choose the set of $3l$ independent variables as

$$X_0, Y_0, Z_0, X_2, Y_2, Z_2, \ldots, X_l, Y_l, Z_l. \tag{A.17}$$

The coordinates X_1, Y_1, and Z_1 can be eliminated because of the center of mass condition,

$$m_1 X_1 = -\sum_{r=2}^{l} m_r X_r \tag{A.18}$$

with similar equations for Y_1 and Z_1. Then, we get

$$\mathcal{T} = \mathcal{T}_{CM} + \mathcal{T}_{int} \tag{A.19}$$

where

$$\mathcal{T}_{CM} = -\frac{\hbar^2}{2M}\left(\frac{\partial^2}{\partial X_0^2} + \frac{\partial^2}{\partial Y_0^2} + \frac{\partial^2}{\partial Z_0^2}\right) \tag{A.20}$$

$$\mathcal{T}_{int} = -\frac{\hbar^2}{2}\sum_{r=2}^{l}\frac{1}{m_r}\left(\frac{\partial^2}{\partial X_r^2} + \frac{\partial^2}{\partial Y_r^2} + \frac{\partial^2}{\partial Z_r^2}\right) + \frac{\hbar^2}{2M}\sum_{r=2}^{l}\sum_{s=2}^{l}\left(\frac{\partial^2}{\partial X_r \partial X_s} + \frac{\partial^2}{\partial Y_r \partial Y_s} + \frac{\partial^2}{\partial Z_r \partial Z_s}\right) \tag{A.21}$$

and M is the total mass of all the electrons and nuclei in the molecule.

$$M = \sum_{r=1}^{l} m_r \tag{A.22}$$

The full symmetry group of the molecular Hamiltonian

The exact Hamiltonian of an isolated molecule commutes with (or is invariant to) all of the following operations:

(a) any translation of the molecule along a space fixed direction,

(b) any rotation of the molecule about a space fixed axis passing through the center of mass of the molecule,

(c) any permutation of the space and spin coordinates of the electrons,

(d) any permutation of the space and spin coordinates of identical nuclei,

(e) the inversion of the coordinates of all the particles (nuclei and electrons) in the center of mass of the molecule, and

(f) time reversal.

Each set of operations (a) to (e) forms a corresponding true symmetry group;

(a) the translational group G_T,

(b) the spatial rotation group K(spatial),

(c) the electron permutation group $S_n^{(e)}$,

(d) the complete nuclear permutation group G^{CNP}, and

(e) the inversion group $\mathcal{E}$.

Each of these groups is called a true symmetry group of the molecular Hamiltonian since elements of the group commute with the exact molecular Hamiltonian. The full Hamiltonian group G_{full} is the direct product of the above five groups:

$$\begin{aligned} G_{full} &= G_T \otimes K(\text{spatial}) \otimes S_n^{(e)} \otimes G^{CNP} \otimes \mathcal{E} \\ &= G_T \otimes K(\text{spatial}) \otimes S_n^{(e)} \otimes G^{CNPI} \end{aligned} \qquad \text{(A.23)}$$

Symmetry labels (i.e., irreducible representation labels) obtained by using G_{full} or a subgroup of it are called true symmetry labels. In particular the true symmetry labels obtained by using the group G^{CNPI} or the molecular symmetry group (a subgroup of G^{CNPI}) are useful for analyzing a non-rigid system, rotation-vibration coupling, and so on. The five subgroups of G_{full} and symmetry labels of the complete wavefunctions in these groups are summarized in Table A.1.

Table A.1 The true symmetry groups of the Hamiltonian of an isolated molecule

Symmetry group	Fundamental concept	Symmetry label of the complete wavefunctions
G_T	Uniform space	Linear momentum vector $\boldsymbol{k}$
K(spatial)	Isotropic space	Total angular momentum F, m_F
$S_n^{(e)}$	Indistinguishability of electrons	The antisymmetric representation $\Gamma^{(e)}$(A)
G_{CNP}	Indistinguishability of identical nuclei	The antisymmetric representation Γ^{CNP}(A)
$\mathcal{E}$	Conservation of parity	Parity ±

$\Gamma^{(e)}$(A): The character is (+1) under even permutations and (−1) under odd permutations.
Γ^{CNP}(A): The character is (−1) for nuclear permutations that involve odd permutation of fermion nuclei and (+1) for all the other nuclear permutations.
Note that the symmetry label of the complete wavefunctions in $S_n^{(e)}$ and G_{CNP} is restricted by the Fermi-Dirac and Bose-Einstein statistics.

Basis functions and basis function symmetry

In the space fixed MCM (X, Y, Z) axis system we can separate the translational kinetic energy and obtain the internal Hamiltonian $\mathcal{H}_{int}$.

$$\mathcal{H} = \mathcal{T}_{CM} + \mathcal{H}_{int}, \tag{A.24}$$

where

$$\mathcal{H}_{int} = \mathcal{T}_{int} + V + \mathcal{H}_{es} + \mathcal{H}_{ns} \tag{A.25}$$

A suitable choice of the $(3l-3)$ coordinates in $\mathcal{H}_{int}$ makes the major part of $\mathcal{H}_{int}$ to be separable into independent five parts, i.e., the rotational, vibrational, electronic, electron spin, and nuclear spin Hamiltonians.

$$\mathcal{H}_{int} = \mathcal{H}^0_{int} + \mathcal{H}' \tag{A.26}$$

where

$$\mathcal{H}^0_{int} = \mathcal{H}_{rot} + \mathcal{H}_{vib} + \mathcal{H}_{elec} + \mathcal{H}_{ss} + \mathcal{H}_{nsns} \tag{A.27}$$

The remaining part of the Hamiltonian $\mathcal{H}'$ contains all the terms that spoil the separation of coordinates. Note that a part of the internal kinetic energy is also contained in $\mathcal{H}'$ since it

spoils the separation of rotational, vibrational, and electronic coordinates (see eqs. (A50) – (A52), (A59), (A71) – (A73)). As a result of the separation of coordinates in $\mathcal{H}^0_{\rm int}$ we can write

$$\mathcal{H}^0_{\rm int}\,\Phi^0_{\rm int} = E^0_{\rm int}\,\Phi^0_{\rm int} \tag{A.28}$$

where

$$\Phi^0_{\rm int} = \Phi_{\rm rot}\,\Phi_{\rm vib}\,\Phi_{\rm elec}\,\Phi_{\rm ss}\,\Phi_{\rm nsns} \tag{A.29}$$

$$E^0_{\rm int} = E_{\rm rot} + E_{\rm vib} + E_{\rm elec} + E_{\rm ss} + E_{\rm nsns} \tag{A.30}$$

The eigenfunctions of the separable and approximate Hamiltonian $\mathcal{H}^0_{\rm int}$ form basis functions for the diagonalization of the true $\mathcal{H}_{\rm int}$. Each component function of $\Phi^0_{\rm int}$ can be classified in the true symmetry groups of the molecular Hamiltonian to give basis function symmetry labels. The basis function symmetry is summarized in Table A.2.

Table A.2 Basis function symmetry

	$\Phi_{\rm rot}$	$\Phi_{\rm vib}$	$\Phi_{\rm elec}$	$\Phi_{\rm espin}$	$\Phi_{\rm nspin}$	$\Phi^0_{\rm int}$
$G_{\rm T}$	S	S	S	S	S	S
K(spatial)	$D^{(N)}$			$D^{(S)}$	$D^{(I)}$	$D^{(F)}$
$S_n^{(e)}$	S	S	$\Gamma^{(e)}_{\rm elec}$	$\Gamma^{(e)}_{\rm espin}$	S	$\Gamma^{(e)}$(A)
$G^{\rm CNP}$	$\Gamma^{\rm CNP}_{\rm rve}$			S	$\Gamma^{\rm CNP}_{\rm nspin}$	$\Gamma^{\rm CNP}$(A)
$\mathcal{E}$	$\pm$			+	+	$\pm$

S: totally symmetric representation.

N: rovibronic angular momentum.
S: electron spin angular momentum.
I: nuclear spin angular momentum.
F: total angular momentum.

$$F = J + I \tag{A.31}$$

$$J = N + S \tag{A.32}$$

Fermi-Dirac and Bose-Einstein statistical restrictions

$$\Gamma^{(e)}_{\rm elec} \otimes \Gamma^{(e)}_{\rm espin} \supset \Gamma^{(e)}(\mathrm{A}) \tag{A.33}$$

$$\Gamma^{\rm CNP}_{\rm rve} \otimes \Gamma^{\rm CNP}_{\rm nspin} \supset \Gamma^{\rm CNP}(\mathrm{A}) \tag{A.34}$$

4. The rovibronic coordinates

The space fixed NCM (nuclear center of mass) axis system: (ξ, η, ζ)

Separation of the electronic and nuclear kinetic energy

When we change the coordinate system in the internal kinetic energy $\mathcal{T}_{\text{int}}$ from the space fixed MCM (X, Y, Z) axis system to the space fixed NCM (ξ, η, ζ) axis system parallel to the (X, Y, Z) system, we can separate the electronic and nuclear kinetic energy.

$$\mathcal{T}_{\text{int}} = \mathcal{T}_{\text{N}} + \mathcal{T}_{\text{e}} \tag{A.35}$$

$$\mathcal{T}_{\text{N}} = -\frac{\hbar^2}{2}\sum_{i=2}^{N}\frac{1}{m_i}\left(\frac{\partial^2}{\partial\xi_i^2}+\frac{\partial^2}{\partial\eta_i^2}+\frac{\partial^2}{\partial\zeta_i^2}\right)+\frac{\hbar^2}{2M_{\text{N}}}\sum_{i,j=2}^{N}\left(\frac{\partial^2}{\partial\xi_i\partial\xi_j}+\frac{\partial^2}{\partial\eta_i\partial\eta_j}+\frac{\partial^2}{\partial\zeta_i\partial\zeta_j}\right) \tag{A.36}$$

$$\mathcal{T}_{\text{e}} = -\frac{\hbar^2}{2m_{\text{e}}}\sum_{i=N+1}^{l}\left(\frac{\partial^2}{\partial\xi_i^2}+\frac{\partial^2}{\partial\eta_i^2}+\frac{\partial^2}{\partial\zeta_i^2}\right)-\frac{\hbar^2}{2M_{\text{N}}}\sum_{i,j=N+1}^{l}\left(\frac{\partial^2}{\partial\xi_i\partial\xi_j}+\frac{\partial^2}{\partial\eta_i\partial\eta_j}+\frac{\partial^2}{\partial\zeta_i\partial\zeta_j}\right) \tag{A.37}$$

where nuclei are labeled 1,2, ..., N and electrons are labeled $N + 1, N + 2, ..., l$. The total mass of all the nuclei in the molecule is denoted M_{N};

$$M_{\text{N}} = \sum_{i=1}^{N} m_i \tag{A.38}$$

The kinetic energy is completely separable into a nuclear part $\mathcal{T}_{\text{N}}$ and an electronic part $\mathcal{T}_{\text{e}}$ in the (ξ, η, ζ) system.

The molecule fixed axis system: (x, y, z)

The molecule fixed axis system (x, y, z) has the origin at the nuclear center of mass and an orientation away from the (ξ, η, ζ) axis system that is determined by the nuclear coordinates $(\xi_2, \eta_2, \zeta_2, \cdots, \xi_N, \eta_N, \zeta_N)$. It is introduced to facilitate the separation of the rotational and vibrational coordinates. The Euler angles θ, ϕ, and χ are used to define the orientation of the (x, y, z) axis system relative to the (ξ, η, ζ) axis system:

$$\begin{pmatrix} x_i \\ y_i \\ z_i \end{pmatrix} = [\mathbf{R}] \begin{pmatrix} \xi_i \\ \eta_i \\ \zeta_i \end{pmatrix} \tag{A.39}$$

where

$$\mathbf{R} = \begin{pmatrix} \cos\theta\cos\phi\cos\chi - \sin\phi\sin\chi & \cos\theta\sin\phi\cos\chi + \cos\phi\sin\chi & -\sin\theta\cos\chi \\ -\cos\theta\cos\phi\sin\chi - \sin\phi\cos\chi & -\cos\theta\sin\phi\sin\chi + \cos\phi\cos\chi & \sin\theta\sin\chi \\ \sin\theta\cos\phi & \sin\theta\sin\phi & \cos\theta \end{pmatrix} \tag{A.40}$$

Electronic kinetic energy operator $\mathcal{T}_e$ does not change its form upon a rotation of the axis system **R**, where the Euler angles are defined purely by the nuclear coordinates.

$$\mathcal{T}_e = -\frac{\hbar^2}{2m_e}\sum_{i=N+1}^{l}\left(\frac{\partial^2}{\partial x_i^2}+\frac{\partial^2}{\partial y_i^2}+\frac{\partial^2}{\partial z_i^2}\right) - \frac{\hbar^2}{2M_N}\sum_{i,j=N+1}^{l}\left(\frac{\partial^2}{\partial x_i \partial x_j}+\frac{\partial^2}{\partial y_i \partial y_j}+\frac{\partial^2}{\partial z_i \partial z_j}\right) \tag{A.41}$$

On the other hand, the electronic coordinates are introduced back into the expression for $\mathcal{T}_N$ in the (x, y, z) axis system.

Summary of the four Cartesian axis systems

(a) The space fixed axis system: (X, Y, Z)

The (X, Y, Z) axis system is fixed in space with an arbitrary origin.

(b) The space fixed MCM (molecular center of mass) axis system: (X, Y, Z)

The (X, Y, Z) axis system is taken to be parallel to the (X, Y, Z) axis system with the origin at the molecular center of mass. The coordinates of the molecular center of mass in the (X, Y, Z) axis system are designated (X_0, Y_0, Z_0). This axis system is introduced to separate the kinetic energy of the molecular center of mass.

(c) The space fixed NCM (nuclear center of mass) axis system: (ξ, η, ζ)

The (ξ, η, ζ) axis system is taken to be parallel to both the (X, Y, Z) and (X, Y, Z) axis systems but with the origin at the nuclear center of mass. The coordinates of the nuclear center of mass in the (X, Y, Z) axis system are designated $(X_{NCM}, Y_{NCM}, Z_{NCM})$. This axis system is introduced to separate the nuclear and electronic kinetic energy.

(d) The molecule fixed axis system: (x, y, z)

The (x, y, z) axis system has the origin at the nuclear center of mass (as for the (ξ, η, ζ) axis system) but has an orientation away from the (ξ, η, ζ) system. The orientation is determined by the nuclear coordinates and the Euler angles θ, φ, and χ are used to define the orientation of the (x, y, z) axis system relative to the (ξ, η, ζ) axis system. This axis system is introduced to facilitate the separation of rotational and vibrational coordinates.

Changing to rovibronic coordinates I. Diatomic molecule

For a diatomic molecule we label the two nuclei 1 and 2 and the n electrons 3, 4, ..., $n+2$. The molecule fixed (x, y, z) axis system is fixed so that the z axis points from nucleus 1 to nucleus 2. This defines the two rotational variables θ and ϕ. We choose $\chi = 0$ to define the location of the x and y axes. As a result the coordinates are changed form $(\xi_2, \eta_2, \zeta_2,\ldots,\zeta_{n+2})$ to $(\theta, \phi, R, x_3, y_3, z_3,\ldots, z_{n+2})$, where R is the internuclear distance. In the new coordinates $\mathcal{T}_N$ becomes as follows.

$$\mathcal{T}_N = -\frac{1}{2\mu R^2}\left[\hbar^2 \frac{\partial}{\partial R}\left(R^2 \frac{\partial}{\partial R}\right) - (J_x - L_x)^2 - \frac{1}{\sin\theta}(J_y - L_y)\sin\theta(J_y - L_y)\right] \qquad \text{(A.42)}$$

where

$$\mu = \frac{m_1 m_2}{m_1 + m_2} \qquad \text{(A.43)}$$

and

$\boldsymbol{J}$: the rovibronic angular momentum operator

$\boldsymbol{L}$: the electronic angular momentum operator

the three components of $\boldsymbol{J}$ in the molecule fixed axis system (x, y, z)

$$J_x = i\hbar \csc\theta \frac{\partial}{\partial\phi} + \cot\theta L_z \qquad \text{(A.44)}$$

$$J_y = -i\hbar \frac{\partial}{\partial\theta} \qquad \text{(A.45)}$$

$$J_z = L_z \qquad \text{(A.46)}$$

commutators

$$[J_x, J_y] = -i\hbar \cot\theta J_x - i\hbar L_z\,, \quad [J_y, J_z] = [J_z, J_x] = 0 \qquad \text{(A.47)}$$

commutators for the three components of $\boldsymbol{L}$ in the (x, y, z) axis system

$$[L_\alpha, L_\beta] = i\hbar \sum_\gamma \varepsilon_{\alpha\beta\gamma} L_\gamma \qquad \alpha, \beta, \gamma = x, y, \text{ or } z \tag{A.48}$$

where

$\varepsilon_{\alpha\beta\gamma} = +1$ if $\alpha\beta\gamma$ are cyclic (i.e., xyz, yzx, or zxy).
$= -1$ if $\alpha\beta\gamma$ are anticyclic (i.e., zyx, yxz, or xzy).
$= 0$ otherwise.

Note that x and z components of $\boldsymbol{J}$ do not commute with x and y components of $\boldsymbol{L}$ for a diatomic molecule.

The rovibronic Schrödinger equation of a diatomic molecule in the new coordinate system is represented as

$$[\mathcal{T}_{\text{rot}} + \mathcal{T}_{\text{vib}} + \mathcal{T}_{\text{e}} + V(R, x_3, y_3, z_3, \ldots, z_{n+2}) - E_{\text{rve}}]\, \Phi_{\text{rve}}(R, \theta, \phi, x_3, y_3, z_3, \ldots, z_{n+2}) = 0 \tag{A.49}$$

where

$$\mathcal{T}_{\text{rot}} = \frac{1}{2\mu R^2}\left[(J_x - L_x)^2 + \frac{1}{\sin\theta}(J_y - L_y)\sin\theta(J_y - L_y)\right] \tag{A.50}$$

$$\mathcal{T}_{\text{vib}} = -\frac{\hbar^2}{2\mu R^2}\frac{\partial}{\partial R}\left(R^2\frac{\partial}{\partial R}\right) \tag{A.51}$$

and $\mathcal{T}_{\text{e}}$ is given in eq. (A.41). This Schrödinger equation does not separate into independent rotational (θ, ϕ), vibrational (R), and electronic $(x_3, y_3, z_3, \ldots, z_{n+2})$ parts because of (a) the occurrence of both R and the electronic coordinates in V, (b) the occurrence of R in $\mathcal{T}_{\text{rot}}$ (centrifugal distortion), and (c) the occurrence of L_α in $\mathcal{T}_{\text{rot}}$ (Coriolis coupling effects on the electrons). We can achieve a separation of rotation by neglecting L_α and by setting $R = R_{\text{e}}$ (the equilibrium internuclear distance) in $\mathcal{T}_{\text{rot}}$. The approximate rigid rotor rotational kinetic energy operator is

$$\mathcal{T}^0_{\text{rot}} = \frac{1}{2\mu R_{\text{e}}^2}\left[J_x^2 + \frac{1}{\sin\theta}J_y \sin\theta J_y\right] \tag{A.52}$$

The separation of the vibrational and electronic coordinates is achieved by making the Born-Oppenheimer approximation.

Changing to rovibronic coordinates II. rigid nonlinear polyatomic molecules

In this section we will change coordinates in the Schrödinger equation for a rigid nonlinear polyatomic molecule from (ξ_2, η_2, ζ_2, ..., ζ_l) to the rovibronic coordinates (θ, ϕ, χ, Q_1, ..., Q_{3N-6}, x_{N+1}, ..., z_l), where the $(3N-6)$ Q_r s are the vibrational normal coordinates. As a result of this $\mathcal{T}_N$ will be expressed in terms of (J, L, Q_1, ..., Q_{3N-6}, P_1, ..., P_{3N-6}) where $P_r = -i\hbar\,\partial/\partial Q_r$. This coordinate change is made so that the sum of $\mathcal{T}_N$ and the internuclear potential function V_N (this arises after making the Born-Oppenheimer approximation) is separable with least approximation into a part depending only on J and into $(3N-6)$ parts each involving one Q_r and associated P_r. This coordinate change leaves the form of $\mathcal{T}_e$ unchanged as shown in (A.41). The two central parts of the coordinate change to the rovibronic coordinates are the Eckart equations [Eckart (1935)] which define the Euler angles, and the l matrix which defines the normal coordinates.

For the equilibrium nuclear configuration we usually choose the principal axes of inertia as the molecule fixed (x, y, z) axes. This choice simplifies the rotational kinetic energy. The equilibrium nuclear coordinates (x_i^e, y_i^e, z_i^e) for each nucleus i are determined from the following principal axis conditions.

$$\sum_i m_i\, x_i^e\, y_i^e = \sum_i m_i\, y_i^e\, z_i^e = \sum_i m_i\, z_i^e\, x_i^e = 0 \tag{A.53}$$

To determine the Euler angles (i.e., the orientation of the (x, y, z) axes) for an arbitrarily distorted nuclear configuration we use the Eckart equation,

$$\sum_i m_i\, \boldsymbol{r}_i^e \times \boldsymbol{r}_i = 0 \tag{A.54}$$

The three components of this equation are

$$\sum_i m_i\,(x_i^e\, y_i - y_i^e\, x_i) = 0 \tag{A.55}$$

$$\sum_i m_i\,(y_i^e\, z_i - z_i^e\, y_i) = 0 \tag{A.56}$$

and

$$\sum_i m_i\,(z_i^e\, x_i - x_i^e\, z_i) = 0 \tag{A.57}$$

The reason why we use the Eckart axis system rather than the principal axis system for a distorted configuration is that the use of the Eckart axis system approximately eliminates the coupling between rotational and vibrational coordinates. In order to separate the rotational

and vibrational kinetic energy, we must eliminate the the vibrational angular momentum J_{vib} ($\sum_i m_i r_i^e \times v_i$) because there is a Coriolis coupling of it to the rovibronic angular momentum J which will spoil the separation of the variables. Though we cannot completely eliminate J_{vib}, the Eckart condition makes it small.

The $3N \times (3N-6)$ l matrix defines the relation between the normal coordinates Q_r and the Cartesian displacement coordinates $\Delta\alpha_i (= \alpha_i - \alpha_i^e)$:

$$\sqrt{m_i}\,\Delta\alpha_i = \sum_{r=1}^{3N-6} l_{\alpha i,r}\, Q_r \tag{A.58}$$

where $\alpha = x$, y, or z. The l matrix is chosen in such a manner that the internuclear potential function V_N separates into $(3N-6)$ harmonic oscillator potential functions in the lowest power of the Q_r (the harmonic oscillator approximation). The l matrix is determined by the equilibrium nuclear geometry (the $\boldsymbol{B}$ matrix), the nuclear masses (the $\boldsymbol{M}$ matrix), and the potential function (the $\boldsymbol{F}$ matrix).

Using the Eckart equations and the l matrix the nuclear kinetic energy $\mathcal{T}_N$ in the rovibronic coordinates becomes as follows [Watson (1968)]

$$\mathcal{T}_N = \frac{1}{2}\sum_{\alpha,\beta} \mu_{\alpha\beta}(J_\alpha - p_\alpha - L_\alpha)(J_\beta - p_\beta - L_\beta) + \frac{1}{2}\sum_{r=1}^{3N-6} P_r^2 + U \tag{A.59}$$

where

$$\mu = [\boldsymbol{I}']^{-1} \tag{A.60}$$

The $\boldsymbol{I}'$ matrix is given in Sec. 11-2 (eq. 10) of Wilson, Decius, and Cross (1955). The $\boldsymbol{I}'$ matrix is almost, but not quite, equal to the instantaneous inertia matrix $\boldsymbol{I}$.

$\boldsymbol{J}$: the rovibronic angular momentum

$\boldsymbol{L}$: the electronic angular momentum

$\boldsymbol{p}$: the vibrational angular momentum (not quite equal to the quantum mechanical counterpart of $\boldsymbol{J}_{\text{vib}}$)

$$p_\alpha = \sum_{r,s=1}^{3N-6} \zeta_{r,s}^{\alpha}\, Q_r\, P_s \tag{A.61}$$

where the $\zeta_{r,s}^{\alpha}$ are Coriolis coupling constants

and

$$U = -\frac{\hbar^2}{8}\sum_{\alpha}\mu_{\alpha\alpha} \tag{A.62}$$

The expression of the three components of $\boldsymbol{J}$ in terms of Euler angles are as follows.

$$J_x = -i\hbar\left(\sin\chi\frac{\partial}{\partial\theta} - \csc\theta\cos\chi\frac{\partial}{\partial\phi} + \cot\theta\cos\chi\frac{\partial}{\partial\chi}\right) \tag{A.63}$$

$$J_y = -i\hbar\left(\cos\chi\frac{\partial}{\partial\theta} + \csc\theta\sin\chi\frac{\partial}{\partial\phi} - \cot\theta\sin\chi\frac{\partial}{\partial\chi}\right) \tag{A.64}$$

and

$$J_z = -i\hbar\frac{\partial}{\partial\chi} \tag{A.65}$$

The three components obey the commutation relations

$$[J_\alpha, J_\beta] = -i\hbar\sum_{\gamma}\varepsilon_{\alpha\beta\gamma}J_\gamma \tag{A.66}$$

where $\alpha, \beta, \gamma = x, y,$ or z. Note that these commutation relations are anomalous in that they differ from the normal ones by a change in the sign [Klein (1929), Van Vleck (1951), Curl and Kinsey (1961), Freed (1966), Brown and Howard (1976a, b)]. In a space fixed coordinate system components of $\boldsymbol{J}$ are given by

$$J_\xi = -i\hbar\sum_{j=2}^{I}\left(\eta_j\frac{\partial}{\partial\zeta_j} - \zeta_j\frac{\partial}{\partial\eta_j}\right) \tag{A.67}$$

and cyclically for J_η and J_ζ. They obey the normal commutation relations,

$$[J_\sigma, J_\tau] = +i\hbar\sum_{\nu}\varepsilon_{\sigma\tau\nu}J_\nu \tag{A.68}$$

where $\sigma, \tau, \nu = \xi, \eta,$ or ζ. The components of the electronic angular momentum operator $\boldsymbol{L}$ have the normal commutation relations even in the molecule fixed axis system (see eq. (A.48)).

The $\mu_{\alpha\beta}$ elements can be expanded as Taylor series in the Q_r as

$$\mu_{\alpha\beta} = \mu^{e}_{\alpha\beta} - \sum_{r} \mu^{e}_{\alpha\alpha} a_r^{\alpha\beta} \mu^{e}_{\beta\beta} Q_r + \frac{3}{4} \sum_{r,s,\gamma} \mu^{e}_{\alpha\alpha} a_r^{\alpha\gamma} \mu^{e}_{\gamma\gamma} a_s^{\gamma\beta} \mu^{e}_{\beta\beta} Q_r Q_s + .. \qquad \text{(A.69)}$$

with

$$\mu^{e}_{\alpha\beta} = \{[I^e]^{-1}\}_{\alpha\beta} \qquad \text{(A.70)}$$

where I^e is the moment of inertia matrix for the equilibrium configuration. In the exact nuclear kinetic energy operator (A.59), if we neglect the dependence of $\mu_{\alpha\beta}$ on the Q_r,neglect p_α, L_α and U, we obtain

$$\mathcal{T}_N^0 = \frac{1}{2} \sum_{\alpha,\beta} \mu^{e}_{\alpha\beta} J_\alpha J_\beta + \frac{1}{2} \sum_{r=1}^{3N-6} P_r^2 \qquad \text{(A.71)}$$

This approximate nuclear kinetic energy operator separates into a rotational kinetic energy term and $3N-6$ vibrational kinetic energy terms. The neglected terms are such as

$$-\frac{1}{2} \mu^{e}_{\alpha\alpha} a_r^{\alpha\beta} \mu^{e}_{\beta\beta} Q_r J_\alpha J_\beta \qquad \text{(the centrifugal distortion)} \qquad \text{(A.72)}$$

and

$$-\frac{1}{2} \mu^{e}_{\alpha\beta} J_\alpha p_\beta \qquad \text{(the Coriolis coupling)} \qquad \text{(A.73)}$$

These terms spoil the separation of the rotational and vibrational coordinates in $\mathcal{T}_N$.

The transformation properties of the Euler angles and J

For a rigid nonlinear polyatomic molecule each nuclear permutations and the inversion operations has the effect of a certain kind of rotation of the molecule fixed axes (x, y, z) and this rotation is called an equivalent rotation. If we find the equivalent rotation corresponding to a permutation or permutation inversion operation, the transformation properties of the Euler angles are easily deduced. From the transformation properties of Euler angles we can derive those of J_x, J_y, and J_z by using eq. (A.64), (A.65), and (A.66). The results are listed in Table A.3.

Table A.3 The transformation properties of the Euler angles and the components of the rovibronic angular momentum J

	$R_\alpha{}^\pi$	$R_z{}^\beta$
θ	$\pi - \theta$	θ
ϕ	$\phi + \pi$	ϕ
χ	$2\pi - 2\alpha - \chi$	$\chi + \beta$
J_x	$J_x \cos 2\alpha + J_y \sin 2\alpha$	$J_x \cos \beta + J_y \sin \beta$
J_y	$J_x \sin 2\alpha - J_y \cos 2\alpha$	$-J_x \sin \beta + J_y \cos \beta$
J_z	$-J_z$	J_z

$R_\alpha{}^\pi$ is a rotation of the molecule fixed (x, y, z) axes through π radians about an axis in the xy plane making an angle α with the x axis (α is measured in the right handed sense about the z axis).
$R_z{}^\beta$ is a rotation of the molecule fixed (x, y, z) axes through β radians about the z axis (β is measured in the right handed sense about the z axis).

5. The molecular symmetry (MS) group

The definition of the MS group and its relation to the CNPI group is summarized by Bunker (1979): The CNPI group for a molecule can be used to classify the rotational, vibrational, and electronic wavefunctions. The irreducible representation for a molecule in an electronic state in which there are two or more symmetrically equivalent nuclear equilibrium structures, between which tunneling produces no observable splittings, this classification scheme is more detailed than necessary. To symmetry label the energy levels as much as is necessary, that is in order to distinguish between energy levels that are distinguishable experimentally, it is sufficient to use a particular subgroup of the CNPI group. This subgroup, called the molecular symmetry group, is obtained from the CNPI group by deleting all "unfeasible" elements. An unfeasible element is one that interconverts symmetrically equivalent equilibrium nuclear structures that are separated by an insuperable barrier in the potential energy function on the time scale of the experiment. Feasible elements maintain an equilibrium form as itself or interconvert forms between which tunneling (such as by torsion or inversion) produces observable splittings. If we are interested in considering two or more electronic states at once to study interactions or transitions between them, the definition of a feasible element must be extended.

Examples:

The CNPI group of the following four molecules, CH_3F, NF_3, NH_3, and BF_3, is

$$G^{CNPI} = S_3 \otimes \mathcal{E} = G_{12}. \tag{A.74}$$

$$G_{12} = \{E, (12), (23), (31), (123), (132), E^*, (12)^*, (23)^*, (31)^*, (123)^*, (132)^*\} \tag{A.75}$$

The MS group of each molecule is determined as follows.

(i) CH_3F. There are two symmetrically equivalent nuclear equilibrium structures. In one of the two structures numbering of the three protons is clockwise around the C - F axis and in the other that is anticlockwise.

Since no tunneling between them is observed, elements that interconvert the clockwise and anticlockwise forms are unfeasible; E^*, (12), (23), (31), (123)*, and (132)*. Thus the MS group of CH_3F is

$$C_{3v}(M) = \{E, (123), (132), (12)^*, (23)^*, (31)^*\}. \tag{A.76}$$

which is called $C_{3v}(M)$ since it is isomorphic to the molecular point group C_{3v}

(ii) NF_3. For this pyramidal molecule there are two symmetrically equivalent equilibrium structures. Since the inversion splittings are not observed in this molecule, elements that interconvert the two structures are unfeasible. Thus, the MS group of NF_3 is the same as that of CH_3F, $C_{3v}(M)$.

(iii) NH_3. Since splittings due to inversion tunneling are observed in NH_3, all the elements of its CNPI group are feasible. Thus, the MS group of NH_3 is the same as its CNPI group, G_{12}.

(iv) BF_3. Since the molecule has the planar equilibrium configuration, there are no different symmetrically equivalent nuclear equilibrium structures. Thus, the MS group of BF_3 is the same as its CNPI group and called $D_{3h}(M)$ since it is isomorphic to D_{3h}.

6. Near symmetry group

A near symmetry group is a group whose elements do not commute with the exact Hamiltonian of an isolated molecule itself but rather they commute with a certain part of it. The molecular point group and the molecular rotation group are important near symmetry groups.

The molecular rotation group

The molecular rotation group of a molecule consists of all Euler angle transformations that leave the rigid rotor Hamiltonian of the molecule invariant. Therefore, each element of the molecular rotation group has no effect on the vibronic coordinates and spin coordinates The terms which couple the rotational coordinates to the vibronic or spin coordinates (*e.g.*, centrifugal distortion, Coriolis coupling, and spin-rotation interaction) will not necessarily be invariant under the operations of the molecular rotation group and they can break this near symmetry. Only three rotation groups appear in the molecular rotation group:

(i) **A spherical top;** $\boldsymbol{K}$(mol)

The rigid rotor Hamiltonian for a spherical top is

$$\mathcal{H}_{\text{sph}} = \hbar^{-2} B \boldsymbol{J}^2. \tag{A.77}$$

The symmetry label is J and each J level has a $(2J + 1)$-fold k degeneracy and $(2J + 1)$-fold m degeneracy where k is the quantum number of the molecule fixed J_z component and m is that of the space fixed J_ζ component.

(ii) **A symmetric top;** $\boldsymbol{D_\infty}$

The rigid rotor Hamiltonian for a symmetrical top is

$$\mathcal{H}_{\text{symm}} = \hbar^{-2}[B\boldsymbol{J}^2 + (Z - B)J_z^2]. \tag{A.78}$$

where Z is A for a prolate top and C for a oblate top. The character table of the spin double group $D_\infty{}^2$ is given in Table A.4 together with the species of J_x, J_y, and J_z and those of symmetric top functions $|J, k, m\rangle$. The species of the J_α are determined by using the Table A.3 and those of $|J, k, m\rangle$ are determined by the following equations.

$$R_z\beta\,|J, k, m\rangle = e^{ik\beta}\,|J, k, m\rangle \tag{A.79}$$

and

$$R_\alpha{}^\pi\,|J, k, m\rangle = e^{i\pi J}e^{-2ik\alpha}\,|J, -k, m\rangle \tag{A.80}$$

Table A.4 The character table of $D_\infty{}^2$ and the species of J_α and $|J, k, m\rangle$ in the group.

	E	$2R_z{}^\varepsilon$	$\cdots$	$\infty R_\alpha{}^\pi$	$R^{2\pi}$	$2R_z{}^{2\pi+\varepsilon}$	$\cdots$		K
Σ^+	1	1	$\cdots$	1	1	1	$\cdots$		0 (J even)
Σ^-	1	1	$\cdots$	−1	1	1	$\cdots$	J_z	0 (J odd)
Π	2	$2\cos\varepsilon$	$\cdots$	0	2	$2\cos\varepsilon$	$\cdots$	(J_x, J_y)	1
Δ	2	$2\cos 2\varepsilon$	$\cdots$	0	2	$2\cos 2\varepsilon$	$\cdots$		2
Φ	2	$2\cos 3\varepsilon$	$\cdots$	0	2	$2\cos 3\varepsilon$	$\cdots$		3
$\vdots$	$\vdots$	$\vdots$	$\cdots$	$\vdots$	$\vdots$	$\vdots$	$\cdots$		$\vdots$
$E_{1/2}$	2	$2\cos(\varepsilon/2)$	$\cdots$	0	−2	$-2\cos(\varepsilon/2)$	$\cdots$		1/2
$E_{3/2}$	2	$2\cos(3\varepsilon/2)$	$\cdots$	0	−2	$-2\cos(3\varepsilon/2)$	$\cdots$		3/2
$E_{5/2}$	2	$2\cos(5\varepsilon/2)$	$\cdots$	0	−2	$-2\cos(5\varepsilon/2)$	$\cdots$		5/3
$\vdots$	$\vdots$	$\vdots$	$\cdots$	$\vdots$	$\vdots$	$\vdots$	$\cdots$		$\vdots$

The last column shows the symmetry species of $|J, k, m\rangle$ as function of $K = |k|$.

(iii) **An asymmetric top; D_2**

The rigid rotor Hamiltonian for an asymmetric top is

$$\mathcal{H}_{\text{asym}} = \hbar^{-2}[AJ_a{}^2 + BJ_b{}^2 + CJ_c{}^2]. \tag{A.81}$$

and the character table of the spin double group $D_2{}^2$ is given in Table A.5.

Table A.5 The character table of the group $D_2{}^2$ and the species of J_α and those of asymmetric top functions $|J_{K_aK_c}\rangle$ in the group

	E	$R_a{}^\pi$	$R_b{}^\pi$	$R_c{}^\pi$	$R^{2\pi}$		K_aK_c
	1	2	2	2	1		
A	1	1	1	1	1		ee
B_a	1	1	−1	−1	1	J_a	eo
B_b	1	−1	1	−1	1	J_b	oo
B_c	1	−1	−1	1	1	J_c	oe
$E_{1/2}$	2	0	0	0	−2		half-integral J

$K_a = |k_a|$ and $K_c = |k_c|$, where k_a and k_c are the quantum number of J_a and J_c, respectively. The molecule fixed a, b, and c axes are determined from the moment of inertia so that $I_{aa} < I_{bb} < I_{cc}$. The rotational constants satisfy the relation of $A > B > C$.

The molecular point group

The effect of an operation of the molecular point group is rotations and reflections of the vibronic variables (vibrational displacements $\{\Delta\alpha_i = \frac{1}{\sqrt{m_i}} \sum_{r=1}^{3N-6} l_{\alpha i,r} Q_r\}$ and the electronic coordinates $\{r_i\}$) in the molecule fixed axis system [see Sec. 5.5 in Wilson, Decius, and Cross (1955)]. Thus, the molecular point group is a symmetry group of an electronic and vibronic Hamiltonians. The molecular symmetry group is used for labeling the electronic and vibronic states and it can be used for studying the vibronic interactions. However, since the Euler angles and nuclear spin coordinates are unaffected by the operation of the molecular point group, interactions between the vibronic variables and the rotation or nuclear spins (e.g., the centrifugal distortion, Coriolis coupling, and spin-orbit coupling) can break this symmetry.

For a rigid nonlinear molecule the molecular point group and the molecular symmetry group is isomorphic. Before the birth of the molecular symmetry group [Longuet-Higgins (1963)] Hougen defined the "full molecular point group" for *nonlinear* rigid molecules by combining molecular point group operations and rotations [Hougen (1962, 1963)]. It is shown that the elements of the group are permutations of identical nuclei in the molecule with or without inversion. This group is, in fact, the MS group of rigid nonlinear molecules. Bunker and Papoušek extended the definition of the molecular symmetry group to *linear* molecules and introduced the "extended molecular symmetry (EMS) group" (1969).

Example:

H_2O (see Table A.6)

the molecular point group	the molecular symmetry group
C_{2v}	C_{2v}(M)
E	E
C_{2b}	(12)
σ_{ab}	E^*
σ_{bc}	(12)*

The relation between the MS group and near symmetry groups

Each operation O of the molecular symmetry group of a molecule can be written as the product of three component operations which commute each other:

$$O = O_a O_b O_c \tag{A.82}$$

where

O_a operates on vibronic variables
and is an element of the molecular point group (for a rigid molecule),

O_b operates on the Euler angles
and is an element of the molecular rotation group,

O_c operates on nuclear spin coordinates
and is an element of nuclear spin permutation group.

An identity operation of each near symmetry group is denoted as E, R^0, and p_0, respectively.

Example:

H_2O.

$$E = ER^0p_0 \tag{A.83a}$$

$$(12) = C_{2b}R_b{}^{\pi}p_{12} \tag{A.83b}$$

$$E^* = \sigma_{ab}R_c{}^{\pi}p_0 \tag{A.83c}$$

$$(12)^* = \sigma_{bc}R_a{}^{\pi}p_{12} \tag{A.83d}$$

The effect of each operation in eq. (A.83a) was illustrated in Figure A.1.

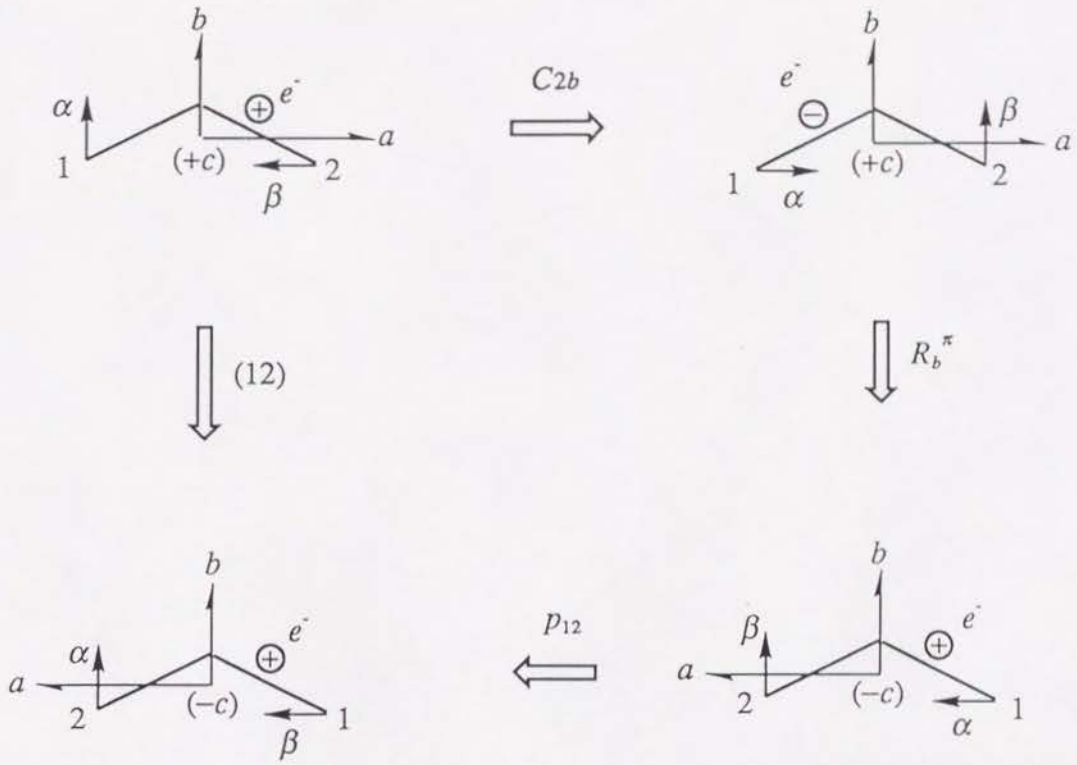

Figure A.1 The effect of successive operations of C_{2b} (rotation of vibronic coordinates by π radian around the molecule fixed b axis), $R_b{}^{\pi}$ (rotation of molecule fixed axes by π radian about b axis), and p_{12} (nuclear spin permutation). A series of these operations is equivalent to the nuclear permutation operation (12). The two hydrogen atoms are numbered 1 and 2 and their displacements from the equilibrium position are shown by the arrows. The nuclear spins of hydrogen atoms are represented α and β. An electron above the plane of the page is represented by ⊕, and that below the page is represented by ⊖.

The g and u labels in a centrosymmetric molecule

The molecular point group of a centrosymmetric molecule contains the operation i. The corresponding operation in the molecular symmetry group, O_i, can be written as the permutation inversion operation of

$$O_i = (AA')(BB')(CC') \cdots (NN')^* \tag{A.84}$$

where AA', BB', CC', , NN' are all pairs of identical nuclei located symmetrically about the nuclear center of mass (in its equilibrium nuclear configuration). Since this molecular symmetry group operation O_i does not change the Euler angles, it is related with the molecular point group operation i by

$$O_i = iR^0 p_{(AA')(BB')(CC')\cdots(NN')}. \tag{A.85}$$

Thus, the molecular point group operation i is a true symmetry operation of the rovibronic Hamiltonian and it gives the g and u labels on rovibronic states. The g and u labels are near symmetry labels that are spoiled by interactions including the nuclear spins.

7. The transformation properties of the rotational and translational coordinates, the polarizability tensor, and the electric dipole moment.

The transformation properties of the rotational and translational coordinates ($\boldsymbol{R}$ and $\boldsymbol{T}$), the polarizability tensor (α), and the electric dipole moment ($\boldsymbol{M}$) under the effect of elements of the MS group are summarized as follows:

$\boldsymbol{R}$: being the same as $\boldsymbol{J}$.

$\boldsymbol{T}$: being the same as $\boldsymbol{J}$ for permutations and having opposite sign for permutation inversions.

α: A symmetric product of the corresponding components of $\boldsymbol{T}$.

$\boldsymbol{M}$: Its components are taken in a space fixed axis system because it represents the response of a molecule to the external field. For example, its ζ component is given by

$$M_\zeta = \sum_j e_j \zeta_j \qquad \text{(A.86)}$$

Since the summation is taken over all particles in the molecule, it has the character (+) for permutations and (–) for permutation inversions. Its irreducible representation is shown by Γ^* in the following example of a character table.

Example:

Table A.6 The character table of C_{2v}(M): H_2O.

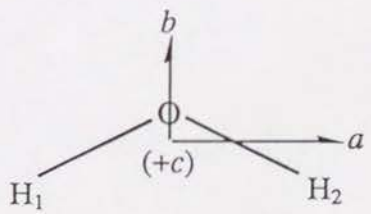

C_{2v}(M)	E	(12)	E^*	(12)*				
C_{2v}	E	C_{2b}	σ_{ab}	σ_{bc}				
Equiv. rot.	R^0	$R_b\pi$	$R_c\pi$	$R_a\pi$				
A_1	1	1	1	1		T_b	α_{aa}, α_{bb}, α_{cc}	
A_2	1	1	−1	−1	J_b		α_{ac}	Γ^*
B_1	1	−1	−1	1	J_a	T_c	α_{bc}	
B_2	1	−1	1	−1	J_c	T_a	α_{ab}	

8. An example of the application of the MS group;

Effects of the internal rotation of methyl groups on ESR spectra

The idea of the PI group proposed by Longuet-Higgins was applied to the study of the internal rotation of a methyl group by Freed (1965). He used the group consisting of cyclic permutations of methyl protons, i.e., $G_3 = \{E, (123), (132)\}$, which is isomorphic to the group C_3. Using the G_3 group he analyzed the nuclear spin and the internal rotational functions and explained the equally spaced septet ESR lines of the methyl group. We applied the method to the two equivalent methyl groups in the radical cation of dimethylether [Matsushita *et al.* (1990a)]. If the radical is completely isolated, its MS group would be G_{36}, the character table of which is given in Table A.7 [Bunker (1979)]. When the methyl groups are approximated as C_3 rotors the rotational kinetic energy (including the internal rotation of methyl groups) becomes as follows [Lin and Swalen (1959), Swalen and Costain (1959), Myers and Wilson (1960)].

$$\mathcal{T} = C\,P_x^2 + A\,P_y^2 + B\,P_z^2 + F_z\,(p_+ - 2\,\rho_z\,P_z)^2 + F_y\,(p_- - 2\,\rho_y\,P_y)^2 \qquad \text{(A.87)}$$

where

$$A = \frac{1}{2\,I_y} \qquad P_x = \frac{\partial \mathcal{T}}{\partial \omega_x}$$
$$B = \frac{1}{2\,I_z} \qquad P_y = \frac{\partial \mathcal{T}}{\partial \omega_y} \qquad \text{(A.88a)}$$
$$C = \frac{1}{2\,I_x} \qquad P_z = \frac{\partial \mathcal{T}}{\partial \omega_z}$$

$$F_y = \frac{1}{2\,r_y\,I_{CH_3}} \qquad p_+ = p_1 + p_2 \qquad p_1 = \frac{\partial \mathcal{T}}{\partial \dot{\alpha}_1}$$
$$F_z = \frac{1}{2\,r_z\,I_{CH_3}} \qquad p_- = p_1 - p_2 \qquad p_2 = \frac{\partial \mathcal{T}}{\partial \dot{\alpha}_2} \qquad \text{(A.88b)}$$

$$r_y = 1 - 2\,\lambda_y^2\,\frac{I_{CH_3}}{I_y} \qquad \rho_y = \lambda_y\,\frac{I_{CH_3}}{I_y}$$
$$r_z = 1 - 2\,\lambda_z^2\,\frac{I_{CH_3}}{I_z} \qquad \rho_z = \lambda_z\,\frac{I_{CH_3}}{I_z} \qquad \text{(A.88c)}$$

p_1 and p_2 are momenta associated with the internal rotation angles α_1 and α_2 which are defined to increase on rotating the methyl groups clockwise viewed outward; l_y and l_z are the direction cosines between the y and z principal axes and the top axes, where we put $l_y =$

$(l_y)_1 = -(l_y)_2$ and $l_z = (l_z)_1 = (l_z)_2$. The principal axes and the angles α_1 and α_2 are shown in the figure in Table A.7.

However, in our experiment using the solid matrix at very low temperature, the overall rotation of the radical is prohibited as is known from the anisotropic feature of the ESR spectrum. Then, the operations of the group G_{36} which are accompanied by the rotation of the molecule fix axes are unfeasible for the radical isolated in a solid matrix. Eliminating the unfeasible elements we obtain the group G_9, which is the direct product group of the two G_3 groups, i.e., $\{E, (123), (132)\} \otimes \{E, (456), (465)\}$. Correspondingly, the rotational kinetic energy operator contains only the internal rotation of the methyl groups.

$$\mathcal{T} = \frac{1}{2 I_{CH_3}} (p_1^2 + p_2^2) \qquad \text{(A.89)}$$

Using the G_9 group and eq. (A.89), we have analyzed the ESR spectrum of $CH_3OCH_3^{+\bullet}$ at 14 K (see Figure A.2) and investigated the interaction between the two methyl rotors [Matsushita *et al.* (1990a)]. The spectrum at 14 K is essentially a superposition of the ESR transitions between molecular eigenstates. However, the spectrum changes drastically with temperature and at higher temperatures the spectrum shows a septet with the binomial intensity ratio of 1:6:15:20:15:6:1. This spectral change is explained as due to dephasing between the rotationally degenerate levels, which is caused by the thermal contact with the lattice. The density operator formalism was used to simulate the spectra (see Figure A.2).

Table A.7 The character table of G_{36}: CH_3OCH_3 (with tunneling rotation)

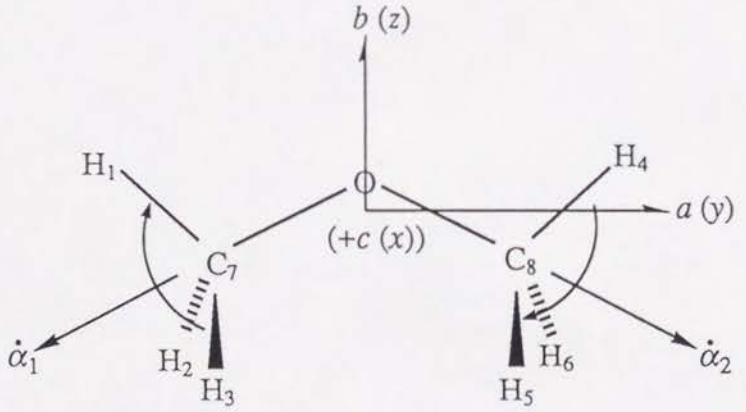

G_{36}	E	(123)(456)	(14)(26)(35)(78)*	(123)(465)	(132)	(142635)(78)*	(14)(25)(36)(78)	(142536)(78)	(23)(56)*	
	1	2	3	2	4	6	3	6	9	
Equiv.rot.	R^0	R^0	R_a^{π}	R^0	R^0	R_a^{π}	R_b^{π}	R_b^{π}	R_c^{π}	
A_1	1	1	1	1	1	1	1	1	1	$T_b,\alpha_{aa},\alpha_{bb},\alpha_{cc}$
A_2	1	1	1	1	1	1	−1	−1	−1	T_c,J_a,α_{bc}
A_3	1	1	−1	1	1	−1	1	1	−1	J_b,α_{ac},Γ^*
A_4	1	1	−1	1	1	−1	−1	−1	1	T_a,J_c,α_{ab}
E_1	2	2	2	−1	−1	−1	0	0	0	
E_2	2	2	−2	−1	−1	1	0	0	0	
E_3	2	−1	0	2	−1	0	2	−1	0	
E_4	2	−1	0	2	−1	0	−2	1	0	
G	4	−2	0	−2	1	0	0	0	0	

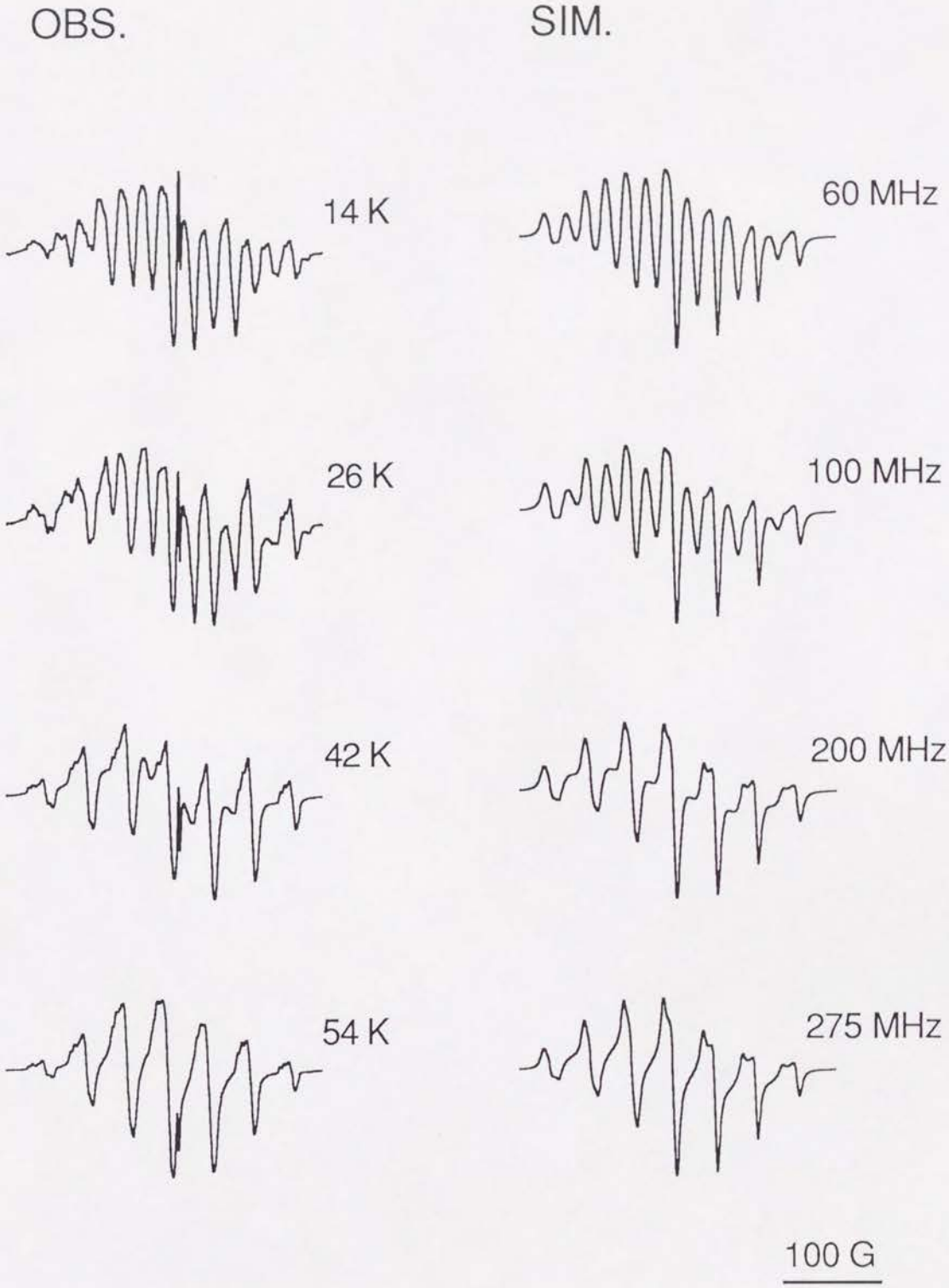

Figure A.2 Observed ESR spectra of $CH_3OCH_3^{+\bullet}$ in the temperature region of 14 - 54 K (the left column), and the corresponding simulated spectra (the right column).

Appendix B Powder-Pattern ESR Fine Structure

Spin Hamiltonian

The spin Hamiltonian used for the analysis of ESR spectra of high-spin organic molecules comprises the electron Zeeman and the fine structure terms. The anisotropy of the **g** tensor is usually negligibly small for hydrocarbons. Then, the spin Hamiltonian is described as follows.

$$\mathcal{H} = g\beta\tilde{\mathbf{S}}\cdot\mathbf{H} + \tilde{\mathbf{S}}\cdot\mathbf{D}\cdot\mathbf{S} \tag{B.1}$$

In the analysis of the Hamiltonian it is convenient to take spin projections along the static magnetic field so that the electron Zeeman term have a simple form, $g\beta S_z H$. In the $\{x, y, z\}$ axis system where z is parallel to the static magnetic field, the representation of the fine structure term becomes as follows;

$$\begin{aligned}\tilde{\mathbf{S}}\cdot\mathbf{D}\cdot\mathbf{S} = {} & D_{zz} S_z^2 \\ & + D_{zx} S_z S_x + D_{xz} S_x S_z + D_{zy} S_z S_y + D_{yz} S_y S_z \\ & + D_{xy} S_x S_y + D_{yx} S_y S_x \\ & + D_{xx} S_x^2 + D_{yy} S_y^2 \end{aligned} \tag{B.2}$$

$$\begin{aligned} = {} & D_{zz} S_z^2 \\ & + D_{xz}(S_x S_z + S_z S_x) + D_{yz}(S_y S_z + S_z S_y) + D_{xy}(S_x S_y + S_y S_x) \\ & + \frac{1}{2}(D_{xx} + D_{yy})(S_x^2 + S_y^2) + \frac{1}{2}(D_{xx} - D_{yy})(S_x^2 - S_y^2) \end{aligned}$$

$$\begin{aligned} = {} & D_{zz} S_z^2 - \frac{1}{2} D_{zz}(S^2 - S_z^2) \\ & + D_{xz}(S_x S_z + S_z S_x) + D_{yz}(S_y S_z + S_z S_y) + D_{xy}(S_x S_y + S_y S_x) \\ & + \frac{1}{2}(D_{xx} - D_{yy})(S_x^2 - S_y^2) \end{aligned}$$

where we use the relations of $D_{ij} = D_{ji}$ and tr $D = 0$. Finally we get

$$\begin{aligned}\tilde{\mathbf{S}}\cdot\mathbf{D}\cdot\mathbf{S} = {} & \frac{1}{2} D_{zz}(3S_z^2 - S^2) + \frac{1}{2}(D_{xx} - D_{yy})(S_x^2 - S_y^2) \\ & + D_{xz}(S_x S_z + S_z S_x) + D_{yz}(S_y S_z + S_z S_y) + D_{xy}(S_x S_y + S_y S_x) \end{aligned} \tag{B.3}$$

The transformation of the principal axis system $\{X, Y, Z\}$ to the laboratory axis system $\{x, y, z\}$ is represented by the orthogonal matrix **R**.

$$\begin{pmatrix} x \\ y \\ z \end{pmatrix} = [\mathbf{R}] \begin{pmatrix} X \\ Y \\ Z \end{pmatrix} \tag{B.4}$$

$$\mathbf{R} = \begin{pmatrix} \cos\theta\cos\phi\ \cos\chi - \sin\phi\ \sin\chi & \cos\theta\sin\phi\ \cos\chi + \cos\phi\ \sin\chi & -\sin\theta\cos\chi \\ -\cos\theta\cos\phi\ \sin\chi - \sin\phi\ \cos\chi & -\cos\theta\sin\phi\ \sin\chi + \cos\phi\ \cos\chi & \sin\theta\sin\chi \\ \sin\theta\cos\phi & \sin\theta\sin\phi & \cos\theta \end{pmatrix} \tag{B.5}$$

Using the transformation matrix **R**, the fine structure tensor in its principal axis system is transformed to that in the laboratory axis system by

$$\mathbf{D}_{lab.} = \mathbf{R} \cdot \mathbf{D}_P \cdot \mathbf{R}^{-1} \tag{B.6}$$

Each component of the fine structure tensor in the laboratory axis system is represented by the three principal values and the three Euler angles as follows.

$$D_{zz} = D_{XX} \sin^2\theta \cos^2\phi + D_{YY} \sin^2\theta \sin^2\phi + D_{ZZ} \cos^2\theta \tag{B.7}$$

$$\begin{aligned} D_{xx} - D_{yy} = {} & D_{XX}\left(\cos^2\theta \cos^2\phi\ \cos 2\chi - \sin^2\phi\ \cos 2\chi - \cos\theta \sin 2\phi\ \sin 2\chi\right) \\ & + D_{YY}\left(\cos^2\theta \sin^2\phi\ \cos 2\chi - \cos^2\phi\ \cos 2\chi + \cos\theta \sin 2\phi\ \sin 2\chi\right) \\ & + D_{ZZ} \sin^2\theta \cos 2\chi \end{aligned} \tag{B.8}$$

$$\begin{aligned} D_{xy} = {} & D_{XX}\left(-\frac{1}{2}\cos^2\theta \cos^2\phi\ \sin 2\chi + \frac{1}{2}\sin^2\phi\ \sin 2\chi - \frac{1}{2}\cos\theta \sin 2\phi\ \cos 2\chi\right) \\ & + D_{YY}\left(-\frac{1}{2}\cos^2\theta \sin^2\phi\ \sin 2\chi + \frac{1}{2}\cos^2\phi\ \sin 2\chi + \frac{1}{2}\cos\theta \sin 2\phi\ \cos 2\chi\right) \\ & + D_{ZZ}\left(-\frac{1}{2}\sin^2\theta \sin 2\chi\right) \end{aligned} \tag{B.9}$$

$$\begin{aligned} D_{xz} = {} & D_{XX}\left(\frac{1}{2}\sin 2\theta \cos^2\phi\ \cos\chi - \frac{1}{2}\sin\theta \sin 2\phi\ \sin\chi\right) \\ & + D_{YY}\left(\frac{1}{2}\sin 2\theta \sin^2\phi\ \cos\chi + \frac{1}{2}\sin\theta \sin 2\phi\ \sin\chi\right) \\ & + D_{ZZ}\left(-\frac{1}{2}\sin 2\theta \cos\chi\right) \end{aligned} \tag{B.10}$$

$$\begin{aligned} D_{yz} = {} & D_{XX}\left(-\frac{1}{2}\sin 2\theta \cos^2\phi\ \sin\chi - \frac{1}{2}\sin\theta \sin 2\phi\ \cos\chi\right) \\ & + D_{YY}\left(-\frac{1}{2}\sin 2\theta \sin^2\phi\ \sin\chi + \frac{1}{2}\sin\theta \sin 2\phi\ \cos\chi\right) \\ & + D_{ZZ}\left(\frac{1}{2}\sin 2\theta \sin\chi\right) \end{aligned} \tag{B.11}$$

Since the fine structure tensor is traceless, the three principal values of the tensor can be represented by the two parameters D and E as follows.

$$D_{XX} = -\frac{D}{3} + E, \quad D_{YY} = -\frac{D}{3} - E, \quad D_{ZZ} = \frac{2}{3}D \tag{B.12}$$

$$D = D_{ZZ} - \frac{1}{2}(D_{XX} + D_{YY}) = \frac{3}{2}D_{ZZ} \tag{B.13}$$

$$E = \frac{1}{2}(D_{XX} - D_{YY}) \tag{B.14}$$

Substituting eq. (B.12) to eqs. (B.7) – (B.11), we finally get the following expressions of the components of the fine structure tensor.

$$D_{zz} = D\left(\cos^2\theta - \frac{1}{3}\right) + E\,\sin^2\theta\,\cos 2\phi \tag{B.15}$$

$$D_{xx} - D_{yy} = \left[(D - E\,\cos 2\phi)\sin^2\theta + 2E\,\cos 2\phi\right]\cos 2\chi - 2E\,\cos\theta\,\sin 2\phi\,\sin 2\chi \tag{B.16}$$

$$D_{xy} = -E\,\cos\theta\,\sin 2\phi\,\cos 2\chi - \frac{1}{2}\left[(D - E\,\cos 2\phi)\sin^2\theta + 2E\,\cos 2\phi\right]\sin 2\chi \tag{B.17}$$

$$D_{xz} = -\frac{1}{2}(D - E\,\cos 2\phi)\sin 2\theta\,\cos\chi - E\,\sin\theta\,\sin 2\phi\,\sin\chi \tag{B.18}$$

$$D_{yz} = -E\,\sin\theta\,\sin 2\phi\,\cos\chi + \frac{1}{2}(D - E\,\cos 2\phi)\sin 2\theta\,\sin\chi \tag{B.19}$$

These equations, combined with the formula of fine structure term eq. (B.3), are used to construct the spin Hamiltonian when the direction of the magnetic field in the principal axis system is given by the three Euler angles. The powder-pattern spectrum can be obtained by integrated over the three Euler angles.

Transition probability

When the direction of the static magnetic field is taken to be z direction, the perturbation oscillating magnetic field is located in the xy-plane. The transition probability is the average of the orientation of the perturbation field in the xy-plane. If the anisotropy of the g tensor is neglected in the Zeeman interaction with the perturbation field, the transition probability, P, is simply determined by the expectation value of the component of S parallel to the perturbation field.

$$P_{n\to m} = \frac{1}{\pi}\int_0^{\pi} |\langle n|S(\chi)|m\rangle|^2 d\chi$$
$$= \frac{1}{\pi}\int_0^{\frac{\pi}{2}} \{|\langle n|S(\chi)|m\rangle|^2 + |\langle n|S(\chi+\pi/2)|m\rangle|^2\} d\chi \qquad \text{(B.20)}$$

where

$$S(\chi) = S_x \cos\chi + S_y \sin\chi \qquad \text{(B.21)}$$

$$S(\chi+\pi/2) = -S_x \sin\chi + S_y \cos\chi \qquad \text{(B.22)}$$

When we use the equation

$$|\langle n|S(\chi)|m\rangle|^2 + |\langle n|S(\chi+\pi/2)|m\rangle|^2 = |\langle n|S_x|m\rangle|^2 + |\langle n|S_y|m\rangle|^2, \qquad \text{(B.23)}$$

the transition probability is found to be independent of χ.

$$P_{n\to m} = \frac{1}{2}\{|\langle n|S_x|m\rangle|^2 + |\langle n|S_y|m\rangle|^2\} \qquad \text{(B.24)}$$

If we use the ladder operators, it is expressed as

$$P_{n\to m} = \frac{1}{4}\{|\langle n|S_+|m\rangle|^2 + |\langle n|S_-|m\rangle|^2\} \qquad \text{(B.25)}$$

where we use the relations

$$S_x = \frac{1}{2}(S_+ + S_-), \quad S_y = \frac{1}{2i}(S_+ - S_-) \qquad \text{(B.26)}$$

Thus, the integration over 2π is equal to the average of the modulus squared of S_+ and S_- (eq. (B.25)). The use of eq. (B.25) instead of the integration greatly reduces the computational time. However, it should be emphasized that eq.(B.25) is valid only when the anisotropy of the g tensor is negligibly small.

The expression for resonance field and the transition probabilities derived from a perturbation treatment up to the third-order are given in the literatures [Teki *et al.* (1985, 1986, 1988)]. The expression is valid for the anisotropic g tensor.

In the present work ESR spectra of the quartet monoions were calculated by diagonalizing the spin Hamiltonian of eq. (B.1). The computer program for the diagonalization and construction of the powder-pattern spectrum is listed in the following.

Computer program for the simulation of powder-pattern ESR fine structure

```
C           ESR POWDER PATTERN OF HIGH-SPIN MOLECULE
C                        QUARTET.FORT                DATE=91.08.20
C
C
C                 ESR SIMULATION PROGRAM
C           OF MULTIPLET STATE (2S+1 = 3,4,...,11)
C
C         DIRECT DIAGONOLIZATION OF SPIN HAMILTONIAN
C
C GAUSSIAN INHOMOGENEOUS LINE BROADENING
C CURVES OF ABSORPTION AND 1ST DERIVATIVE ARE OBTAINED AS RESULTS
C OPTION 1. ANGULAR DEPENDENCE OF RESONANT FIELD
C OPTION 2. MAGNETIC FIELD DEPENDENCE OF EIGEN STATES
C.....................................................................
C
      IMPLICIT   REAL*8 (A-H,O-Z)
C
      DIMENSION  SXA(720),CXA(720),SXP(360),CXP(360)
      DIMENSION  ABZ(2003),DER(2003),XAH(2003)
      DIMENSION  E(11),HFIT(55),PTR(55),BF(55)
      REAL*4     ABD(2003),DRV(2003),XMF(2003)
C*OPT2* DIMENSION .RZE1(1300),RZE2(1300),RZE3(1300),RZE4(1300)
C
      CHARACTER  TITLE*64
C
      COMPLEX*16 H(11,11),HH(11,11),F(11)
      COMPLEX*16 SZ(11,11),SX(11,11),SY(11,11),SZZ(11,11),SXXYY(11,11),
     -           SXY(11,11),SZX(11,11),SZY(11,11)
C
      PARAMETER(PI=3.14159265358)
      PARAMETER(BETA=13.99612E-4,CMIV=29.97930)
      PARAMETER(K=11)
C
C     ****  DATA FOR INTEGRATION  ****
        LIM=2
        THETA=PI/2.
        PHI=PI/2.
        IOX=260
        JOX=25
      CALL INTGPM(LIM,IOX,THETA,SXA,CXA,JOX,PHI,SXP,CXP)
        TITLE='M-PBPM CATION II'
C     ****  DATA FOR OUTPUT CHART  ****
        AH=0000.0
        PH=5.00000
        ZH=7000.00
      MH=(ZH-AH)/PH+1.001
        SPAN=20.0
        HEIGHT=15.0
        LEDER=1
C     ****  SPECTROSCOPIC DATA  ****
      FREQ=9.17500
      MS=4
      GVALUE=2.003
      DCM=0.1285
      ECM=0.0055
      WIDTH=40.0
C     ******************************
        CALL DCSMTX(SZ,SX,SY,SZZ,SXXYY,SXY,SZX,SZY,K,MS)
        DD=CMIV*DCM
        EE=CMIV*ECM
```

```
        BI=GVALUE*BETA*AH
        DB=GVALUE*BETA*PH
        DGAUS=2./(WIDTH**2)
        DCUT=12./DGAUS
C
      WRITE(6,1200)TITLE
      IF(LIM.GT.0) WRITE(6,1201)
      IF(LIM.EQ.1) WRITE(6,1202) IOX
      IF(LIM.EQ.2) WRITE(6,1203) IOX,JOX
      WRITE(6,1211) FREQ,MS
      WRITE(6,1212) GVALUE,DCM,ECM
      WRITE(6,1213) WIDTH
C
      AH1=AH
      DO 11 KH=1,MH
        ABZ(KH)=0.
        XAH(KH)=AH1
        AH1=AH1+PH
   11 CONTINUE
      DO 12 I=1,MS-1
        BF(I)=FREQ
   12 CONTINUE
      DO 13 I=MS,MS*(MS-1)/2
        BF(I)=0.01
   13 CONTINUE
C
C       START OF DOUBLE INTEGRAL
C
      DO 21 IO=1,IOX
        SA=SXA(IO)
        CA=CXA(IO)
        CCA=CA**2
        SSA=SA**2
      DO 22 JO=1,JOX
        SB=SXP(JO)
        CB=CXP(JO)
        C2B=CB**2-SB**2
        S2B=2.*SB*CB
        CALL DCFMTX(DD,EE,CA,SA,CCA,SSA,C2B,S2B,
     -              SZZ,SXXYY,SXY,SZX,SZY,K,MS,H)
C
C*OPT2*  B1=BI
C*OPT2*  DO 101 KH=1,MH
C*OPT2*    CALL DCHMTX(B1,SZ,H,K,MS,HH)
C*OPT2*    ILL=1
C*OPT2*    CALL CHOQRD(HH,K,MS,E,F,1E-6,ILL)
C*OPT2*    RZE1(KH)=E(1)
C*OPT2*    RZE2(KH)=E(2)
C*OPT2*    RZE3(KH)=E(3)
C*OPT2*    RZE4(KH)=E(4)
C*OPT2*    B1=B1+DB
C*OPT2*    WRITE(6,1019) XAH(KH),RZE1(KH),RZE2(KH),RZE3(KH),RZE4(KH)
 1019    FORMAT(2XF7.2,2X4(4E12.4))
  101    CONTINUE
      NTR=0
      DO 191 I=1,MS-1
        NTR=NTR+1
        BI=BF(I)
        J=I+1
        CALL FITMF(BI,I,J,FREQ,GVALUE,BETA,SZ,H,HH,K,MS,E,F,FITH)
        HFIT(NTR)=FITH
        CALL PRTRS(HH,K,MS,I,I+1,SX,PTR(NTR))
        BF(NTR)=BI
```

```
  191 CONTINUE
      DO 192 I=1,MS-2
      DO 192 J=I+2,MS
        NTR=NTR+1
        BI=BF(NTR)
        CALL FITMF(BI,I,J,FREQ,GVALUE,BETA,SZ,H,HH,K,MS,E,F,FITH)
        IF(FITH.LT.0.) FITH=-FITH
        HFIT(NTR)=FITH
        CALL PRTRS(HH,K,MS,I,J,SX,PTR(NTR))
        BF(NTR)=BI
  192 CONTINUE
      CALL ADDABZ(HFIT,PTR,NTR,DGAUS,DCUT,SA,AH,MH,PH,ABZ,DER)
C*OPT1*  ANGLE=90.*(FLOAT(IO)-0.5)/IOX
C*OPT1*  WRITE(10,1929) ANGLE,(HFIT(III),III=1,NTR)
 1929    FORMAT(11F9.2)
   22 CONTINUE
   21 CONTINUE
C
C       DATA OUTPUT
C
      WRITE(10,1200) TITLE
      DO 788 I=1,MH
        WRITE(10,1299) XAH(I),DER(I)
  788 CONTINUE
      DO 789 I=1,MH
        ABD(I)=ABZ(I)
        DRV(I)=DER(I)
        XMF(I)=XAH(I)
  789 CONTINUE
C
C       FORMAT STATEMENTS
C
 1200 FORMAT(//5XA64)
 1201 FORMAT(/5X'POLYCRYSTALLINE CALCULATION'/)
 1202 FORMAT(1X'THERE ARE'I4,' COMPONENTS IN THE THETA DISTRIBUTION FUNC
     -TION'/)
 1203 FORMAT(1X'THERE ARE'I4,' COMPONENTS IN THE THETA AND'I4,' IN THE P
     -HI DISTRIBUTION FUNCTIONS'/)
 1211 FORMAT(21X'MICROWAVE : 'F7.4,' GHZ'/26X'2S+1 = ',I2)
 1212 FORMAT(29X'G ='F6.3/29X'D ='F7.4,' CM'/29X'E ='F7.4,' CM'/)
 1213 FORMAT(11X'INHOMOGENEOUS LINE BROADENIG  = 'F6.1,' GAUSS'//)
 1299 FORMAT(2XF10.3,2(2XE14.7))
      STOP
      END
C******                                                          *******
C******                                                          *******
      SUBROUTINE DCSMTX(SZ,SX,SY,SZZ,SXXYY,SXY,SZX,SZY,K,MS)
C
      IMPLICIT   REAL*8 (A-H,O-Z)
      COMPLEX*16 SZ(K,MS),SX(K,MS),SY(K,MS),SZZ(K,MS),SXXYY(K,MS),
     -           SXY(K,MS),SZX(K,MS),SZY(K,MS)
C
      DO 11 J=1,MS
      DO 11 I=1,MS
        SZ(I,J)=CMPLX(0.,0.)
        SZZ(I,J)=CMPLX(0.,0.)
   11 CONTINUE
      DO 12 I=1,MS
        SZ(I,I)=CMPLX(FLOAT(MS+1-2*I)/2.,0.)
        SZZ(I,I)=CMPLX(FLOAT((MS+1-2*I)**2)/4.,0.)
   12 CONTINUE
C
      DO 21 J=1,MS
```

```
      DO 21 I=1,MS
        SX(I,J)=CMPLX(0.,0.)
        SY(I,J)=CMPLX(0.,0.)
   21 CONTINUE
      J=MS-1
      L=J
      DO 22 I=1,MS-1
        S=SQRT(FLOAT(J*(J+2)-L*(L-2)))/4.
        SX(I,I+1)=CMPLX(S,0.)
        SX(I+1,I)=CMPLX(S,0.)
        SY(I,I+1)=CMPLX(0.,-S)
        SY(I+1,I)=CMPLX(0.,S)
        L=L-2
   22 CONTINUE
C
      DO 31 J=1,MS
      DO 31 I=1,MS
        SXXYY(I,J)=CMPLX(0.,0.)
   31 CONTINUE
      J=MS-1
      L=J
      DO 32 I=1,MS-2
        S=SQRT(FLOAT((J*(J+2)-L*(L-2))*(J*(J+2)-(L-2)*(L-4))))/8.
        SXXYY(I,I+2)=CMPLX(S,0.)
        SXXYY(I+2,I)=CMPLX(S,0.)
        L=L-2
   32 CONTINUE
C
      CALL DCABBA(SX,SY,K,MS,SXY)
      CALL DCABBA(SZ,SX,K,MS,SZX)
      CALL DCABBA(SZ,SY,K,MS,SZY)
      RETURN
      END
C******                                                          *******
C******                                                          *******
      SUBROUTINE DCABBA(A,B,K,N,C)
C
      IMPLICIT   REAL*8 (A-H,O-Z)
      COMPLEX*16 A(K,N),B(K,N),C(K,N),Z
C
      DO 11 J=1,N
      DO 11 I=1,N
        Z=CMPLX(0.,0.)
        DO 12 L=1,N
          Z=Z+A(I,L)*B(L,J)+B(I,L)*A(L,J)
   12   CONTINUE
        C(I,J)=Z
   11 CONTINUE
      RETURN
      END
C******                                                          *******
C******                                                          *******
      SUBROUTINE DCFMTX(DD,EE,CA,SA,CCA,SSA,C2B,S2B,
     -                  SZZ,SXXYY,SXY,SZX,SZY,K,MS,FS)
C
      IMPLICIT   REAL*8 (A-H,O-Z)
      COMPLEX*16 SZZ(K,MS),SXXYY(K,MS),SXY(K,MS),SZX(K,MS),SZY(K,MS),
     -           FS(K,MS)
C
      DZZ=DD*(CCA-1./3.)+EE*SSA*C2B
      DXXYY=DD*SSA+EE*(CCA+1)*C2B
      DXY=-EE*CA*S2B
      DZX=(-DD+EE*C2B)*CA*SA
```

```
      DZY=-EE*SA*S2B
C
      DO 11 I=1,MS
      DO 11 J=I,MS
        FS(I,J)=1.5*DZZ*SZZ(I,J)+0.5*DXXYY*SXXYY(I,J)+DXY*SXY(I,J)+DZX*S
     -          ZX(I,J)+DZY*SZY(I,J)
   11 CONTINUE
      A=-0.5*DZZ*(MS**2-1)*0.25
      DO 12 I=1,MS
        FS(I,I)=FS(I,I)+A
   12 CONTINUE
      RETURN
      END
C******                                                              *******
C******                                                              *******
      SUBROUTINE DCHMTX(B,SZ,H,K,N,HH)
C
      IMPLICIT    REAL*8 (A-H,O-Z)
      COMPLEX*16 SZ(K,N),H(K,N),HH(K,N),Z
C
      DO 11 I=1,N
        Z=B*SZ(I,I)+H(I,I)
        HH(I,I)=Z
   11 CONTINUE
      DO 12 I=1,N-1
      DO 12 J=I+1,N
        HH(I,J)=H(I,J)
   12 CONTINUE
      RETURN
      END
C******                                                              *******
C******                                                              *******
      SUBROUTINE ADDABZ(HFIT,PTR,NTR,DGAUS,DCUT,SA,AH,MH,PH,ABZ,DER)
C
      IMPLICIT    REAL*8 (A-H,O-Z)
      DIMENSION   ABZ(MH),DER(MH),HFIT(NTR),PTR(NTR)
C
      AH1=AH
      DO 11 I=1,MH
        SUMA=0.
        SUMD=0.
        DO 12 J=1,NTR
          DH=AH1-HFIT(J)
          DHSQ=DH**2
          IF(DHSQ.GE.DCUT) GOTO 12
          FACT=PTR(J)*EXP(-DGAUS*DHSQ)
          SUMA=SUMA+FACT
          SUMD=SUMD-DH*DGAUS*FACT
   12   CONTINUE
        ABZ(I)=ABZ(I)+SA*SUMA
        DER(I)=DER(I)+SA*SUMD
        AH1=AH1+PH
   11 CONTINUE
      RETURN
      END
C******                                                              *******
C******                                                              *******
      SUBROUTINE PRTRS(HH,K,MS,I,J,SX,PROB)
C
      IMPLICIT    REAL*8 (A-H,O-Y)
      IMPLICIT    COMPLEX*16 (Z)
      COMPLEX*16 HH(K,MS),SX(K,MS)
C
```

```
      ZD=CMPLX(0.,0.)
      ZU=CMPLX(0.,0.)
      ZA1=HH(1,I)
      ZB1=HH(1,J)
      DO 11 M=2,MS
        ZA2=HH(M,I)
        ZB2=HH(M,J)
        ZSX=SX(M-1,M)
        ZD=ZD+DCONJG(ZA1)*ZSX*ZB2
        ZU=ZU+DCONJG(ZB1)*ZSX*ZA2
        ZA1=ZA2
        ZB1=ZB2
   11 CONTINUE
      PROB=REAL(ZD)**2+IMAG(ZD)**2+REAL(ZU)**2+IMAG(ZU)**2
      RETURN
      END
C******                                                              *******
C******                                                              *******
      SUBROUTINE FITMF(BI,I,J,FREQ,GVALUE,BETA,SZ,H,HH,K,MS,E,F,FITH)
C
      IMPLICIT REAL*8 (A-H,O-Z)
      COMPLEX*16 SZ(K,MS),H(K,MS),HH(K,MS),F(MS)
      DIMENSION  E(MS)
C
      BFIT=BI
      CALL DCHMTX(BFIT,SZ,H,K,MS,HH)
      ILL=1
      CALL CHOQRD(HH,K,MS,E,F,1E-6,ILL)
      DTR=FREQ-E(I)+E(J)
      DMF=DTR
   11 DTR1=DTR
      BFIT=BFIT+DMF
      CALL DCHMTX(BFIT,SZ,H,K,MS,HH)
      ILL=1
      CALL CHOQRD(HH,K,MS,E,F,1E-6,ILL)
      DTR=FREQ-E(I)+E(J)
      BDRV=DMF/(DTR1-DTR)
      DMF=DTR*BDRV
      IF(ABS(DMF).GE.0.0001) GOTO 11
      FITH=BFIT/(GVALUE*BETA)
      BI=BFIT
      RETURN
      END
C******                                                              *******
C******                                                              *******
      SUBROUTINE INTGPM(LIM,IOX,THETA,SX,CX,JOX,PHI,SXP,CXP)
C
      IMPLICIT   REAL*8 (A-H,O-Z)
      DIMENSION  SX(IOX),CX(IOX),SXP(JOX),CXP(JOX)
      PARAMETER(PI=3.14159265358)
C
      IF(LIM.LT.1) GO TO 16
      ANGLE=PI/2.
      QUANG=ANGLE/FLOAT(IOX)
      CEANG=-QUANG/2.
      DO 11 J=1,IOX
        CEANG=CEANG+QUANG
        SX(J)=SIN(CEANG)
        CX(J)=COS(CEANG)
   11 CONTINUE
      IF(LIM.LT.2) GO TO 26
      QUANG=ANGLE/FLOAT(JOX-1)
      CEANG=0.
```

```
      DO 21 J=1,JOX
        SXP(J)=SIN(CEANG)
        CXP(J)=COS(CEANG)
        CEANG=CEANG+QUANG
   21 CONTINUE
      GO TO 99
   16 IOX=1
      SX(1)=SIN(THETA)
      CX(1)=COS(THETA)
   26 JOX=1
      SXP(1)=SIN(PHI)
      CXP(1)=COS(PHI)
   99 RETURN
      END
C******                                                              *******
C******                                                              *******
C            CHOQRD              LEVEL=1        DATE=90.03.03
C#NUMPAC#CHOQRD              REVISED ON 1986-09-29
      SUBROUTINE CHOQRD(ZA,KA,N,E,ZF,EPS,IND)
      IMPLICIT REAL*8 (A-H,O-Y)
      IMPLICIT COMPLEX*16 (Z)
      DIMENSION ZA(KA,N),E(N),ZF(N)
      DATA DMACH/2.D-16/
      CDABS1(Z)=DABS(DREAL(Z))+DABS(DIMAG(Z))
   10 IF(N.LT.1.OR.N.GT.KA.OR.EPS.LE.0.D0) GO TO 300
      NM1=N-1
      NM2=N-2
      IF(N.LE.2) GO TO 90
      DO 80 K=1,NM2
      KP1=K+1
      E(K)=ZA(K,K)
      S=0.D0
      DO 20 J=KP1,N
   20 S=DREAL(ZA(K,J))**2+DIMAG(ZA(K,J))**2+S
      R=CDABS(ZA(K,KP1))
      S=DSQRT(S)
      ZT=S
      IF(R.GT.0.D0) ZT=ZA(K,KP1)*S/R
      ZA(K,KP1)=ZA(K,KP1)+ZT
      ZF(K)=-DCONJG(ZT)
      H=(R+S)*S
      IF(H.EQ.0.D0) GO TO 80
      T=0.D0
      DO 60 I=KP1,N
      ZT=0.D0
      DO 30 J=KP1,I
   30 ZT=ZA(J,I)*ZA(K,J)+ZT
      IF(I.GE.N) GO TO 50
      IP1=I+1
      DO 40 J=IP1,N
   40 ZT=DCONJG(ZA(I,J))*ZA(K,J)+ZT
   50 ZF(I)=ZT/H
   60 T=DCONJG(ZF(I))*ZA(K,I)+T
      U=T*0.5D0/H
      DO 70 J=KP1,N
      ZF(J)=ZA(K,J)*U-ZF(J)
      DO 70 I=KP1,J
   70 ZA(I,J)=DCONJG(ZF(I))*ZA(K,J)+DCONJG(ZA(K,I))*ZF(J)+ZA(I,J)
   80 ZA(K,K)=H
   90 E(N)=ZA(N,N)
      ZA(N,N)=1.D0
      IF(N.EQ.1) GO TO 290
      E(NM1)=ZA(NM1,NM1)
```

```
      ZF(NM1)=DCONJG(ZA(NM1,N))
      ZF(N)=0.D0
      ZA(NM1,NM1)=1.D0
      ZA(NM1,N)=0.D0
      ZA(N,NM1)=0.D0
      IF(IND.EQ.0.OR.N.EQ.2) GO TO 140
      DO 130 L=1,NM2
      K=NM1-L
      KP1=K+1
      H=-ZA(K,K)
      ZA(K,K)=1.D0
      IF(H.GE.0.D0) GO TO 120
      DO 110 J=KP1,N
      ZS=0.D0
      DO 100 I=KP1,N
  100 ZS=ZA(K,I)*ZA(I,J)+ZS
      ZS=ZS/H
      DO 110 I=KP1,N
  110 ZA(I,J)=DCONJG(ZA(K,I))*ZS+ZA(I,J)
  120 DO 130 I=KP1,N
      ZA(K,I)=0.D0
  130 ZA(I,K)=0.D0
  140 GN=DABS(E(1))
      DO 150 J=2,N
  150 GN=DMAX1(CDABS1(ZF(J-1))+DABS(E(J)),GN)
      IF(GN.EQ.0.D0) GO TO 290
      DEL=DMAX1(EPS,DMACH)*GN
      K=N
  160 L=K
  170 IF(CDABS1(ZF(L-1)).LT.DEL) GO TO 180
      L=L-1
      IF(L.GT.1) GO TO 170
  180 IF(L.EQ.K) GO TO 230
      W=(E(K-1)+E(K))*0.5D0
      R=E(K)-W
      X=DSIGN(DSQRT(DREAL(ZF(K-1))**2+DIMAG(ZF(K-1))**2+R*R),R)+W
      EE=E(L)-X
      E(L)=EE
      ZFF=ZF(L)
      R=DSQRT(EE*EE+DREAL(ZFF)**2+DIMAG(ZFF)**2)
      J=L
      GO TO 200
  190 R=DSQRT(E(J)*E(J)+DREAL(ZF(J))**2+DIMAG(ZF(J))**2)
      ZF(J-1)=ZS*R
      EE=E(J)*C
      ZFF=ZF(J)*C
  200 C=E(J)/R
      ZS=ZF(J)/R
      W=E(J+1)-X
      E(J)=(DCONJG(ZFF)*C+DCONJG(ZS)*W)*ZS+EE+X
      E(J+1)=C*W-DCONJG(ZFF)*ZS
      IF(IND.EQ.0) GO TO 220
      DO 210 I=1,N
      ZT=ZA(I,J+1)
      ZA(I,J+1)=ZT*C-DCONJG(ZS)*ZA(I,J)
  210 ZA(I,J)=ZA(I,J)*C+ZT*ZS
  220 J=J+1
      IF(J.LT.K) GO TO 190
      ZF(K-1)=E(K)*ZS
      E(K)=E(K)*C+X
      GO TO 160
  230 K=K-1
      IF(K.GT.1) GO TO 160
```

```
      J=N
  240 L=1
      II=1
      JJ=1
      DO 260 I=2,J
      IF(E(I).GT.E(L)) GO TO 250
      L=I
      GO TO 260
  250 JJ=L
      II=I
  260 CONTINUE
      IF(II.EQ.JJ) GO TO 280
      W=E(JJ)
      E(JJ)=E(II)
      E(II)=W
      IF(IND.EQ.0) GO TO 280
      DO 270 I=1,N
      ZT=ZA(I,JJ)
      ZA(I,JJ)=ZA(I,II)
  270 ZA(I,II)=ZT
  280 J=II-1
      IF(J.GE.2) GO TO 240
  290 IND=0
      RETURN
  300 IND=30000
      RETURN
      END
```

References

H. Ajie, M. M. Alvarez, S. J. Anz, R. D. Beck, F. Diederich, K. Fostiropoulos, D. R. Huffman, W. Krätschmer, Y. Rubin, K. E. Schriver, D. Sensharma, and R. L. Whetten, *J. Phys. Chem.* **94**, 8630 – 8633 (1990).

M. I. Al-Joboury and D. W. Turner, *J. Chem. Soc.* B, 4434 - 4441 (1964).

M. I. Al-Joboury and D. W. Turner, *J. Chem. Soc.* B, 373 - 376 (1967).

S. A. Alexander and D. J. Klein, *J. Am. Chem. Soc.* **110**, 3401 – 3405 (1988).

J. Arents and L. C. Allen, *J. Chem. Phys.* **53**, 73 - 78 (1970).

A. D. Baker, C. Baker, C. R. Brundle, and D. W. Turner, *Int. J. Mass Spectrometry and Ion Physics*, **1**, 285 - 301 (1968).

E. de Boer and S. I. Weissman, *J. Am. Chem. Soc.* **80**, 4549 – 4557 (1958).

R. W. Brandon, G. L. Closs, C. E. Davoust, C. A. Hutchison Jr., B. E. Kohler, and R. Silbey, *J. Chem. Phys.* **43**, 2006 – 2016 (1965).

B. Brehm and E. von Puttkamer, *Z. Naturforsch.* **22A**, 8 - 10 (1967)

R. Breslow and E. Wasserman, *J. Am. Chem. Soc.* **86**, 5349 – 5350 (1964).

J. Brickmann and G. Kothe, *J. Chem. Phys.* **59**, 2807 – 2814 (1973).

J. M. Brown and B. J. Howard, *Mol. Phys.* **31**, 1517 – 1525 (1976a).

J. M. Brown and B. J. Howard, *Mol. Phys.* **32**, 1197 (1976b).

C. R. Brundle, M. B. Robin, and H. Basch, *J. Chem. Phys.* **53**, 2196 - 2213 (1970).

P. R. Bunker and D. Papoušek, *J. Mol. Spectrosc.* **32**, 419 – 429 (1969).

P. R. Bunker, *"Molecular Symmetry and Spectroscopy"* Academic Press, San Diego (1979).

A. Cabana, G. B. Savitsky, and D. F. Hornig, *J. Chem. Phys.* **39**, 2942 - 2950 (1963).

A. Carrington, F. Dravnieks, and M. C. R. Symons, *J. Chem. Soc.* 947 – 952 (1959).

S. Clough and F. Poldy, *J. Chem. Phys.* **51**, 2076 - 2084 (1969).

C. A. Coulson and H. L. Strauss, *Proc. Roy. Soc.* A, **269**, 443 - 455 (1962).

R. F. Curl, Jr. and J. L. Kinsey, *J. Chem. Phys.* **35**, 1758 – 1765 (1961).

R. B. Davidson and I. Miyagawa, *J. Chem. Phys.* **52**, 1727 - 1732 (1970).

R. N. Dixon, *Mol. Phys.* **20**, 113 - 126 (1971).

T. R. Dyke, B. J. Howard, and W. Klemperer, *J. Chem. Phys.* **56**, 2442 – 2454 (1972).

T. R. Dyke, *J. Chem. Phys.* **66**, 492 – 497 (1977).

C. Eckart, *Phys. Rev.* **47**, 552 – 558 (1935).

F. H. Frayer and G. E. Ewing, *J. Chem. Phys.* **48**, 781 - 792 (1968).

K. Furukawa, T. Matsumura, Y. Teki, T. Kinoshita, T. Takui, and K. Itoh, *Prepr. XXX. ESR Symp. (Osaka)* 50 – 52 (1991).

J. H. Freed, *J. Chem. Phys.* **43**, 1710 – 1720 (1965).

K. F. Freed, *J. Chem. Phys.* **45**, 4214 –/ 4241 (1966).

R. F. Frey and E. R. Davidson, *J. Chem. Phys.* **88**, 1775 - 1785 (1988).

I. Fujita, Y. Teki, T. Takui, T. Kinoshita, K. Itoh, F. Miko, Y. Sawaki, H. Iwamura, A. Izuoka, and T. Sugawara, *J. Am. Chem. Soc.* **112**, 4074 – 4075 (1990).

A. Grimison and G. A. Simpson, *J. Phys. Chem.* **72**, 1776 – 1779 (1968).

W. H. Hamill, in *"Radical Ions"*, ed. by E. T. Kaiser and L. Kevan, pp.321 – 416, Interscience Publishers, New York (1968).

J. Higuchi, *J. Chem. Phys.* **38**, 1237 – 1245 (1963a).

J. Higuchi, *J. Chem. Phys.* **39**, 1847 – 1852 (1963b).

J. Higuchi, *Bull. Chem. Soc. Japan*, **43**, 3773 – 3779 (1970).

J. T. Hougen, *J. Chem. Phys.* **37**, 1433 – 1441 (1962).

J. T. Hougen, *J. Chem. Phys.* **39**, 358 – 365 (1963).

J. T. Hougen, in *International Review of Science, Physical Chemistry, Ser. 2, Vol. 3, Spectroscopy,* edited by D. A. Ramsay (Butterworths, London, 1976), pp. 75 - 125.

J. Hubbard, *Proc. Roy. Soc.* A, **276**, 238 – 257 (1963).

K. Itoh, *Chem. Phys. Lett.* **1**, 235 – 238 (1967).

K. Itoh, H. Konishi, and N. Mataga, *J. Chem. Phys.* **48**, 4789 – 4790 (1968).

K. Itoh, *Pure Appl. Chem.* **50**, 1251 – 1259 (1978).

H. A. Jahn and E. Teller, *Proc. Roy. Soc.* A, **161**, 220 - 235 (1937).

L. H. Jones, S. A. Ekberg, and B. I. Swanson, *J. Chem. Phys.* **85**, 3203 - 3210 (1986).

H. F. King and D. F. Hornig, *J. Chem. Phys.* **44**, 4520 - 4531 (1966).

D. J. Klein, *J. Chem. Phys.* **77**, 3098 – 3100 (1982).

D. J. Klein, C. J. Nelin, S. Alexander, and F. A. Matsen, *J. Chem. Phys.* **77**, 3101 – 3108 (1982).

O. Klein, *Z. Physik.* **58**, 730 – 734 (1929).

L. B. Knight, Jr. and J. Steadman, *J. Chem. Phys.* **78**, 5940 - 5945 (1983).

L. B. Knight, Jr., J. Steadman, D. Feller, and E. R. Davidson, *J. Am. Chem. Soc.* **106**, 3700 - 3701 (1984).

L. B. Knight, *Acc. Chem. Res.* **19**, 313 - 321 (1986).

J. Koutecký, *J. Chem. Phys.* **44**, 3702 – 3706 (1966).

W. Krätschmer, K. Fostiropoulos, and D. R. Huffman, *Chem. Phys. Lett.* **170**, 167 – 170 (1990a).

W. Krätschmer, L. D. Lamb, K. Fostiropoulos, and D. R. Huffman, *Nature* **347**, 354 – 357 (1990b).

H. W. Kroto, J. R. Heath, S. C. O'Brien, R. F. Curl, and R. E. Smalley, *Nature* **318**, 162 – 163 (1985).

E. Lieb and D. Mattis, *J. Math. Phys.* **3**, 749 – 751 (1962).

C. C. Lin and J. D. Swalen, *Rev. Mod. Phys.* **31**, 841 – 892 (1959).

H. C. Longuet-Higgins, *J. Chem. Phys.* **18**, 265 – 274 (1950).

H. C. Longuet-Higgins, *Mol. Phys.* **6**, 445 – 460 (1963).

F. Marinelli and M. Roche, *Chem. Phys.* **146**, 219 - 223 (1990).

M. Matsushita, T. Momose, and T. Shida, *J. Chem. Phys.* **92**, 4749 – 4758 (1990a).

M. Matsushita, T. Momose, T. Shida, Y. Teki, T. Takui, and K. Itoh, *J. Am. Chem. Soc.* **112**, 4700 – 4702 (1990b).

H. M. McConnell, A. D. McLean, and C. A. Reilly, *J. Chem. Phys.* **23**, 1152 - 1159 (1955).

H. M. McConnell, *J. Chem. Soc.* **29**, 1422 (1958).

A. D. McLachlan, *Mol. Phys.* **2**, 271 – 284 (1959).

A. D. McLachlan, *Mol. Phys.* **4**, 49 – 56 (1961).

W. Meyer, *J. Chem. Phys.* **58**, 1017 - 1035 (1973).

R. E. Miller and J. C. Decius, *J. Chem. Phys.* **59**, 4871 – 4883 (1973).

S. -I. Murahashi, Y. Yoshimura, Y. Yamamoto, and I. Moritani, *Tetrahedron*, **4**, 1485 – 1496 (1972).

R. J. Myers and E. B. Wilson, Jr. *J. Chem. Phys.* **33**, 186 – 191 (1960).

K. Nasu, *Phys. Rev.* **B 33**, 330 – 338 (1986).

R. Neiman and D. Kivelson, *J. Chem. Phys.* **35**, 156 – 161 (1961).

K. Nishiyama and T. Yamamoto, *J. Chem. Phys.* **58**, 1001 - 1016 (1973).

Y. Ohshima and Y. Endo, *J. Chem. Phys.* **93**, 6256 – 6265 (1990).

M. Okamoto, Y. Teki, T. Takui, T. Kinoshita, and K. Itoh, *Chem. Phys. Lett.* **173**, 265 – 270 (1990).

A. A. Ovchinnikov, *Theor. Chim. Acta* **47**, 297 – 304 (1978).

M. N. Paddon-Row, D. J. Fox, J. A. Pople, K. N. Houk, and D. W. Pratt, *J. Am. Chem. Soc.* **107**, 7696 - 7700 (1985).

B. P. Pullen, T. A. Carlson, W. E. Moddeman, G. K. Schweitzer, W. E. Bull, and F. A. Grimm, *J. Chem. Phys.* **53**, 768 - 782 (1970).

J. W. Rabalais, T. Bergmark, L. O. Werme, L. Karlsson, and K. Siegbahn, *Physica Scripta*, **3**, 13 - 18 (1971).

A. Rajca, *J. Am. Chem. Soc.* **112**, 5889 – 5890 (1990a).

A. Rajca, *J. Am. Chem. Soc.* **112**, 5890 – 5892 (1990b).

A. Rajca, *J. Org. Chem.* **56**, 2557 – 2563 (1991).

M. S. Reeves and E. R. Davidson, *J. Chem. Phys.* **95**, 6551 - 6561 (1991).

K. Reibisch, G. Kothe, and J. Brickmann, *Chem. Phys. Lett.* **17**, 86 – 89 (1972).

M. E. Rose, *"Elementary Theory of Angular Momentum"* John Wiley & Sons, New York (1957).

T. Shida and W. H. Hamill, *J. Chem. Phys.* **44**, 2369 – 2374 (1966a).

T. Shida and W. H. Hamill, *J. Chem. Phys.* **44**, 2375 – 2377 (1966b).

T. Shida and W. H. Hamill, *J. Chem. Phys.* **44**, 4372 – 4377 (1966c).

T. Shida and S. Iwata, *J. Am. Chem. Soc.* **95**, 3473 – 3483 (1973).

T. Shida and T. Kato, *Chem. Phys. Lett.* **68**, 106 – 110 (1979).

T. Shida, Y. Egawa, H. Kubodera, and T. Kato, *J. Chem. Phys.* **73**, 5963 – 5970 (1980).

T. Shida, E. Haselbach, and T. Bally, *Acc. Chem. Res.* **17**, 180 – 186 (1984).

T. Shida, *"Electronic Absorption Spectra of Radical Ions"*; Physical Sciences Data 34; Elsevier, Amsterdam (1988).

T. Shida, *Annu. Rev. Phys. Chem.* **42**, 55 – 81 (1991).

T. Shida, T. Kato, T. Momose, and M. Matsushita, *J. Chem. Phys.* **95**, 4725 – 4726 (1991).

T. Sugawara, S. Bandow, K. Kimura, H. Iwamura, and K. Itoh, *J. Am. Chem. Soc.* **106**, 6449 – 6450 (1984).

T. Sugawara, S. Bandow, K. Kimura, H. Iwamura, and K. Itoh, *J. Am. Chem. Soc.* **108**, 368 – 371 (1986).

J. D. Swalen and C. C. Costain, *J. Chem. Phys.* **31**, 1562 – 1574 (1959).

K. Takeshita, *J. Chem. Phys.* **86**, 329 - 338 (1987).

T. Takui and K. Itoh, *Chem. Phys. Lett.* **19**, 120 – 124 (1973).

T. Takui, S. Kita, S. Ichikawa, Y. Teki, T. Kinoshita, and K. Itoh, *Mol. Cryst. Liq. Cryst.* **176**, 67 – 76 (1989).

Y. Teki, T. Takui, K. Itoh, H. Iwamura, and K. Kobayashi, *J. Am. Chem. Soc.* **105**, 3722 – 3723 (1983).

Y. Teki, T. Takui, H. Yagi, K. Itoh, and H. Iwamura, *J. Chem. Phys.* **83**, 539 – 547 (1985).

Y. Teki, T. Takui, K. Itoh, H. Iwamura, and K. Kobayashi, *J. Am. Chem. Soc.* **108**, 2147 – 2156 (1986).

Y. Teki, T. Takui, T. Kinoshita, S. Ichikawa, H. Yagi, and K. Itoh, *Chem. Phys. Lett.* **141**, 201 – 205 (1987a).

Y. Teki, T. Takui, M. Kitano, and K. Itoh, *Chem. Phys. Lett.* **142**, 181 – 186 (1987b).

Y. Teki, T. Takui, and K. Itoh, *J. Chem. Phys.* **88**, 6134 – 6145 (1988).

Z. Vager, E. P. Kanter, G. Both, P. J. Cooney, A. Faibis, W. Koenig, B. J. Zabransky, and D. Zajfman, *Phys. Rev. Lett.* **57**, 2793 - 2795 (1986).

J. H. Van Vleck, *Rev. Mod. Phys.* **23**, 213 – 227 (1951).

E. Wasserman, R. W. Murray, W. A. Yager, A. M. Trozzolo, and G. Smolinsky, *J. Am. Chem. Soc.* **89**, 5076 – 5078 (1967).

E. Wasserman, K. Schueller, and W. A. Yager, *Chem. Phys. Lett.* **2**, 259 – 260 (1968).

S. I. Weissman, E. de Boer, and J. J. Conradi, *J. Chem. Phys.* **26**, 963 – 964 (1957).

J. K. G. Watson, *Mol. Phys.* **15**, 479 – 490 (1968).

E. B. Wilson, Jr., J. C. Decius, and P. C. Cross, *"Molecular Vibrations"* McGraw-Hill, New York (1955).

K. Yamaguchi, Y. Toyoda, and T. Fueno, *Synthetic Metals* **19**, 81 – 86 (1987).

Acknowledgement

The author is deeply indebted and grateful to Professor T. Shida for his helpful suggestions and continuous encouragements. The author is heartily grateful to Professor K. Itoh, Dr. T. Takui, Dr. Y. Teki, and Dr. T. Kinoshita for the joint work on the charged high-spin molecules. The author is equally indebted to Professor L. B. Knight, Jr. for the joint work on methane cation. Thanks are also due to Dr. K. Akasaka, Dr. S. Rokushika, Dr. T. Kato, and Dr. T. Momose. We wish to thank Professor T. Kawamura for allowing us to use the ESR spectrometer and the liquid helium transfer cryostat of his laboratory. The author was financially supported by Fellowship of the Japan Society for the Promotion of Science for Japanese Junior Scientists (Chemistry, 0854, (1991)). Finally, I would like to express my sincere thanks to my parents.

Michio Matsushita

Kyoto
December, 1991